Ring Resonators for Integrated Optics Applications

by

Michael Gad

A thesis
presented to the University of Waterloo
in fulfillment of the
thesis requirement for the degree of
Doctor of Philosophy
in
Physics

Waterloo, Ontario, Canada, 2011

AUTHOR'S DECLARATION

I hereby declare that I am the sole author of this thesis. This is a true copy of the thesis, including any required final revisions, as accepted by my examiners.

I understand that my thesis may be made electronically available to the public.

Abstract

Integrated ring resonators have attracted a considerable interest in optical communications because of their small size and wide range of applicability. Here we consider several aspects of these devices, beginning with a tunable hybrid ring resonators consisting of a silicon over insulator (SOI) ring covered with a polymer layer in a variable electric field. Varying the field changes the polymer refractive index and consequently the resonance condition of the cavity. This device offers a large degree of optical confinement together with a high modulation speed. Subsequently, we design and present fabrication results for a Wavelength Division Multiplexing (WDM) multiplexer/demultiplexer formed from a series of ring resonators with two channels separated by $50\,GHz$ each that is predicted to exhibit a free spectral range (FSR) of $100\ GHz$, signal dispersion less than $30\ ps/nm$ and a signal cross-talk less than $-23\,dB$. Finally, we analyze the application of the coupled ring waveguide circuit to rotation sensors based on the Sagnac phase shift. Here, however our analysis indicates that a single ring, of the same area exhibits a higher degree of sensitivity to rotational motion than a multiple ring circuit.

Acknowledgements

It was a great opportunity for me to work under the supervision of Prof. David Yevick, who is always available, knowledgeable and supportive. He is always open to any questions and is able of giving good guidance. With an expert eye, Prof. Yevick could see what was usually hidden to me, which was essential to get to creative ideas.

I would like also to acknowledge the important role of Prof. Paul Jessop from McMaster University especially in the device measurement part that took place at his lab facilities.

The fabrication part was done in collaboration with CMC, IMEC and UBC.

This work was supported by the Canadian Institute for Photonics Innovations (CIPI).

Dedication

I would like to dedicate this effort to the soul of my father, the members of my supportive family, my mother, Merit, Joseph, Daniel, Mina and Mona and also my friends in Canada who helped me a lot through this trip, Albert Wasif, Ayad Fekry, George Bassem, George Beskales, George Shaker, George Soliman, Michael Naeim, Michel El-Naggar, Hany Lewis, Hany Samuel, John Saad, Mina Farid, Mina Saleeb and Salam Gabran.

Table of Contents

AUTHOR'S DECLARATION ii
Abstract iii
Acknowledgements iv
Dedication v
Table of Contents vi
List of Figures viii
List of Tables xiii
Chapter 1 Introduction 1
1.1 Electromagnetic Background 1
1.1.1 Light propagation in a two dimensional straight waveguide 2
1.1.2 Effective index method (EIM) 5
1.1.3 Light propagation in ring resonators 11
1.1.4 Beam propagation method (BPM) 13
1.2 Field coupling and bending loss calculations 15
1.2.1 Power coupling 15
1.2.2 Propagation loss factor 19
1.3 The basic ring resonator circuit 22
1.4 Complex RR circuit analysis 25
1.4.1 Transfer matrix method 25
1.4.2 Coupling of modes in time (CMT) 27
1.5 Conclusion 29
Chapter 2 Tunable hybrid ring resonators 30
2.1 Hybrid structure design 30
2.1.1 Operation and dimensions 30
2.1.2 Polymer thickness 32
2.2 Hybrid structure application 35
2.2.1 Power transmission tuning 35
2.2.2 Ring-bus coupling variation 40

2.3 Conclusion 47
Chapter 3 Compound ring resonators 48
3.1 Transfer matrix approach 48
3.2 WDM compound ring resonator structure interleaver circuit 52
3.3 Comparison of interleavers 62
3.4 CMT analysis 63
3.4.1 CMS circuit parameters 64
3.4.2 CMT circuit parameters 65
3.4.3 Numerical results 67
3.5 Design, fabrication and characterization 71
3.6 Post fabrication study 79
3.7 Conclusion 82
Chapter 4 High sensitivity ring resonator Gyroscopes 83
4.1 Overview 83
4.2 Circuit analysis 83
4.2.1 Sagnac effect 83
4.2.2 Crow gyroscope 86
4.2.3 Loop of ring gyroscope 87
4.3 Summary of previous CROW and FOG results 88
4.4 Numerical results: 92
4.5 Conclusion 100
Chapter 5 Conclusion and future work 101
References 103

List of Figures

FIGURE 1.1: A 2D WAVEGUIDE WITH CORE WIDTH w, CORE RI n_1, CLADDING RI n_2 AND SUBSTRATE RI n_3 2

FIGURE 1.2: THREE DIMENSIONAL WAVEGUIDE 6

FIGURE 1.3: (A) THE 2D WAVEGUIDES REPRESENTING THE (A) FIRST AND (B) SECOND STEP OF THE EIM 7

FIGURE 1.4: WG1 STRUCTURE. DIFFERENT MATERIAL REGIONS ARE COLORED DIFFERENTLY ... 8

FIGURE 1.5: WG2 STRUCTURE. 9

FIGURE 1.6: B-V DIAGRAM FOR THE REDUCED WG1 AS IN THE FIRST STEP OF THE EIM. SOLID (DOTTED) LINE CURVES REPRESENT TE (TM) MODES. 10

FIGURE 1.7: B-V DIAGRAM FOR THE REDUCED WG1 AS IN THE SECOND STEP OF THE EIM. SOLID (DOTTED) LINE CURVES REPRESENT TE (TM) MODES. 10

FIGURE 1.8: A RING RESONATOR WAVEGUIDE STRUCTURE 11

FIGURE 1.9: THE TE-LIKE MODE FOR WG1 WITH THE CHARACTERISTICS IN TABLE 1.1. 14

FIGURE 1.10: THE TE-LIKE MODE FOR WG2 WITH THE CHARACTERISTICS IN TABLE 1.2. 15

FIGURE 1.11: TWO WAVEGUIDES WGI AND WGII, IN CLOSE PROXIMITY. 16

FIGURE 1.12: COUPLING BETWEEN TWO STRAIGHT WG2 WAVEGUIDES. THE POWER PROFILE IS GIVEN BY THE LEFT PLOT WHILE THE POWER LEVEL VERSUS PROPAGATION DIRECTION IS SHOWN AS THE BLUE AND GREEN LINES. 18

FIGURE 1.13: POWER COUPLING BETWEEN A STRAIGHT AND A CURVED WAVEGUIDE FOR (A) TE-LIKE AND (B) TM-LIKE MODES. 19

FIGURE 1.14: NEGLIGIBLE BENDING LOSSES FOR BENDS WITH $R = 5\,\mu m$ FOR (A) TE-LIKE FIELDS IN WG1, (B) TM-LIKE FIELDS IN WG1, (C) TE-LIKE FIELDS IN WG2 AND (D) TM-LIKE FIELDS IN WG2 21

FIGURE 1.15: SINGLE RR CIRCUIT 22

FIGURE 1.16: A RING RESONATOR COUPLED TO TWO BUSES. 24

FIGURE 1.17: SERIES COUPLED RRS 26

FIGURE 1.18: PARALLEL COUPLED RRS 26

FIGURE 1.19: A LOOP OF RINGS COUPLED TO TWO BUSES. 27

FIGURE 1.20: A SINGLE RR COUPLED TO TWO BUSES. 28
FIGURE 2.1: A SIMPLE SINGLE RING RESONATOR CIRCUIT. 31
FIGURE 2.2: A VERTICAL CROSS SECTION OF THE WAVEGUIDE STRUCTURE. THE COLOR MARK TO THE RIGHT DEFINES THE LAYER MATERIAL. 31
FIGURE 2.3: THE ABSORPTION LOSS INDUCED BY THE GOLD LAYER AS A FUNCTION OF POLYMER THICKNESS. THE INSET SHOWS THE LOSSES FOR $t_2 > 0.8\,\mu m$ 33
FIGURE 2.4: MODE REFRACTIVE INDEX (n_e) AS A FUNCTION OF THE FREE SPACE WAVELENGTH (λ_o) FOR DIFFERENT POLYMER RI (n_2) VALUES. (A) TE MODE WITH $t_2 = 0.8\,\mu m$ (B) TM MODE WITH $t_2 = 1\,\mu m$ 34
FIGURE 2.5: (A) VARIATION OF n_2 AND n_e WITH V (B) THE DEPENDENCE OF THE $R = R_{oo}$ REQUIRED ON V FOR FULL ON-OFF SWITCHING. 37
FIGURE 2.6. THE VARIATION OF THE FIELD TRANSFER COEFFICIENT r AND THE FIELD LOSS COEFFICIENT χ WITH MEAN RING RADIUS $R = R_{oo}$ AND THE RING-BUS GAP g_o 38
FIGURE 2.7: THE DEVICE NORMALIZED POWER TRANSMISSION (A) FIRST DESIGN POINT, (B) SECOND DESIGN POINT 38
FIGURE 2.8: RACETRACK-BUS CONFIGURATION. THE SILICA LAYER SURROUNDING THE SILICON CORE IS NOT SHOWN. 41
FIGURE 2.9: VARIATION OF THE POWER TRANSMISSION FACTOR (T) ON RESONANCE WITH THE FIELD COUPLING RATIO (k) FOR DIFFERENT ROUND-TRIP LOSSES 42
FIGURE 2.10. $W(\Delta n_e)$ (SOLID LINE) AND $Z(m)$ (DASHED LINE) FOR $L = n\pi/\kappa$, (A) $n = 1$, (B) $n = 2$, (C) $n = 3$, (D) $n = 4$, (E) $n = 5$, (F) $n = 6$, (G) $n = 7$, (H) $n = 8$ 45
FIGURE 2.11: $W(\Delta n_e)$ (SOLID LINE) AND $Z(m)$ (DASHED LINE) FOR (A) $L = 40.05\mu m$, (B) $L = 80\mu m$ 46
FIGURE 3.1: THE COMPOUND RING RESONATOR CIRCUIT WITH (A) $N = 4$, (B) $N = 6$ RING RESONATORS. 49
FIGURE 3.2: THE CIRCUIT RESPONSE WITH $k_o = k_{oo} = 0.935$ AND k INCREASING FROM 0.5 TO 0.6 IN STEPS OF 0.025. THE ARROWS INDICATE INCREASING PARAMETER VALUES. THE

ROUND TRIP POWER LOSS IS 10%. (A) THE POWER SPECTRA. (B) THE PHASE VARIATION. (C) THE NORMALIZED GROUP DELAY. (D) THE THROUGH PORT DISPERSION. (E) THE DROP PORT DISPERSION. (F) THE THROUGH PORT POLE-ZERO DIAGRAM. (G) THE DROP PORT POLE-ZERO DIAGRAM. 55

FIGURE 3.3: THE CIRCUIT RESPONSE WITH $k = 0.525$ AND $k_o = k_{oo}$ INCREASING FROM 0.885 TO 0.985 IN STEPS OF 0.025. THE ARROWS INDICATE INCREASING PARAMETER VALUES. THE ROUND TRIP POWER LOSS IS 10%. (A) THE POWER SPECTRA. (B) THE PHASE VARIATION. (C) THE NORMALIZED GROUP DELAY. (D) THE THROUGH PORT DISPERSION. (E) THE DROP PORT DISPERSION. (F) THE THROUGH PORT POLE-ZERO DIAGRAM. (G) THE DROP PORT POLE-ZERO DIAGRAM. 57

FIGURE 3.4: THE CIRCUIT RESPONSE WITH $k = 0.525$ AND $k_o = k_{oo} = 0.935$ FOR A ROUND TRIP POWER LOSS OF 10%. (A) THE POWER SPECTRA. (B) THE PHASE VARIATION. (C) THE NORMALIZED GROUP DELAY. (D) THE THROUGH PORT DISPERSION. (E) THE DROP PORT DISPERSION. (F) THE THROUGH PORT POLE-ZERO DIAGRAM. (G) THE DROP PORT POLE-ZERO DIAGRAM. 59

FIGURE 3.5: A COMPOUND FOUR RING CIRCUIT ATTACHED TO A SINGLE RING STAGE. 59

FIGURE 3.6: THE SINGLE RING STAGE RESPONSE WITH $k_o = 0.952$ AND $k_{oo} = 0$ FOR A ROUND TRIP POWER LOSS OF 10%. (A) THE POWER SPECTRA. (B) THE PHASE VARIATION. (C) THE NORMALIZED GROUP DELAY. (D) THE THROUGH PORT DISPERSION. (E) THE THROUGH PORT POLE-ZERO DIAGRAM. 60

FIGURE 3.7: THE DROP PORT RESPONSE WITH AN ADDITIONAL SINGLE RING STAGE FOR A ROUND TRIP POWER LOSS EQUAL TO 10%. (A) THE POWER SPECTRA. (B) THE PHASE VARIATION. (C) THE NORMALIZED GROUP DELAY. (D) THE DROP PORT DISPERSION. (E) THE DROP PORT POLE-ZERO DIAGRAM. 61

FIGURE 3.8: THE CMT MODEL OF THE COMPOUND RING RESONATOR CIRCUIT. 65

FIGURE 3.9: (A) THE THROUGH PORT AND (B) THE DROP PORT TRANSMISSION CHARACTERISTICS FOR A LOSSLESS CIRCUIT, - - BY THE CMT MODEL (RED LINE), - BY THE CMS MODEL AND–O BY THE FDTD MODEL. THE SMALL SHIFT OF RESULTS BY THE CMS

AND THE CMT MODELS IS SHOWN IN THE INSET. THE RESONANCE WAVELENGTH CORRESPONDS TO $m=19$ 68
FIGURE 3.10: AS IN FIGURE (3.9) BUT FOR (A) THE THROUGH PORT AND (B) THE DROP PORT TRANSMISSION CHARACTERISTICS FOR A CIRCUIT WITH 5% POWER LOSS PER ROUND TRIP 69
FIGURE 3.11: AS IN FIGURE 3.9 BUT FOR (A) THE THROUGH PORT AND (B) THE DROP PORT TRANSMISSION CHARACTERISTICS FOR A CIRCUIT WITH 10% POWER LOSS PER ROUND TRIP. 70
FIGURE 3.12: THE SINGLE-MODE SOI WAVEGUIDE CROSS-SECTION..... 72
FIGURE 3.13: A SCHEMATIC OF THE PROPOSED CIRCUIT WITH RINGS REPLACED WITH RACETRACKS. 73
FIGURE 3.14: THE CHARACTERIZATION SETUP WITH DIFFERENT PARTS LABELED. POSITIONER (1) HOLDS THE INPUT FIBER; WHILE POSITIONER (2) HOLDS THE OUTPUT FIBER AND POSITIONER (3) HOLDS THE CHIP UNDER TEST. 74
FIGURE 3.15: (A) THE LAYOUT OF THE SIX COPIES OF THE PROPOSED CIRCUIT IN SECTION 3.2. THE TWO DEVICES ON THE RIGHT MOST (1, 2), TWO IN THE MIDDLE (3, 4) AND TWO ON THE LEFT MOST (5, 6) OF THE CHIP CORRESPOND TO THE DIMENSIONS ON THE 1^{ST}, 2^{ND} AND 3^{RD} ENTRIES IN TABLE 3.3 RESPECTIVELY, (B) THE LAYOUT OF DEVICE (1) SHOWING THE INPUT, THROUGH AND DROP PORTS. ON THE RIGHT IS THE TAPERED WAVEGUIDES FOLLOWED BY THE GRATING COUPLERS. 75
FIGURE 3.16: SEM PICTURES FOR THE FABRICATED (A) DEVICE (1) WITH $g=0.2\mu m$, (B) DEVICE (3) WITH $g=0.3\mu m$ AND (C) DEVICE (5) WITH $g=0.4\mu m$ 76
FIGURE 3.17: AN OPTICAL PHOTO FOR SOME THE FABRICATED CIRCUITS. 76
FIGURE 3.18: MEASURED AND THEORETICAL TRANSMISSION CHARACTERISTICS OF (A) THE THOUGH PORT OF DEVICE (A), (B) THE DROP PORT OF DEVICE (A), (C) THE THROUGH PORT OF DEVICE (B) AND (D) THE DROP PORT OF DEVICE (B). 78
FIGURE 3.19: MEASURED AND THEORETICAL TRANSMISSION CHARACTERISTICS AS IN FIGURE 3.18 BUT WITH MODIFIED FIELD COUPLING COEFFICIENTS. 81

FIGURE 4.1: (A) A RING ROTATING ABOUT A CENTER OF ROTATION AT A DISTANCE R_o FROM ITS CENTER, (B) A FIBER OPTIC GYROSCOPE (FOG) AND (C) A SINGLE RING GYROSCOPE. 85
FIGURE 4.2: CROW GYROSCOPE WITH $N = 5$ 87
FIGURE 4.3: CLR GYROSCOPE WITH $N = 4$ 88
FIGURE 4.4: A CROW CIRCUIT PERFORMANCE WITH $\lambda_o = 1.55\ \mu m$ (A) THE NORMALIZED OUTPUT POWER AT PORT B AS A FUNCTION OF ROTATIONAL SPEED (Ω) FOR A CROW WITH $R = 25\ \mu m$, $\alpha = 0$ AND $k = k_o = k_{oo} = \sqrt{\kappa} = 0.1$, (B) THE RELATIVE SENSITIVITY AS A FUNCTION OF THE ROTATIONAL SPEED FOR THE SAME CROW WITH $R = 25\ \mu m$, $\alpha = 0$, AND $k = k_o = k_{oo} = \sqrt{\kappa} = 0.1$, (C) THE CROW SENSITIVITY AS A FUNCTION OF THE POWER COUPLING COEFFICIENT (κ) WITH $N = 9$, $\Omega = 1000Hz = 2000\pi\ r/s$, $R = 25\mu m$ AND $\alpha = 0$, (D) THE CROW SENSITIVITY AS A FUNCTION OF THE RING RADIUS (R) WITH $N = 9$, $\alpha = 0$, $\Omega = 1000Hz = 2000\pi\ r/s$ AND $k = k_o = k_{oo} = \sqrt{\kappa} = 0.1$ 91
FIGURE 4.5: (A) THE NORMALIZED POWER TRANSMISSION OF A CROW GYROSCOPE WITH $N = 81$, $R = 5\,cm$, $\kappa = 0.001$ AND $\alpha = 0.2\,dB/km$ AT $\lambda_o = 1.55\,\mu m$. (B) THE SENSITIVITY OF THE CROW GYROSCOPE AND ITS EQUIVALENT FOG OF $R_f = 45\,cm$, $N_f = 3923$ turns, AND $L_f = 11093\,m$. 92
FIGURE 4.6: THE SENSITIVITY AS A FUNCTION OF N AND R WITH $\lambda_o = 1.55\,\mu m$ AND $\alpha = 0$, (A) A CROW GYROSCOPE, (B) A CLR GYROSCOPE. 94
FIGURE 4.7: THE SENSITIVITY AS A FUNCTION OF N AND R WITH $\lambda_o = 1.55\ \mu m$ AND $\alpha = 0.2\,dB/km$, (A) A CROW GYROSCOPE, (B) A CLR GYROSCOPE. 95
FIGURE 4.8: THE SENSITIVITY AS A FUNCTION OF N AND R WITH $\lambda_o = 0.633\ \mu m$ AND $\alpha = 7\,dB/km$, (A) A CROW GYROSCOPE, (B) A CLR GYROSCOPE. 96
FIGURE 4.9: THE SENSITIVITY OF THE EQUIVALENT FOG FOR (A) CROW GYROSCOPES AND (B) FOR CLR GYROSCOPES, WITH $\lambda_o = 1.55\ \mu m$ AND $\alpha = 0.2\,dB/km$. 98
FIGURE 4.10: THE SENSITIVITY OF THE EQUIVALENT SINGLE RING GYROSCOPE FOR (A) CROW GYROSCOPES AND (B) FOR CLR GYROSCOPES, WITH $\lambda_o = 1.55\ \mu m$ AND $\alpha = 0.2\,dB/km$. 99

List of Tables

TABLE 1.1 : WG1 STRUCTURE. 7

TABLE 1.2 : WG2 STRUCTURE. 8

TABLE 2.1; WAVEGUIDE REFRACTIVE INDICES. 34

TABLE 2.2: WAVEGUIDE CROSS SECTION DIMENSIONS. 35

TABLE 2.3: COMPARISON OF FOUR TUNABLE RING RESONATOR CIRCUITS WHERE OUR 'SECOND DESIGN' PARAMETERS ARE SHOWN BETWEEN BRACKETS. 40

TABLE 2.4: CIRCUIT PARAMETERS FOR $L = 40.05\ \mu m$ 46

TABLE 2.5: CIRCUIT PARAMETERS FOR $L = 80\ \mu m$ 47

TABLE 3.1: THE PERFORMANCE OF THE OPTIMAL DESIGN IN [43] COMPARED TO THE "COMPOUND RR CIRCUIT" PERFORMANCE. 63

TABLE 3.2: SINGLE MODE SOI WAVEGUIDE PARAMETERS. 72

TABLE 3.3: DIMENSIONS OF THE RACETRACKS IN μm WITH $L_2 = 0$ 73

Chapter 1

Introduction

Integrated optics is increasingly employed in miniaturizing components that perform fundamental processing functions such as generating, detecting, filtering, amplifying, routing and multiplexing of signals in telecommunications and data processing systems. While standard integrated optics components such as arrayed waveguides and multi-mode interference (MMI) devices are well established in device applications, the ring resonator (RR) is becoming increasingly competitive in alternative designs because of its small size and functionality. The objective of this thesis is to propose new RR based circuits that are optimized for high speed applications. Here we build on previous work that has included the application of ring resonators to integrated RR cavities, [0] have been employed in numerous contexts such as polarization converters [2], filters [3] optical delay lines [4], demultiplexers [5], reflectors [6], rotational motion detectors [7-8] and logic circuits [9]. Fabrication platforms for RR devices include silicon over insulator (SOI) [10], polymers [11-13] and group III-V semiconductors [14-15].

Accordingly, in the first chapter of this thesis we overview the waveguide theory and then demonstrate the manner in which RR device parameters are calculated in order to establish the basic principles of the RR circuit operation. In the next chapter we propose a novel hybrid ring resonator structure that employs the best features of two well established platforms, namely, polymer and SOI to obtain a high tuning speed while preserving compatibility with CMOS technology. In Chapter 3, we study a ring resonator (RR) structure with internal feedback that label a "compound ring resonator structure" and demonstrate the distinguished features of this structure by incorporating it into a standard wavelength division multiplexing (WDM) interlaver/deinterleaver circuit. We then analyze this circuit with three numerical approaches, the coupling of modes in space (CMS), the coupling of modes in time (CMT) and the finite difference time domain (FDTD) simulations. We further design the circuit layout and fabricate copies of the device for testing. The measurements agree well with theoretical calculations except for minor deviations that presumably could be eliminated with a more optimized design. In Chapter 4 we apply our RR design to gyroscopes for rotational motion detection and compare the performance to previously proposed RR based gyroscopes. We confirmed as other authors have noted previously that a single resonant ring provides a higher sensitivity than any more complex design proposed to date. We finally conclude our work and discuss possible future avenues for exploration.

1.1 Electromagnetic Background

To begin, we discuss electromagnetic field propagation in a 2D waveguide [16] followed by the effective index method (EIM) [17-20], which is useful to reduce a 3D waveguide into 2D. Next, we discuss electromagnetic field propagation in a 2D ring waveguide [21] and finally we overview the beam propagation method (BPM) that forms the basis for the waveguide simulator employed in much of the remainder of this thesis [22-28].

1.1.1 Light propagation in a two dimensional straight waveguide

We now evaluate the complex propagation constant of the electromagnetic modes in a waveguide, $\gamma = \beta - i\alpha/2$, where α is the power loss coefficient, $\beta = 2\pi n_e / \lambda_o$ is the mode propagation constant, n_e is the mode effective refractive index and λ_o is the free space wavelength which is set to $\lambda_o = 1.55\mu m$ in this work unless otherwise specified. In this section we further specialize to lossless waveguides with $\alpha = 0$ and we follow the treatment in [16].

Consider the 2D waveguide shown in Figure 1.1, where the waveguide core consists of a dielectric layer lying in the $y-z$ plane within $-w/2 \le x \le w/2$. The layer permittivity is $\varepsilon_1 = n_1^{\,2}\varepsilon_o$ with ε_o being the free space permittivity and n_1 the core refractive index (RI). The superstrate layer covers the top of the core in $w/2 < x < \infty$ with $\varepsilon_2 = n_2^{\,2}\varepsilon_o$ while the substrate layer extends in the region $-\infty < x < -w/2$ with $\varepsilon_3 = n_3^{\,2}\varepsilon_o$. Typically, the RI values of the three layers have the relation $n_1 > n_3$ and $n_1 > n_2$. The waveguide is considered a 2D waveguide since all layers are assumed infinite in the y direction and consequently for a wave propagating in the *z* direction the fields do not vary in this y direction. Since metallic boundaries are not employed, the waveguide is termed an open waveguide for which the fields vanish at $x = \pm\infty$.

The electric field intensity, $\vec{E}$, and the magnetic field intensity, $\vec{H}$ of modal fields with a monochromatic frequency dependence given by $e^{i\omega t}$, where $\omega = c_0 / \lambda_o$ is the field angular frequency, are given by:

$$\vec{E}(x,y,z) = E_x(x)e^{i\omega t - i\gamma z}\hat{x} + E_y(x)e^{i\omega t - i\gamma z}\hat{y} + E_z(x)e^{i\omega t - i\gamma z}\hat{z} \qquad \textbf{(1.1.a)}$$

$$\vec{H}(x,y,z) = H_x(x)e^{i\omega t - i\gamma z}\hat{x} + H_y(x)e^{i\omega t - i\gamma z}\hat{y} + H_z(x)e^{i\omega t - i\gamma z}\hat{z} \qquad \textbf{(1.1.b)}$$

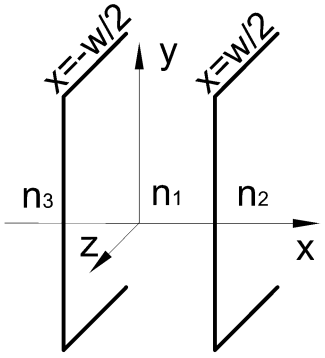

Figure 1.1: A 2D waveguide with core width w, core RI n_1, cladding RI n_2 and substrate RI n_3

Maxwell's equations in a non-magnetic dielectric material are:

$$\nabla \times \vec{E} = -\frac{\partial \mu_o \vec{H}}{\partial t} = -i\omega\mu_o \vec{H} \quad \textbf{(1.2.a)}$$

$$\nabla \times \vec{H} = \frac{\partial \varepsilon \vec{E}}{\partial t} = i\omega\varepsilon \vec{E} \quad \textbf{(1.2.b)}$$

where μ_o is the free space permeability. For a modal field, $\frac{\partial}{\partial y} = 0$ and $\frac{\partial}{\partial z} = -i\beta$ so that:

$$H_x = -\frac{\beta}{\omega\mu_o} E_y \quad \textbf{(1.3.a)}$$

$$H_z = \frac{i}{\omega\mu_o} \frac{\partial E_y}{\partial x} \quad \textbf{(1.3.b)}$$

$$i\beta H_x + \frac{\partial H_z}{\partial x} = -i\omega\varepsilon_j E_y \quad \textbf{(1.3.c)}$$

and

$$E_x = \frac{\beta}{\omega\varepsilon_j} H_y \quad \textbf{(1.4.a)}$$

$$E_z = \frac{-i}{\omega\varepsilon_j} \frac{\partial H_y}{\partial x} \quad \textbf{(1.4.b)}$$

$$i\beta E_x + \frac{\partial E_z}{\partial x} = i\omega\mu_o H_y \quad \textbf{(1.4.c)}$$

where $\varepsilon_j = n_j^{\,2}\varepsilon_o$ represents the layer j. The first set represents the transverse electric (TE) field mode where the electric field lies in the y-direction and the two magnetic field components can be derived from E_y. Similarly, the second set of equations represents the transverse magnetic (TM) mode for which the magnetic field is instead in the y-direction and the two electric field components can be computed from H_y. In either case the scalar wave equation holds so that:

$$\frac{\partial^2 E_y}{\partial x^2} + (k_j{}^2 - \beta^2)E_y = 0 \qquad \textbf{(1.5.a)}$$

and

$$\frac{\partial^2 H_y}{\partial x^2} + (k_j{}^2 - \beta^2)H_y = 0 \qquad \textbf{(1.5.b)}$$

respectively, where $k_j = n_j k_o$, $j = 1,2$ and 3, $k_o = \frac{2\pi}{\lambda_o} = \frac{\omega}{c}$ is the free space propagation constant, and c is the vacuum speed of light. For a guided mode, $k_1 > \beta > k_3 > k_2$ or equivalently $n_1 > n_e > n_3 > n_2$ and consequently we expect the solution to the TE and TM equations to take the form:

$$E_y = \begin{cases} A_2 e^{-k_{x2}(x-w/2)}: & w/2 < x < \infty \\ A_1 \cos(k_{x1}x) + B_1 \sin(k_{x1}x): & -w/2 \le x \le w/2 \\ A_3 e^{k_{x3}(x+w/2)}: & -\infty < x < -w/2 \end{cases} \qquad \textbf{(1.6.a)}$$

and

$$H_y = \begin{cases} A_5 e^{-k_{x2}(x-w/2)}: & w/2 < x < \infty \\ A_4 \cos(k_{x1}x) + B_2 \sin(k_{x1}x): & -w/2 \le x \le w/2 \\ A_6 e^{k_{x3}(x+w/2)}: & -\infty < x < -w/2 \end{cases} \qquad \textbf{(1.6.b)}$$

respectively, where $k_{x1} = \sqrt{k_1{}^2 - \beta^2}$, $k_{x2} = \sqrt{\beta^2 - k_2{}^2}$ and $k_{x3} = \sqrt{\beta^2 - k_3{}^2}$ are the transverse propagation constants in the regions $j = 1,2$ and 3 respectively. Also, $A_{1\to 6}$, B_1 and B_2 are constant values to be determined through the boundary condition and power normalization. The boundary conditions applied at $x = \pm w/2$ result from the continuity of the tangential electric and magnetic field components, namely E_y and H_z for the TE mode and H_y and E_z for the TM mode. This leads to the dispersion relation:

$$2v\sqrt{1-b} = m\pi + \tan^{-1}(q_3{}^2\sqrt{\frac{b}{1-b}}) + \tan^{-1}(q_2{}^2\sqrt{\frac{b+\eta}{1-b}}) \qquad \textbf{(1.7)}$$

where

$$q_j = \begin{cases} 1: & \text{for the TE mode} \\ n_1 / n_j : & \text{for the TM mode} \end{cases} \tag{1.8.a}$$

$$\eta = \frac{\left| n_2^{\,2} - n_3^{\,2} \right|}{n_1^{\,2} - \max\left\{ n_2^{\,2}, n_3^{\,2} \right\}} \tag{1.8.b}$$

$$b = \frac{n_e^{\,2} - \max\left\{ n_2^{\,2}, n_3^{\,2} \right\}}{n_1^{\,2} - \max\left\{ n_2^{\,2}, n_3^{\,2} \right\}} \tag{1.8.c}$$

$$v = k_o \frac{w}{2} \sqrt{n_1^{\,2} - \max\left\{ n_2^{\,2}, n_3^{\,2} \right\}} \tag{1.8.d}$$

In the present case $\max\left\{ n_2^{\,2}, n_3^{\,2} \right\} = n_3^{\,2}$ since $n_3 \succ n_2$. The parameters b and v are called the normalized propagation constant and the normalized frequency respectively while m is an integer termed the mode order such that $m = 0$ defines the fundamental mode with the largest β, while η measures the asymmetry of the cladding refractive indices with $\eta = 0$ for a symmetric waveguide, i.e. $n_3 = n_2$. The dispersion relation can then be solved graphically or numerically.

While in the 2D problem the modes are TE and/or TM, in 3D rectangular waveguides the modes are hybrid. While approximate analytic methods can be applied, the simplified effective index method (EIM) detailed in the subsequent section [17-20] yields good numerical estimates of the propagation constants for many 3D waveguide structures.

1.1.2 Effective index method (EIM)

We consider first the 3D rectangular waveguide of Figure 1.2 with core dimensions labeled $w \times t_1$ and RI n_1 which divides the surrounding space into 8 regions with refractive indices n_j where $j = 2,3,..,9$. The substrate normally comprises the three regions given by $j = 3,4,9$. While pure TE or TM modes do not exist, the modes are either TE-like modes with a dominant electric field component E_x parallel to the substrate or TM-like modes with E_y normal to the substrate [16].

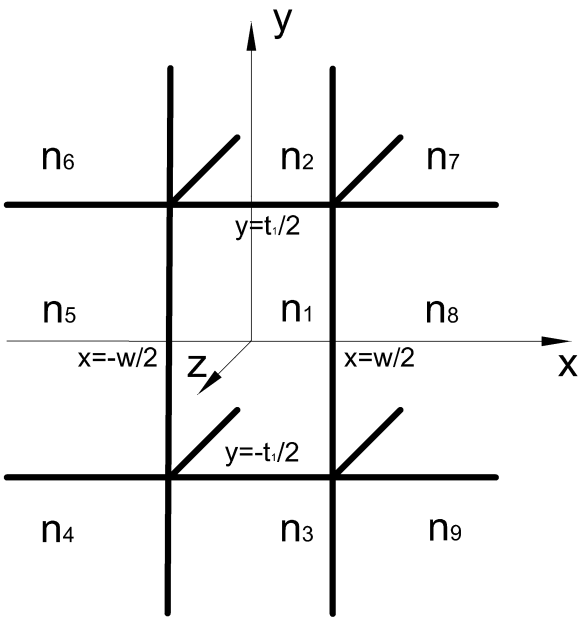

Figure 1.2: Three dimensional waveguide

The EIM calculation of n_e of a TE-like mode [17-20] first extends the $j = 1,2,3$ regions to infinity in the x-direction as shown in Figure 1.3.a and determines the effective RI of this structure n_{e1} from the dispersion relation of equation (1.7). Recall that the TE-like mode of the 3D waveguide in Figure 1.2 has its dominant electric field parallel to the substrate, i.e. in the x-direction motivating the choice of the TE mode for the 2D waveguide calculation. Next, the regions given by $j = 1,5,8$, are extended to infinity in the y-direction while n_1 is replaced with n_{e1} so that the 2D waveguide of Figure 1.3.b is obtained. The effective refractive index of the TE-like mode of the three-dimensional structure is then approximated as n_e of this 2D waveguide TM mode, since the TM mode in this step corresponds to the polarization of the TE-like 3D mode.

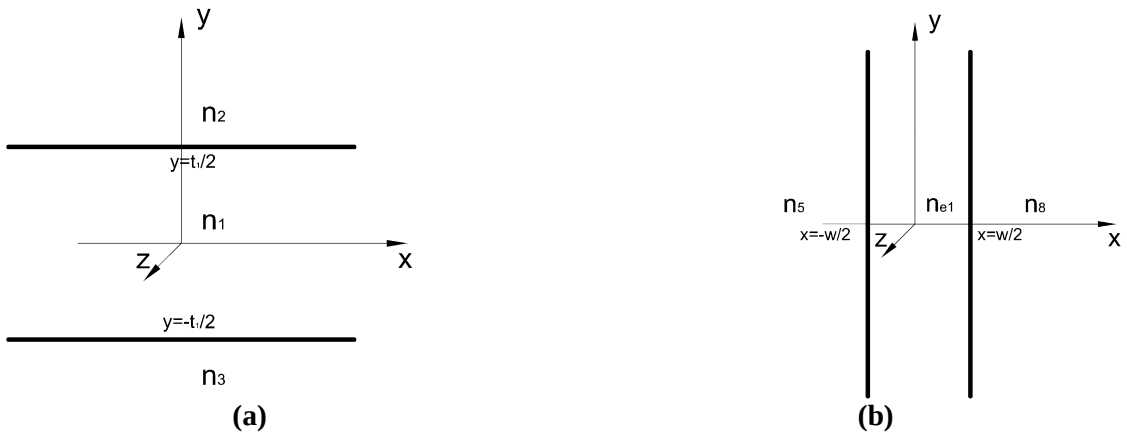

Figure 1.3: (a) The 2D waveguides representing the (a) first and (b) second step of the EIM

The 2D waveguide shown in Figure 1.3.b. can also be employed to calculate properties such as the coupling ratio or the bending loss. The steps of the EIM are slightly different for other 3D waveguide structures such as the rib waveguide, c.f. [19-20].

The two 3D single-mode rectangular waveguides employed in this thesis are labeled WG1 and WG2 and are defined in Table 1.1 and Table 1.2 and Figure 1.4 and Figure 1.5 respectively. Power loss coefficients appear in these tables correspond to scattering loss, as will be discussed later, since this is the main power loss mechanism in these waveguides.

Property	Value
Core width (w)	$0.3\,\mu m$ [29]
Core height (t_1)	$0.3\,\mu m$ [29]
Silicon core RI (n_1)	3.474[29]
Buried Silica RI ($n_3 = n_4 = n_5 = n_8 = n_9$)	1.444 [29]
Polymer (CLD1/APC) layer RI (n_2)	1.612 [12]
Air RI ($n_6 = n_7$)	1
Scattering power loss coefficient (α)	$6\,dB/cm$[30]

Table 1.1 : WG1 structure.

Property	Value
Core width (w)	$0.5\ \mu m$
Core height (t_1)	$0.22\ \mu m$
Silicon core RI (n_1)	3.474[29]
Buried Silica RI ($n_3 = n_4 = n_9$)	1.444 [29]
Air RI ($n_2 = n_5 = n_6 = n_7 = n_8$)	1
Scattering power loss coefficient (α)	$2.4\ dB/cm$ [31-32]

Table 1.2 : WG2 structure.

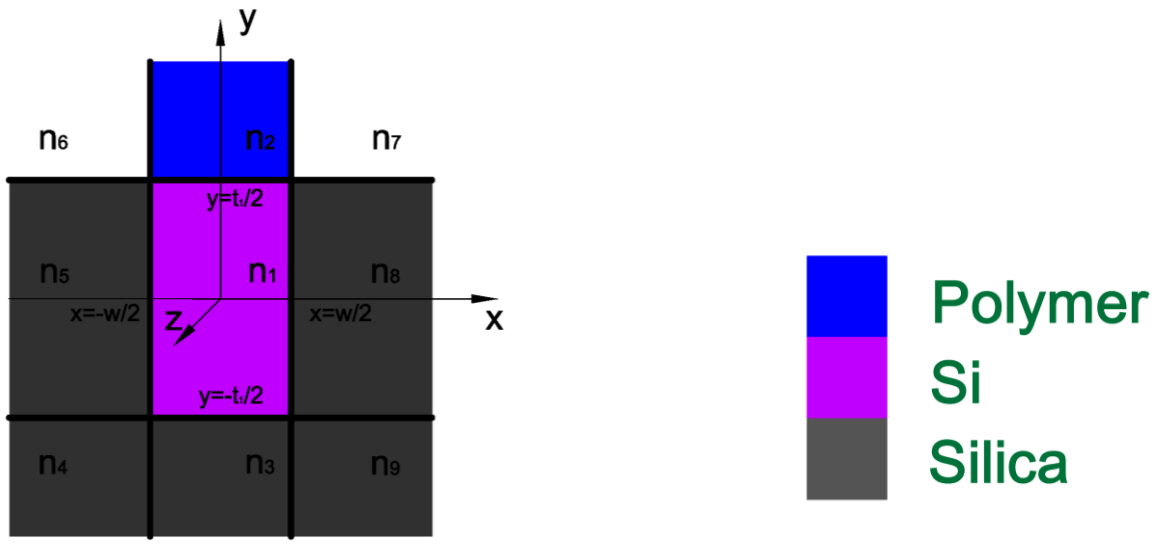

Figure 1.4: WG1 structure. Different material regions are colored differently

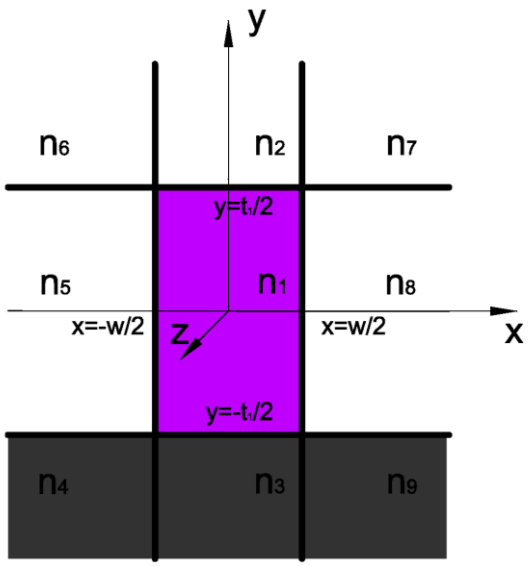

Figure 1.5: WG2 structure.

As a numerical example of the EIM, we calculate n_e for the TE-like mode of WG1. In the first step, the 3D structure is reduced to 2D as in Figure 1.3.a with the waveguide asymmetry coefficient $\eta = \dfrac{\left|n_2^{\,2} - n_3^{\,2}\right|}{n_1^{\,2} - \max\left\{n_2^{\,2}, n_3^{\,2}\right\}} = 0.0542$, thickness $t_1 = 0.3\mu m$ and normalized frequency $v = k_o \dfrac{w}{2}\sqrt{n_1^{\,2} - \max\left\{n_2^{\,2}, n_3^{\,2}\right\}} = 1.8712$. The corresponding b-v diagram is shown in Figure 1.6 where the vertical line marks the value of v. The corresponding value of the normalized propagation constant is given by the intersection of the vertical line and the TE curve of the fundamental mode with $m = 0$, yielding $b = \dfrac{n_{e1}^{\,2} - \max\left\{n_2^{\,2}, n_3^{\,2}\right\}}{n_1^{\,2} - \max\left\{n_2^{\,2}, n_3^{\,2}\right\}} = 0.654$ and $n_{e1} = 2.97$. Next we compute the TM mode of the 2D waveguide shown in Figure 1.3.b, with a core RI $n_{e1} = 2.9651$ and the two cladding layers with $n_5 = n_8 = 1.444$. The core thickness is $w = 0.3\mu m$. The corresponding b-v diagram is shown in Figure 1.7. For this symmetric 2D waveguide, $\eta = 0$ and $v = 1.5747$. Similarly, $b = 0.396$ is given by the intersection of the vertical line $v = 1.5747$ and the TM mode curve with $m = 0$ yielding finally $n_e = 2.18$.

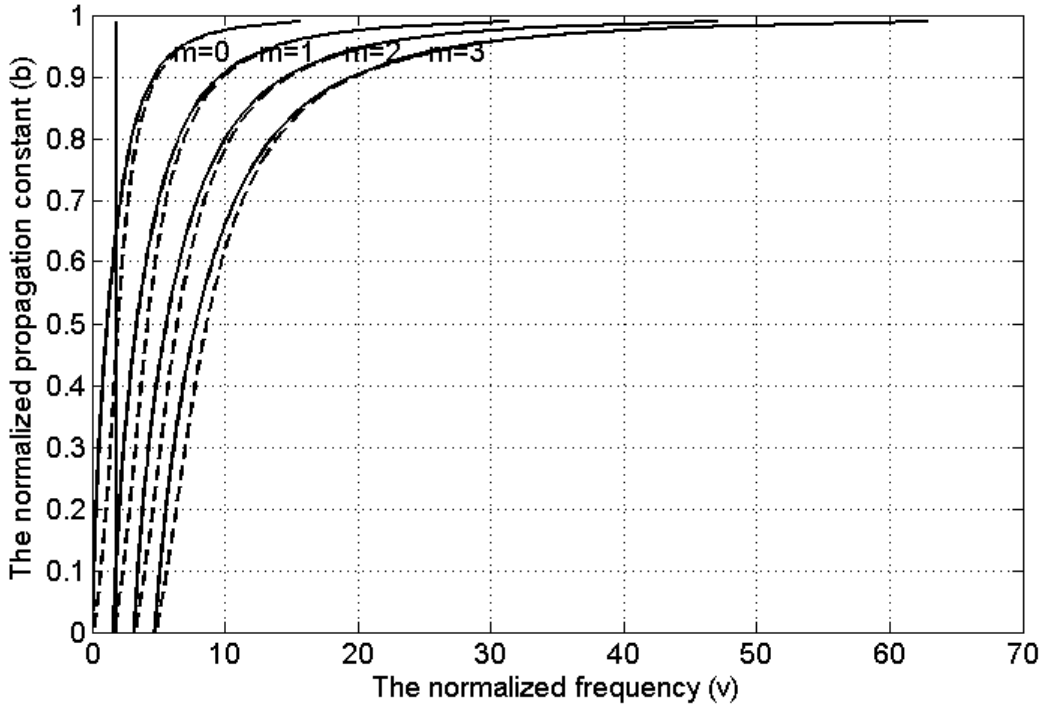

Figure 1.6: b-v diagram for the reduced WG1 as in the first step of the EIM. Solid (dotted) line curves represent TE (TM) modes.

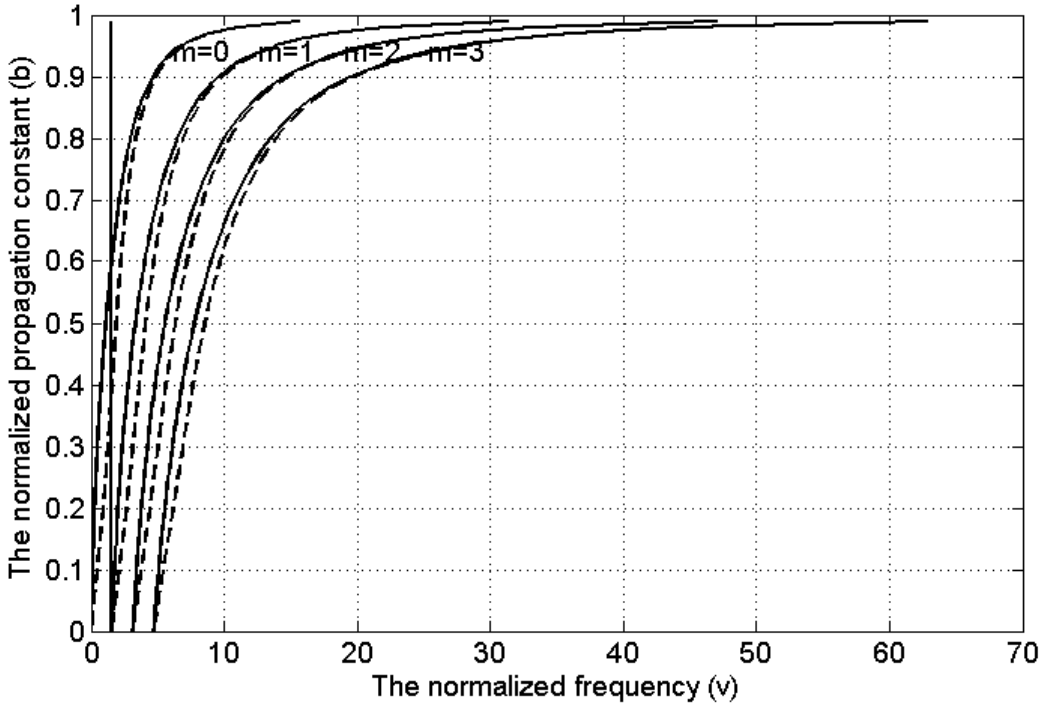

Figure 1.7: b-v diagram for the reduced WG1 as in the second step of the EIM. Solid (dotted) line curves represent TE (TM) modes.

For WG2, the n_e of the TE-like mode, is obtained first from n_{e1} of the TE mode for the field in the configuration of Figure 1.3.a with RI values from Table 1.2 and $t_1 = 0.22\ \mu m$. This yields $\eta = 0.1087,\ v = 1.4089,\ b = 0.556$ and hence $n_{e1} = 2.76$. In the second step we solve for the TM mode of the configuration in Figure 1.3.b employing the value of n_{e1} from the first step, $n_5 = n_6 = 1$ and $w = 0.5\ \mu m$ to obtain $\eta = 0, v = 2.6106,\ b = 0.667$ and $n_e = 2.33$.

1.1.3 Light propagation in ring resonators

We next solve Maxwell's equations for the ring resonator of Figure 1.8 with mean radius R, core width w and refractive index (RI) n_1, surrounded by cladding layers of RI values n_2 in $0 \le r < R - w/2$ and n_3 in $r > R + w/2$ with r being the radial distance from the ring center. The structure is symmetric about the y axis which is normal to the page outward. We consider here the 2D problem so that the refractive index is invariant in both y and θ.

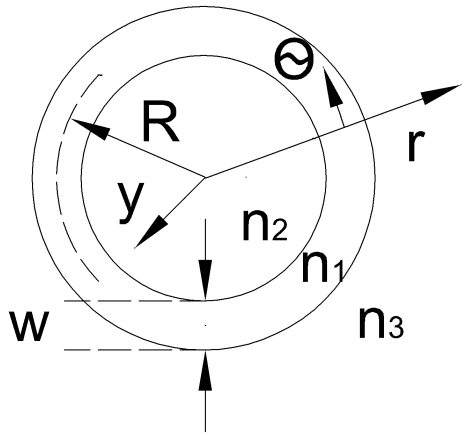

Figure 1.8: A ring resonator waveguide structure

Modal electric and magnetic field intensities can be respectively expressed as [21]:

$$E(r,\theta,y) = (E_r, E_\theta, E_y)e^{i\omega t - iR\gamma\theta} \qquad \textbf{(1.9.a)}$$

$$H(r,\theta,y) = (H_r, H_\theta, H_y)e^{i\omega t - iR\gamma\theta} \qquad \textbf{(1.9.b)}$$

where $\gamma = \beta - i\alpha/2$ is the complex propagation constant of the mode with the real part β and the power loss coefficient α. Substituting (1.9) into (1.2.a) yields two separate sets of equations:

$$\gamma \frac{R}{r} E_y = -\mu_o \omega H_r \qquad \textbf{(1.10.a)}$$

$$\frac{\partial E_y}{\partial r} = -i\mu_o \omega H_\theta \qquad \textbf{(1.10. b)}$$

$$-\frac{1}{r}\frac{\partial r H_\theta}{\partial r} - \frac{i\gamma R}{r} H_r = i n_j{}^2 \varepsilon_o \omega E_y \qquad \textbf{(1.10. c)}$$

and

$$\gamma \frac{R}{r} H_y = n_j{}^2 \varepsilon_o \omega E_r \qquad \textbf{(1.11.a)}$$

$$\frac{\partial H_y}{\partial r} = i n_j{}^2 \varepsilon_o \omega E_\theta \qquad \textbf{(1.11.b)}$$

$$\frac{1}{r}\frac{\partial r E_\theta}{\partial r} + \frac{i\gamma R}{r} E_r = i\mu_o \omega H_y \qquad \textbf{(1.11.c)}$$

where ε has been replaced by $n_j{}^2 \varepsilon_o$ with ε_o is the free space permittivity and n_j is the RI of layer j. Again for a TE mode the two magnetic field components can be expressed in terms of the single electric field component E_y while for a TM mode the two electric field components are given in terms of H_y.

For a TE mode, in each of the three regions with constant RI, the electric field obeys the Helmholtz wave equation:

$$\left(\frac{\partial^2}{\partial r^2} + \frac{1}{r}\frac{\partial}{\partial r} + n_j{}^2 k_o{}^2 - \left(\frac{\gamma R}{r}\right)^2\right) E_y = 0 \qquad \textbf{(1.12)}$$

Appropriate solutions to this equation in the three regions are given by:

$$E_y = \begin{cases} C_2 J_\nu(k_o n_2 r): & 0 \le r < R - w/2 \\ C_1 J_\nu(k_o n_1 r) + D_1 Y_\nu(k_o n_1 r): & R - w/2 \le r \le R + w/2 \\ C_3 H_\nu^{(2)}(k_o n_3 r): & R + w/2 < r < \infty \end{cases} \qquad \textbf{(1.13)}$$

since the field is everywhere finite and decays to zero as $r \to \infty$. The constants C_1, C_2, D_2 and C_3 are determined from the field normalization and the boundary conditions at the interfaces, $r = R - w/2$ and $r = R + w/2$, obtained from the continuity of E_y and H_θ. These yield the dispersion relation [21]:

$$\frac{\frac{J_\nu(k_o n_1(R-w/2))}{J_\nu(k_o n_2(R-w/2))} - q_2 \frac{J_\nu'(k_o n_1(R-w/2))}{J_\nu'(k_o n_2(R-w/2))}}{\frac{Y_\nu(k_o n_1(R-w/2))}{J_\nu(k_o n_2(R-w/2))} - q_2 \frac{Y_\nu'(k_o n_1(R-w/2))}{J_\nu'(k_o n_2(R-w/2))}} = \frac{\frac{J_\nu(k_o n_1(R+w/2))}{H_\nu^{(2)}(k_o n_3(R+w/2))} - q_3 \frac{J_\nu'(k_o n_1(R+w/2))}{H_\nu^{(2)}{}'(k_o n_3(R+w/2))}}{\frac{Y_\nu(k_o n_1(R+w/2))}{H_\nu^{(2)}(k_o n_3(R+w/2))} - q_3 \frac{Y_\nu'(k_o n_1(R+w/2))}{H_\nu^{(2)}{}'(k_o n_3(R+w/2))}} \quad \textbf{(1.14)}$$

with $q_j = n_1 / n_j$. For the TM mode, H_y and E_θ are continuous resulting in the dispersion relation with q_j replaced by $q_j = n_j / n_1$. In both cases $\gamma = \nu / R$ and therefore the modal propagation constant is obtained numerically. Alternatively, conformal mapping [33] replaces the bent waveguide with an equivalent graded index straight waveguide to which methods such as the Wentzel-Kramers-Brillouin (WKB) technique [33-34] can be applied.

These are however not trivial for bent waveguides and especially for 3D waveguides which generally require the EIM for a simplified analysis. However, ring resonators with $R >> w$, can be generally replaced by a straight waveguide with the same width and RI values for core and cladding layers [33-34], while bending contributes negligibly to α compared to surface scattering for most silicon over insulator (SOI) waveguides.

1.1.4 Beam propagation method (BPM)

The beam propagation method (BPM) [22-28] is a one-way marching algorithm for the Helmholtz scalar wave equation for small RI contrast waveguides, which in 3D Cartesian coordinates takes the form:

$$\left(\frac{\partial}{\partial x^2} + \frac{\partial}{\partial y^2} + \frac{\partial}{\partial z^2} + n^2 k_o^{\,2}\right) E = 0 \quad \textbf{(1.15)}$$

If z is the propagation direction, for paraxial fields, we can write $E = \tilde{E}(x, y, z) e^{i\omega t - i\bar{k}z}$ with $\bar{k} = k_o \bar{n}$ where $\bar{n}$ is normally chosen between the core and the cladding RI values [28]. Applying the slowly varying field envelope approximation, for which $\frac{\partial^2 E}{\partial z^2} << \frac{\partial E}{\partial z}$ yields:

$$\frac{\partial \tilde{E}}{\partial z} = \frac{1}{2i\bar{k}} \left(\frac{\partial^2}{\partial x^2} + \frac{\partial^2}{\partial y^2} + k_o^{\,2}(n^2 - \bar{n}^2)\right) \tilde{E} \quad \textbf{(1.16)}$$

An implicit finite-difference (FD) method based on the well-known Crank-Nicholson scheme [24], [26-27] can now be applied as in the commercial BeamPROP code employed later in this thesis. Here

the field is discretized on a set of grid points along the transverse plane. From the discretized field at the waveguide entrance, the field propagation is numerically evaluated at $z = n\Delta z$. While the above equation pertains to the propagation of scalar fields with small beam divergences, more complicated formulation applies to polarized field [35-36] and non-collimated propagation [25], [37]. Since however the method cannot be applied to two-way propagation as in a ring resonator, our calculations are applied to straight waveguides or effective straight waveguide profiles for which we calculate the mode profile, the propagation constant and field coupling between neighboring waveguides and propagation losses. An arc of central angle $\theta = 20^o$ is employed to estimate the bending losses or external coupling strengths of an RR as discussed later.

The BeamProp results for the n_e of the TE-like mode of WG1 and WG2 yield the mode profiles and normalized effective indices of Figure 1.9 and Figure 1.10 respectively. The normalized RI indices differ by approximately 0.05 for WG1 and 0.11 for WG2 between the EIM and the BPM. Since this yields considerable errors for quantities such as the coupling losses, 3D simulations are generally employed below.

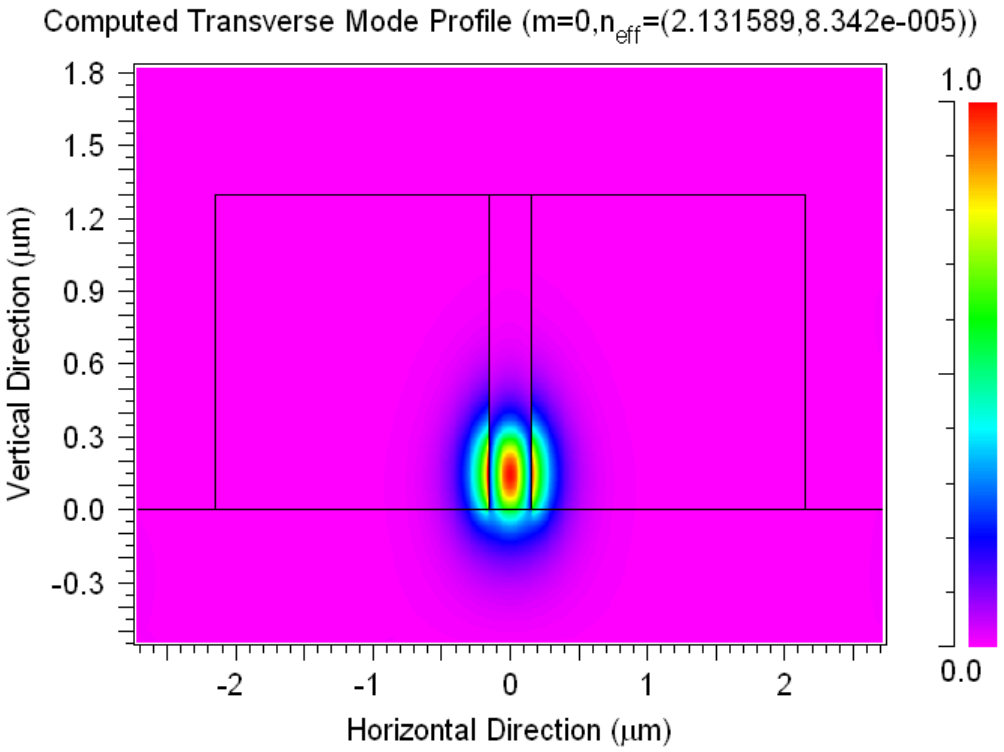

Figure 1.9: The TE-like mode for WG1 with the characteristics in Table 1.1

.

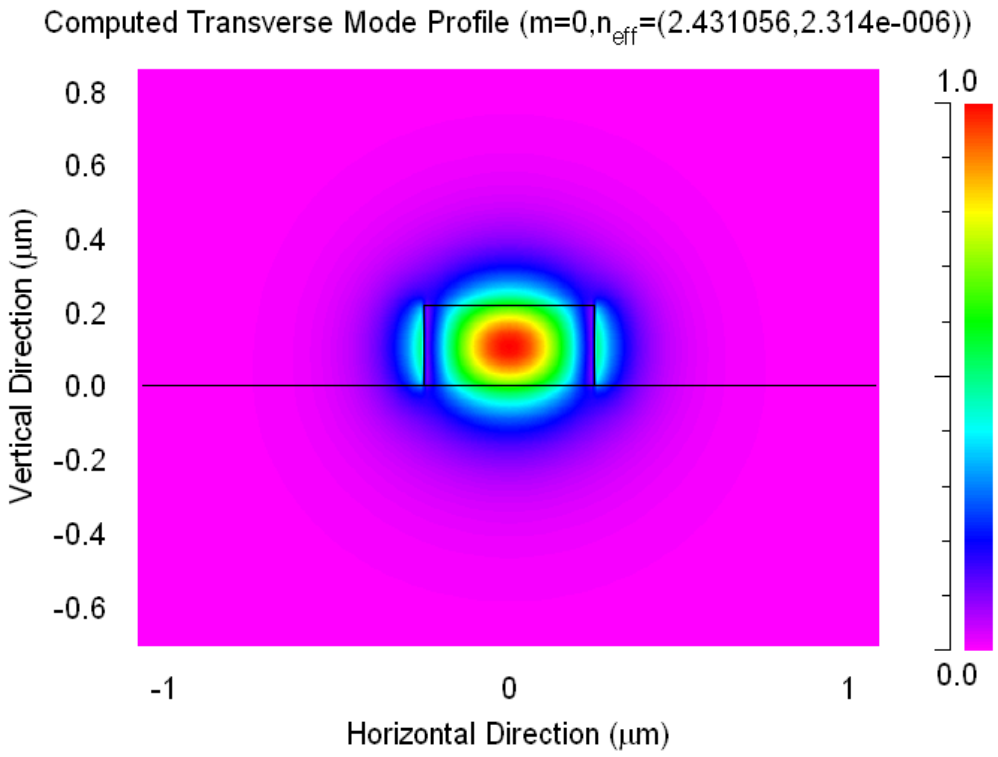

Figure 1.10: The TE-like mode for WG2 with the characteristics in Table 1.2.

1.2 Field coupling and bending loss calculations

We now apply the methods of the previous section to evaluate field coupling and the propagation losses.

1.2.1 Power coupling

Appreciable power can be exchanged between two waveguides that support modes with the same or nearly the same propagation constants when the modal fields appreciably overlap. The field coupling ratio, k represents the ratio of the coupled fields between the two waveguides and can be evaluated by the 'coupled mode theory' [3], [16], [38-40]. Here we consider two waveguides, (WGI) and (WGII) in close proximity as shown in Figure 1.11 .

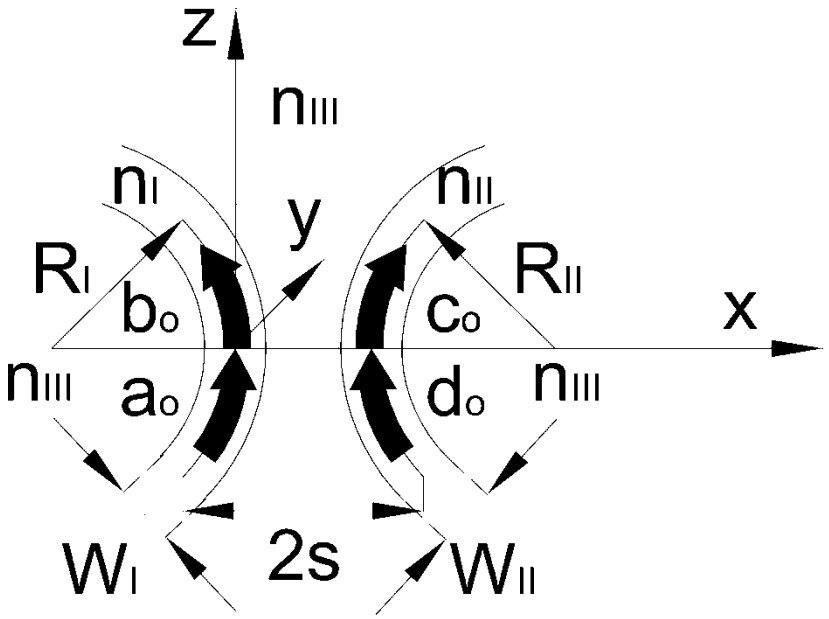

Figure 1.11: Two waveguides WGI and WGII, in close proximity.

Here the core RI, width and mean radius of curvature of WG_j are given by n_j, W_j and R_j respectively with $j = I, II$ while the surrounding media have an RI of n_{III} and The electric field components around the interaction region are given by a_o, b_o, c_o and d_o. If the waveguide center to center distance is $2s(z)$, the ratio of the field coupled from WGII into WGI is then [3], [38]:

$$k = \sin\left(\int_{\text{interaction region}} \kappa(2s(z)) e^{-j\Delta\beta z} dz \right) \qquad \textbf{(1.17)}$$

where $\Delta\beta = \beta_I - \beta_{II} = k_o(n_{eI} - n_{eII})$ is the difference of propagation constants of the waveguides and κ is the 'coupling coefficient' given by the overlap integral [3], [38]:

$$\kappa(s(z)) = \frac{\omega\varepsilon_o}{4} \int_{-w_I/2}^{w_I/2} (n_I{}^2 - n_{III}{}^2) E_I(x) E_{II}{}^*(x) dx \qquad \textbf{(1.18)}$$

where $E_I(x)$ and $E_{II}(x)$ are the electric fields of the modes of propagation of WGI and WGII respectively. For the TE mode described by equation (1.6.a) and the corresponding boundary conditions we arrive at:

$$\kappa(2s(z)) = \frac{\omega^2 \varepsilon_o \mu_o (n_I{}^2 - n_{III}{}^2)\cos(k_{xII} w_{II}/2) e^{k_{xIV}(w_{II}/2-2s)}}{\beta_1 (k_{xI}{}^2 + k_{xIV}{}^2)(w_I/2 + 1/k_{xIII})}$$
$$\times (k_{xIV}\cos(k_{xI} w_I/2)\sinh(k_{xIV} w_I/2) + k_{xI}\sin(k_{xI} w_I/2)\cosh(k_{xIV} w_I/2)) \quad \textbf{(1.19)}$$

where $k_{xI} = \sqrt{k_I{}^2 - \beta_I{}^2}$, $k_{xII} = \sqrt{k_{II}{}^2 - \beta_{II}{}^2}$, $k_{xIII} = \sqrt{\beta_I{}^2 - k_{III}{}^2}$, $k_{xIV} = \sqrt{\beta_{II}{}^2 - k_{III}{}^2}$, and $k_j = n_j k_o$, $j = I, II$ and III.

Since substituting equation (1.19) into (1.17) yields a complicated integral [38], we focus here on two simpler cases. For two straight waveguides interacting over a length L, the integration domain in equation (1.17) is $-L/2 \le z \le L/2$ while $2s(z)$ is replaced by the constant $2s_o$ in equation (1.19). Accordingly,

$$k = \sin\left(\frac{\kappa(2s_o) L \sin(X)}{X}\right) \quad \textbf{(1.20)}$$

with

$$X = \Delta\beta \; L/2 \quad \textbf{(1.21)}$$

If the two waveguides are symmetric, $\Delta\beta = 0$ and equation (1.20) reduces to:

$$k = \sin(\kappa L) \quad \textbf{(1.22)}$$

Then we define the coupling distance $\Lambda = \pi/(2\kappa)$ corresponds to the interaction length for complete power transfer from one straight waveguide to the other, i.e. $k = 100\%$.

For two waveguides with identical core RI, i.e. $n_I = n_{II}$, the center to center separation can be approximated by $s(z) \approx s_o + z^2/(2R_m)$ with $1/R_m = 1/R_I + 1/R_{II}$ [3], [38]. The field coupling ratio is then approximately [3]:

$$k = \sin(\kappa(2s_o) l_m) \quad \textbf{(1.23)}$$

where

$$l_m = \sqrt{\frac{\lambda_o R_m}{2\sqrt{n_{eII}{}^2 - n_{III}{}^2}}} \quad \textbf{(1.24)}$$

The EIM method can often be employed to reduce the problem to 2D before applying the above coupling formulae. The effective RI then replaces the core RIs, n_I or n_{II}.

An alternative is to employ the BeamProp as shown in

Figure 1.12. to calculate light coupling between two parallel waveguides separated by $2s_o = 0.7\ \mu m$ and excited by a TE polarized Gaussian beam in the left waveguide. Complete power transfer is observed at the coupling distance of $\Lambda = 47.5\ \mu m$, yielding $\kappa = \pi/(2\Lambda) = 0.033/\mu m$. The maximum power on the monitor plot is less than 100% since the initial field does not perfectly match the left waveguide mode.

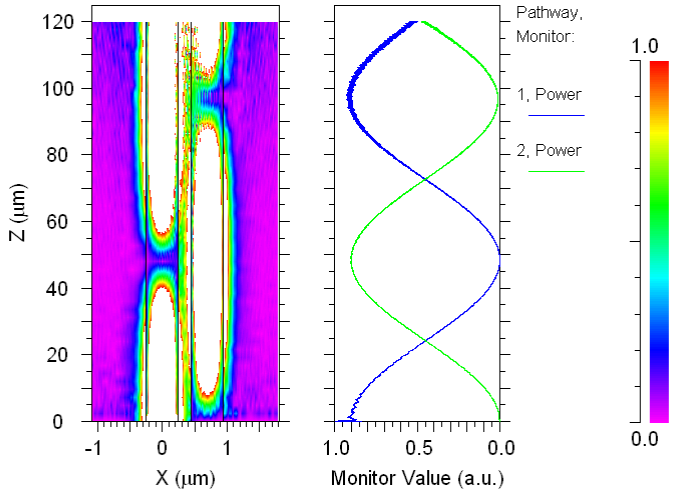

Figure 1.12: Coupling between two straight WG2 waveguides. The power profile is given by the left plot while the power level versus propagation direction is shown as the blue and green lines.

A similar procedure can be employed to calculate the coupling between a bus and a ring. While the beam propagation method is difficult to apply to propagation along a large angular region, propagating the field over a 20^o accurately represents the interaction region in our simulation [19]. Launching light into the straight waveguide and monitoring the remaining power in the straight waveguide after the interaction yields the results of Figure 1.13 for which the straight and curved waveguides exchange power across a gap of $g_o = 0.3\ \mu m$ so that $2s_o = w + g_o = 0.6\mu m$. The mean radius of the bent waveguide is $R = 50\ \mu m$. The blue and green lines on the monitor side display the power variation with z in the straight and bent waveguides, respectively. Because of the mismatch loss between the Gaussian excitation and the mode at the entrance face of the straight waveguide, the normalized power level is again less than 100%. The input power is coupled from the straight waveguide to the curved waveguide so that the power level decreases from approximately 88% to 28% for a TE-like mode and to 38% with a TM-like mode corresponding to $k^2 = 6/8.8$ for the TE-like and $k^2 = 5/8.8$ for the TM-like mode.

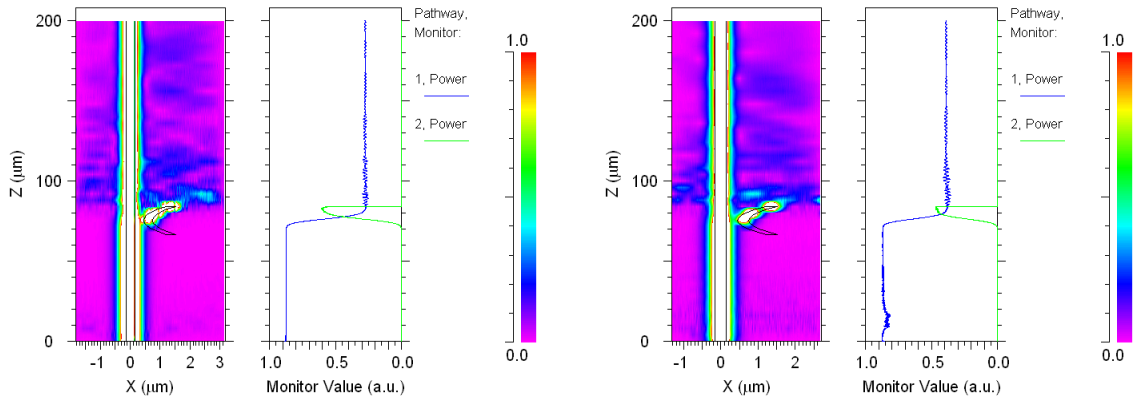

Figure 1.13: Power coupling between a straight and a curved waveguide for (a) TE-like and (b) TM-like modes.

1.2.2 Propagation loss factor

In straight waveguide segments, losses occur through scattering and intrinsic absorption losses. Bending losses are also present in curved waveguides while mode mismatch losses are present at interfaces between straight and bent segments. Since SOI waveguides should possess small cross sections in order to exhibit small fabrication footprints, single mode operation and small bending losses [10], side-wall roughness from fabrication imperfections can be of significant effect yielding scattering losses typically between $0.2\,dB/cm$ to $5\,dB/cm$ [10] that are examined both theoretically as well as experimentally in [10], [13], [29] and [41-42]. Additionally, power leakage into a lower refractive index substrate layer can occur if the buried oxide layer is not thick enough to suppress any overlap between the propagating mode and the silicon substrate. Typically this requires a $1\,\mu m$ thick silica layer [29]. Absorption losses are negligible for SOI waveguides operating at the telecommunications wavelength $\lambda_o = 1.55\ \mu m$ since the energy gap of silicon is $1.1\,ev$ [42].

Also, since the modal wave-front propagates with faster phase velocities far from the center of rotation of a bent waveguide, at a certain distance from the center, the wave-front would have to propagate with a phase velocity greater than the speed of light in the medium. Since this is not possible, bending losses are instead induced.

To decrease bending losses, the electric field must be tightly confined inside the waveguide core, which requires a large refractive index (RI) contrast between the waveguide core and cladding. Indeed, SOI provides larger contrast than most other platforms such as polymers, since the RI contrast is approximately 2 for SOI waveguides. This enables small bending radius waveguides ($R > 5\mu m$) with negligible bending losses [32] that can be employed in e.g. large free spectral range (FSR) WDM multiplexers as will be discussed in Chapter 3. An illustration using BeamPROP is presented in Figure 1.14

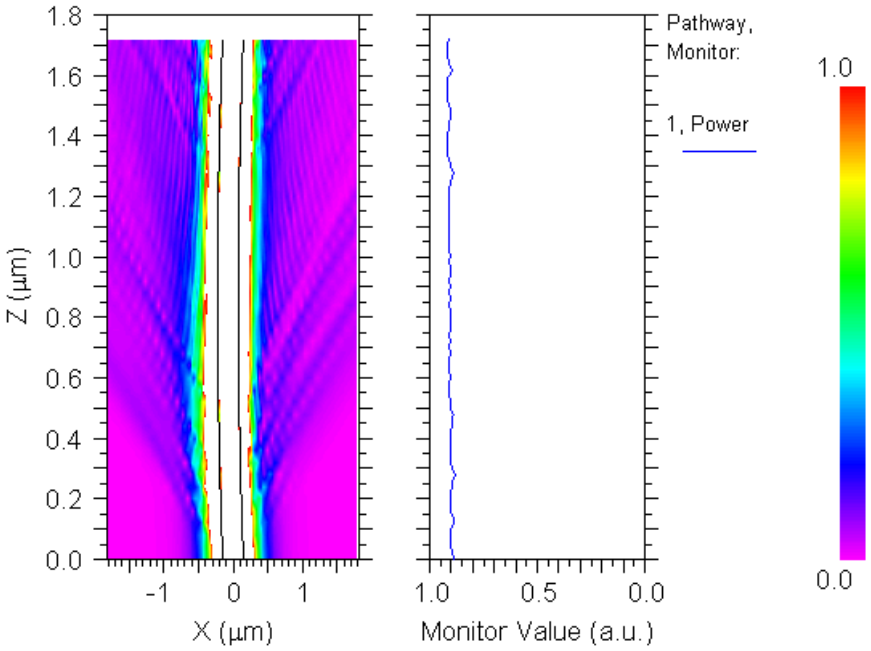
Z (μm)
X (μm)
Monitor Value (a.u.)
Pathway,
Monitor:
1, Power
1.0
0.0

(a)

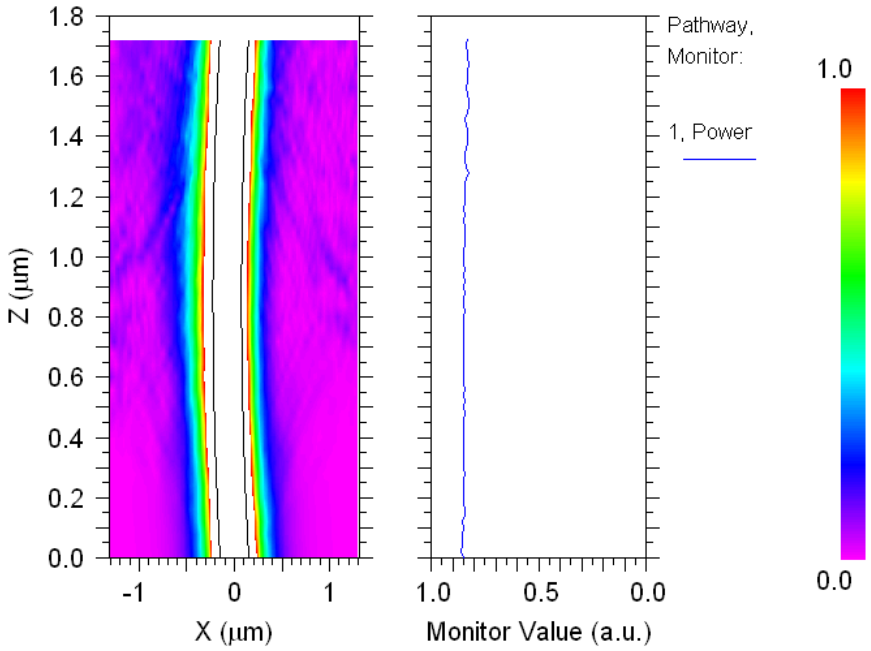
Z (μm)
X (μm)
Monitor Value (a.u.)
Pathway,
Monitor:
1, Power
1.0
0.0

(b)

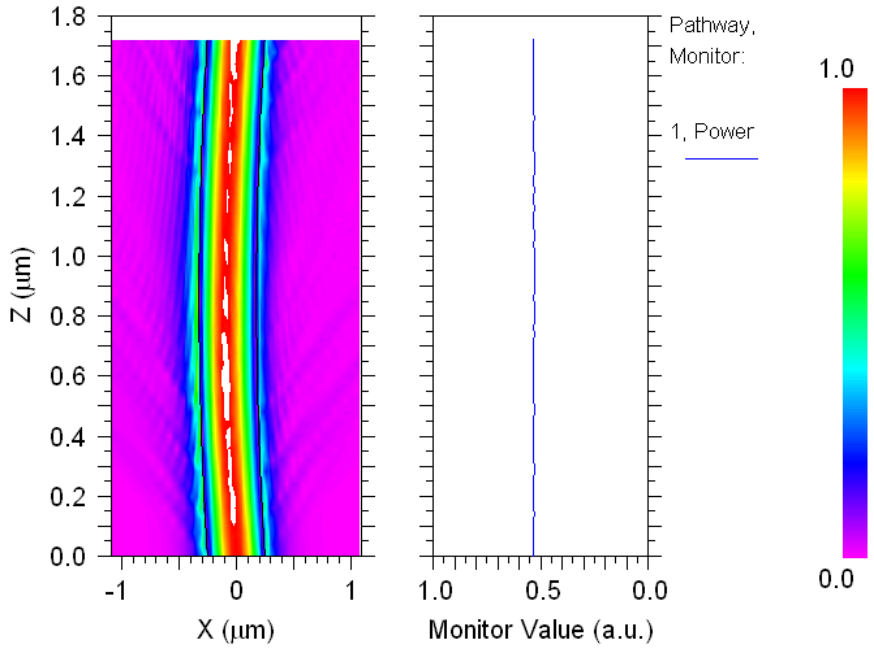

(c)

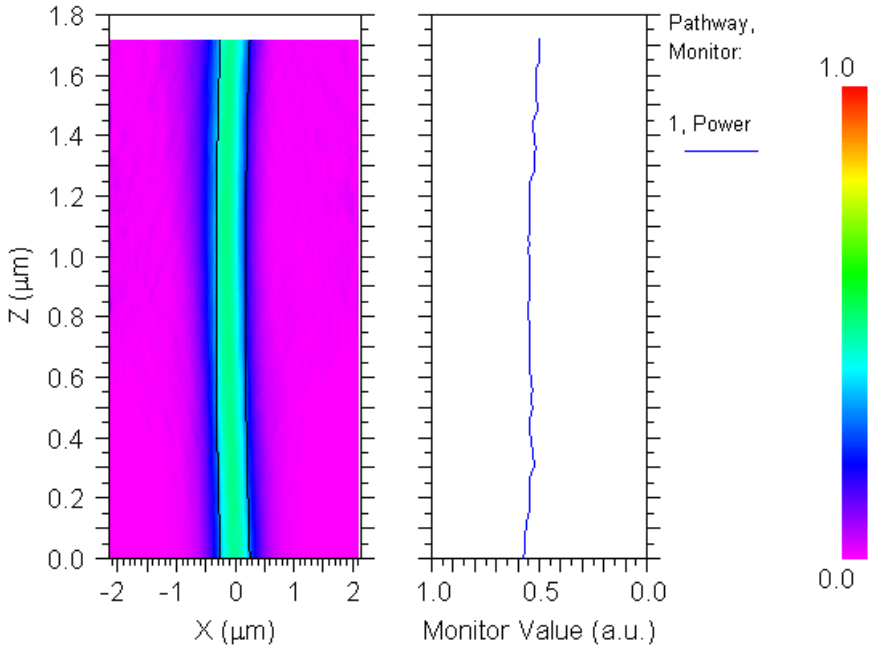

(d)

Figure 1.14: Negligible bending losses for bends with $R = 5\ \mu m$ for (a) TE-like fields in WG1, (b) TM-like fields in WG1, (c) TE-like fields in WG2 and (d) TM-like fields in WG2

Additionally, since the peak of the mode propagating through a bent waveguide segment shifts toward the outer rim, mode mismatch losses take place at transition between straight and curved waveguides as evidenced in racetrack resonators where the field is constantly traversing between straight and curved waveguides.

1.3 The basic ring resonator circuit

In its simplest form, a RR circuit consists of a straight waveguide, usually referred to as the 'bus' waveguide, adjacent to a circular 'ring resonator' waveguide as shown in Figure 1.15 .The separation gap between the two elements, the mean radius of the ring and the width of both waveguides are denoted by g_o, R and w respectively. The effective electric field components entering and leaving the interaction region are the bus input (port I) and the output (port II) fields given by a_o and b_o respectively and the corresponding fields in the ring, c_o and d_o. The light coupled evanescently from the bus to the ring cycles once around the ring before subsequently interfering at the interaction region with the newly coupled field. The interference condition depends on the geometry, mainly R, the material of the waveguides and the free space wavelength, λ_o and leads to a Lorenzian variation of the ratio of the output field to the input field with wavelength λ_o as discussed later.

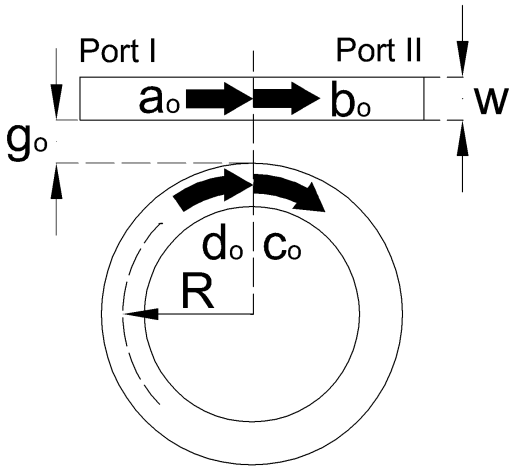

Figure 1.15: Single RR circuit.

In the "coupling of modes in space" (CMS) technique [43], the field components around the interaction region are related by:

$$b_o = r_o a_o - ik_o d_o \quad \textbf{(1.25)}$$

$$c_o = r_o d_o - ik_o a_o \quad \textbf{(1.26)}$$

in which k_o is the ratio of the field coupled between the ring and the bus, and $k_o^2 + r_o^2 = 1$. The term $-ik_o$ accounts for the $\frac{\pi}{2}$ phase shift experienced by the field at coupling transition. To avoid multimode dispersion single mode waveguides are required so that the ring field components satisfy:

$$d_o = c_o e^{-i\delta} \tag{1.27}$$

Here $\delta = \phi - i\frac{\alpha}{2}l$, is the round trip complex phase factor, $\phi = \beta l$ is the round trip phase shift, $l = 2\pi R$ is the mean circumference of the ring, $\beta = \frac{2\pi n_e}{\lambda_o}$ is the mode longitudinal propagation factor, n_e is the mode effective refractive index and α is the power loss coefficient. From the above three equations, the normalized field transmission of the device is:

$$\frac{b_o}{a_o} = \frac{r_o - \chi}{1 - r_o\chi} \tag{1.28}$$

with $\chi = e^{-i\alpha l/2}$ yielding for a normalized power transmission, T,

$$T = \left|\frac{b_o}{a_o}\right|^2 = \frac{r_o^2 - 2r_o\chi\cos(\varphi) + \chi^2}{1 - 2r_o\chi\cos(\varphi) + r_o^2\chi^2} \tag{1.29}$$

Accordingly, $T = T_{\max} = (\frac{r+\chi}{1+r\chi})^2$ when $\varphi = (2m+1)\pi$ and the ring is off-resonance, while $T = T_{\min} = (\frac{r-\chi}{1-r\chi})^2$ when $\varphi = 2m\pi$ and the ring is on-resonance, where $m = 0,1,2..$ is the mode longitudinal resonance order. Physically, after one trip around the ring, the electric field partially couples back into the bus, with a total phase shift $\varphi + \pi$ from the two coupling transitions. Thus if the ring is off-resonance, the total phase shift is an even multiple of π and the interference between the bus and the ring field is constructive. Unlike traveling wave resonators such as Fabry-Perot resonators, the RR can extract a particular wavelength completely from the input power spectrum, i.e. $T_{\min} = 0$ if the power coupled to the ring equals the round trip power loss, i.e. $r = \chi$, termed 'critical coupling' [3].

A more complex circuit is represented by Figure 1.16 , where a ring is coupled to two buses. Such a configuration has four ports: the input port I (III), the corresponding through port II (IV), and the drop ports IV (II). The field components around the bottom interaction region are similarly given by a_{oo}, b_{oo}, c_{oo} and d_{oo}. The mathematical analysis is similar to the above and yields the following coupling:

$$b_o = r_o a_o - ik_o d_o \tag{1.30}$$

$$c_o = r_o d_o - ik_o a_o \quad \textbf{(1.31)}$$

$$b_{oo} = r_{oo} a_{oo} - ik_{oo} d_{oo} \quad \textbf{(1.32)}$$

$$c_{oo} = r_{oo} d_{oo} - ik_{oo} a_{oo} \quad \textbf{(1.33)}$$

and propagation:

$$d_{oo} = c_o e^{-i\frac{\delta(2\pi-\theta)}{2\pi}} \quad \textbf{(1.34)}$$

$$d_o = c_{oo} e^{-i\frac{\delta\theta}{2\pi}} \quad \textbf{(1.35)}$$

equations, where k_{oo} is the ratio of the field coupled between the ring and the bottom bus, and $k_{oo}{}^2 + r_{oo}{}^2 = 1$

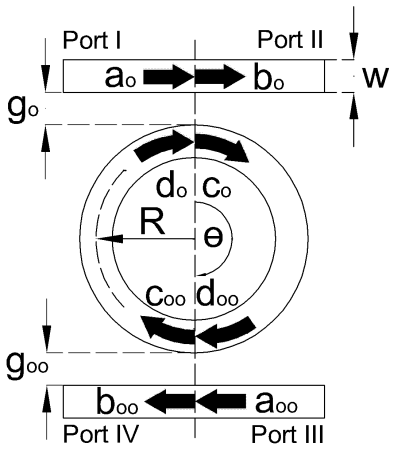

Figure 1.16: A ring resonator coupled to two buses.

We calculate the output field components b_o and b_{oo} for a single input field and then recalculate these components for the second input. The total output field from any port is then the superposition of the two sets of output fields. For $a_{oo} = 0$, we find the resulting normalized field transmission of the through and drop ports respectively given as:

$$\frac{b_o}{a_o} = \frac{r_o - r_{oo} e^{-i\delta}}{1 - r_o r_{oo} e^{-i\delta}} \quad \textbf{(1.36)}$$

$$\frac{b_{oo}}{a_o} = \frac{-k_o k_{oo} e^{-i\delta/2}}{1 - r_o r_{oo} e^{-i\delta}} \tag{1.37}$$

The ratios $\frac{b_o}{a_{oo}}$ and $\frac{b_{oo}}{a_{oo}}$ with $a_o = 0$ can then be found by replacing (k_o, r_o) by (k_{oo}, r_{oo}) in equations (1.36) and (1.37). However, complex structures with multiple rings cannot be easily obtained in this fashion and the transfer matrix method introduced below is instead typically employed.

1.4 Complex RR circuit analysis

1.4.1 Transfer matrix method

The set of equations representing the CMS technique above can be re-arranged in the form of two groups of matrices, those describing the field coupling over the interaction regions, and phase matrices describing field propagation between the coupling regions. Multiplying these matrices results in a transfer matrix that relates the fields at the input and the output of the circuit. Thus for the circuit shown in Figure 1.16 the coupling equations are:

$$\begin{bmatrix} d_o \\ c_o \end{bmatrix} = Q_o \begin{bmatrix} a_o \\ b_o \end{bmatrix} \tag{1.38}$$

$$\begin{bmatrix} d_{oo} \\ c_{oo} \end{bmatrix} = Q_{oo} \begin{bmatrix} a_{oo} \\ b_{oo} \end{bmatrix} \tag{1.39}$$

with coupling matrices $Q_o = \frac{1}{ik_o}\begin{bmatrix} r_o & -1 \\ 1 & -r_o \end{bmatrix}$ and $Q_{oo} = \frac{1}{ik_{oo}}\begin{bmatrix} r_{oo} & -1 \\ 1 & -r_{oo} \end{bmatrix}$. As well,

$$\begin{bmatrix} d_{oo} \\ c_{oo} \end{bmatrix} = P \begin{bmatrix} d_o \\ c_o \end{bmatrix} \tag{1.40}$$

with a phase matrix, $P = \begin{bmatrix} 0 & e^{-i\delta/2} \\ e^{i\delta/2} & 0 \end{bmatrix}$, Hence

$$\begin{bmatrix} a_{oo} \\ b_{oo} \end{bmatrix} = T \begin{bmatrix} a_o \\ b_o \end{bmatrix} \tag{1.41}$$

where the transfer matrix T is then $Q_{oo}PQ_o$. The boundary condition $a_{oo} = 0$, then leads to equations (1.36) and (1.37)**.** This method is especially useful for complex circuits as in Figure 1.17 and Figure 1.18 that can be employed to modify the RR transfer characteristics for e.g. WDM applications. However, while the transfer matrix procedure can be applied to any structure, for a circuit with internal feedback between the rings as in Figure 1.19, further analysis is required, c.f. Chapter 3.

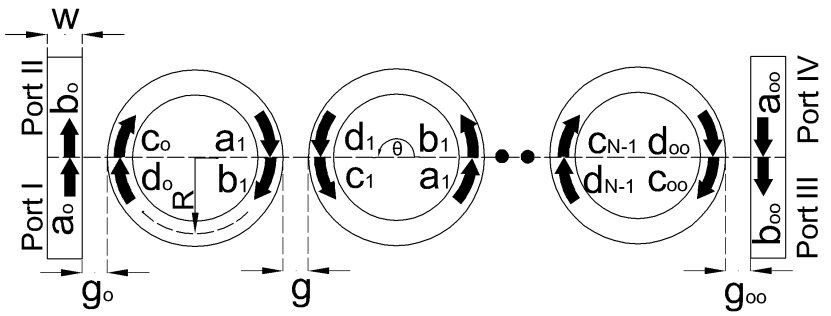

Figure 1.17: Series coupled RRs

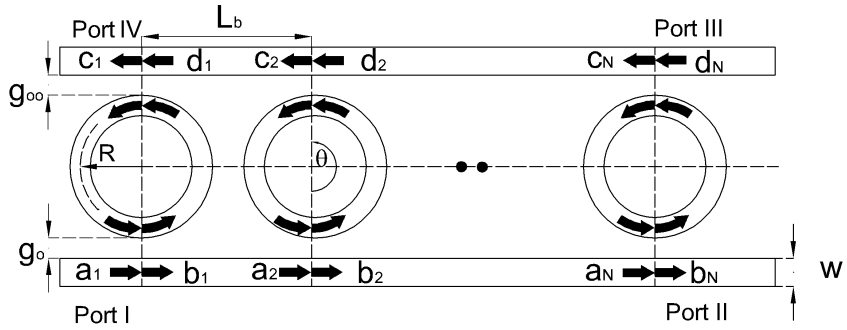

Figure 1.18: Parallel coupled RRs

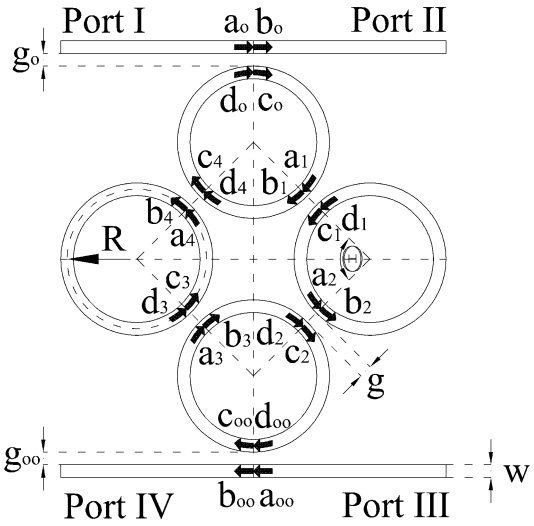

Figure 1.19: A loop of rings coupled to two buses.

1.4.2 Coupling of modes in time (CMT)

In the CMS technique, time dependence is eliminated as all fields are assumed to have harmonic dependence on time (i.e. $\sim e^{i\omega t}$). However, the same assumption can be utilized to study the circuit using a time domain approach that deals with each ring in the circuit as a lumped (i.e. dimensionless) oscillator, so that the phase variation due to field propagation around the ring is negligible w.r.t. that of the coupling transition. This technique is known as the "coupling of modes in time" (CMT) and was suggested for studying travelling wave resonators in [3].

The CMT technique possesses the advantage of simple formulation of the equations describing the problem and consequently a quicker calculation of the transfer characteristics [3]. On the other hand, and unlike the CMS, the CMT is limited to small coupling and small losses. An example exploiting the CMT is given by Figure 1.20, where a single RR is coupled to two buses. The field amplitudes of the first input, second input, through and drop fields are given by S_i, S_f, S_t and S_d respectively and are normalized so that the corresponding field powers are given by $|S_i(t)|^2$, $|S_f(t)|^2$, $|S_t(t)|^2$ and $|S_d(t)|^2$ respectively [3]. The resonant mode of the RR though is described by the energy amplitude f and total energy $|f(t)|^2$.

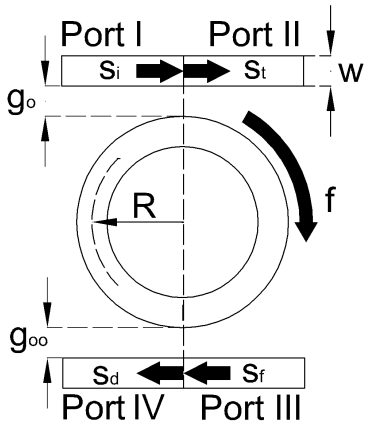

Figure 1.20: A single RR coupled to two buses.

The CMT coupling coefficients μ_o and μ_{oo} replace the CMS coupling coefficients k_o and k_{oo} respectively. Three decay rates represent the power escape from the ring, namely τ_e, τ_d and τ_l where the first two correspond to the decay into the through and the drop ports while the third is the decay due to waveguide losses. The relations between the coupling coefficients in both models are given by [3] $\mu_o = k_o\sqrt{v_g/(2\pi R)}$ and $\mu_{oo} = k_{oo}\sqrt{v_g/(2\pi R)}$ where $v_g = c/n_g$ is the group velocity and n_g the group refractive index of the RR, $\mu_o = \sqrt{2/\tau_e}$ and $\mu_{oo} = \sqrt{2/\tau_d}$ [3].

The equations for f are then:

$$\frac{df}{dt} = (i\omega_o - \frac{1}{\tau})f - i\mu_o S_i \qquad \textbf{(1.42)}$$

$$S_t = S_i - i\mu_o f \qquad \textbf{(1.43)}$$

$$S_d = S_f - i\mu_{oo} f \qquad \textbf{(1.44)}$$

Here, $\frac{1}{\tau} = \frac{1}{\tau_e} + \frac{1}{\tau_d} + \frac{1}{\tau_l}$ while ω_o is the angular resonance frequency of the RR mode. For a single input signal $a_{oo} = 0$ in the CMS model corresponding to $s_f = 0$ in CMT mode. For a harmonic time dependence $\frac{d}{dt}$ is replaced by ω and hence the through and drop normalized field transmissions are respectively:

$$\frac{S_t}{S_i} = \frac{i\Delta\omega + \frac{1}{\tau} - \mu_o^{\,2}}{i\Delta\omega + \frac{1}{\tau}} \tag{1.45}$$

$$\frac{S_d}{S_i} = \frac{-\mu_o^{\,2}}{i\Delta\omega + \frac{1}{\tau}} \tag{1.46}$$

where $\Delta\omega = \omega - \omega_o$ is the angular frequency shift from resonance yielding the power transmission

$$\left|\frac{S_t}{S_i}\right|^2 = \frac{\Delta\omega^2 + (\frac{1}{\tau} - \mu_o^{\,2})^2}{\Delta\omega^2 + \frac{1}{\tau^2}} \tag{1.47}$$

$$\left|\frac{S_d}{S_i}\right|^2 = \frac{\mu_o^{\,4}}{\Delta\omega^2 + \frac{1}{\tau^2}} \tag{1.48}$$

And hence we see that the drop transmission describes a Lorentzian function of frequency.

1.5 Conclusion

In this introduction we presented the basic principles of operation of the RR circuit. In the remainder of this thesis we analyze the tuning and tailoring of the RR Lorentzian transmission characteristics with a view to WDM applications. We also determine the device parameters, e.g. the losses and the coupling or the modal analysis using BeamPROP simulations.

In Chapter 2, we consider a hybrid structure comprising of tunable polymer over SOI and demonstrate the application of this structure to high speed switches. In Chapter 3, we design a closed series of ring resonators and discuss its possible application as a WDM multiplexer. We apply both the CMS and CMT analysis techniques and show how the CMT gives quick and accurate results, under the limitation of small coupling and losses. We also exploit the finite difference time domain (FDTD) simulations to analyze the same circuit and contrast the results to those of the CMS and CMT. As well, we present fabrication and test results for this circuit. Finally, we discuss the application of our structure to rotational motion detectors and compare the structure to fiber optic gyroscopes in Chapter 4. We finally conclude and discuss the future work in Chapter 5.

Chapter 2

Tunable hybrid ring resonators

Tunable ring resonators based on different tuning techniques such as thermal tuning [44], plasma injection tuning [45-47] and electro-optic polymer tuning [11-12] has previously been introduced. While the speed of thermal tuning is limited to milliseconds [44], plasma injection exhibits a tuning speed up to $5\,GHz$, and can be easily implemented in SOI by surrounding the optical waveguide core by a p-doped and n-doped regions [45]. Electrons and holes flow through the resulting p-i-n junction, under an externally applied forward tuning voltage, to alter the effective RI of the field encounters. However, the injected carriers occupy the same region as the propagating light, resulting in undesirable absorption losses. Consequently, the power transmission quality factor at the resonance frequencies becomes dependent on the tuning voltage.

In contrast, electro-optic polymers enable tunable ring resonators with very high tuning speeds of up to $100\,GHz$ [11]. However, the small refractive index (RI) contrast between the waveguide core and cladding requires that the ring radius be large to decrease the bending losses at the expense of the footprint and the free spectral range of transmission. However, extending design concepts that were recently applied to a hybrid polymer-SOI Bragg reflector [48] and a polymer-compound semiconductor directional coupler [49], we here propose a novel tunable RR device that leverages the advantages of both polymers and semiconductors.

2.1 Hybrid structure design

2.1.1 Operation and dimensions

A simple RR circuit consists of one ring coupled to a bus waveguide is shown in Figure 2.1, where the field components around the coupling region are denoted by a_o, b_o, c_o and d_o while the ring mean radius, the bus width and the ring-bus coupling gap are denoted by R, w and g_o respectively. The central free space wavelength in this work is taken to be $\lambda_o = 1.55\ \mu m$.

The ring and the bus are taken to possess the same waveguide structure for which a polymer layer covers the top side of a conventional silicon core–silica clad waveguide as shown in Figure 2.2. When an external tuning voltage (V), is applied, the electro-optically induced RI variation in the polymer layer alters the effective RI, n_e, of the waveguide mode and hence the transmission characteristics of the RR. The tuning voltage is applied across two electrodes. The first electrode is a gold layer with thickness $t_4 = 0.1\,\mu m$ [11] that resides on top of the polymer layer, which has a complex refractive index $n_4 = 0.55 - 11.5i$ [50], where i is the imaginary unit representing the absorption loss in that layer. The second electrode is buried under the buried oxide layer and is composed of a doped silicon layer, with a RI $n_5 \approx n_1 = 3.474$ and thickness $t_5 = 0.2\ \mu m$.

Here, t_3 is chosen small enough to suppress the power overlap with the doped silicon layer, decreasing the power leakage, and also to effectively eliminate the potential drop over the electrode.

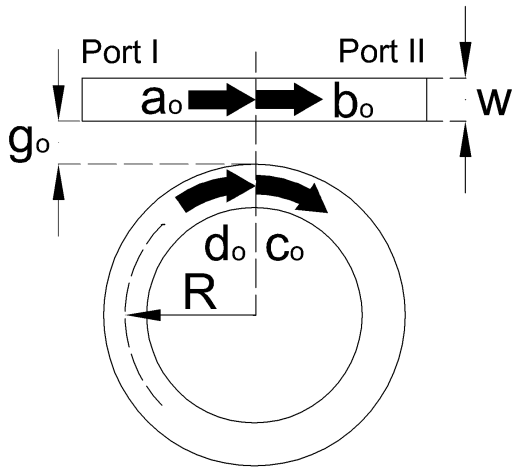

Figure 2.1: A simple single ring resonator circuit.

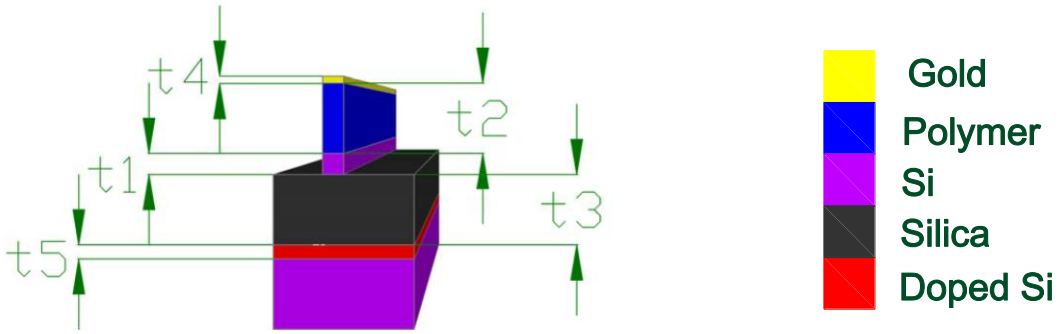

Figure 2.2: A vertical cross section of the waveguide structure. The color mark to the right defines the layer material.

The waveguide core should satisfy three conditions. First, it should operate in a single mode to avoid multimode dispersion effects. Second, the propagation loss should be minimized to ensure a high quality factor, Q. Finally, the device dimensions should be small in order to minimize the tuning voltage V and the footprint, as discussed below. Assuming a constant temperature and neglecting stresses as in [48-49], it is found that all these conditions are satisfied for a Si-core waveguide surrounded by silica with $w = t_1 = 0.3\,\mu m$ and a silica layer thickness $t_3 = 1\,\mu m$ as in [29]. The power propagation loss coefficient due to sidewall scattering and substrate leakage is $\alpha = 6\,dB/cm \rightarrow 1.4\times10^{-4}/\mu m$ as found experimentally [30] and theoretically [29]. The difference between the present structure and that of [29] is the replacement of silica with polymer on one side of the core. The polymer coating has a thickness t_2 and is formed from CLD1/APC (cross linked degree 1/amorphous polycarbonate) as in [12]. The polymer refractive index n_2, is a function of V where $n_2 = n_p = 1.612$ when $V = 0$, and $n_2 = n_p + \Delta n_2$ when $V > 0$. To satisfy these conditions, we can adjust four parameters. The first two are, t_2 and the field polarization, which determine the values of

both the absorption loss due to the gold layer and V. The third is R which determines the bending losses and finally the ring-bus gap, g_o, that controls the ring-bus coupling along with R. The last two parameters are application dependent as will be shown below.

2.1.2 Polymer thickness

We now determine t_2 according to a tradeoff between V and the absorption loss in the gold layer. Since the electric field is continuous:

$$\varepsilon_1 E_1 = \varepsilon_2 E_2 = \varepsilon_3 E_3 \qquad \textbf{(2.1)}$$

where E_j is the externally applied electric field component through the permittivity (ε_j) layer. Neglecting fringing effects and the potential drop on the electrodes we have

$$V = t_1 E_1 + t_2 E_2 + t_3 E_3 = [t_2 + t_1 \frac{\varepsilon_2}{\varepsilon_1} + t_3 \frac{\varepsilon_2}{\varepsilon_3}] E_2 \qquad \textbf{(2.2)}$$

The variation in the polymer RI, Δn_2, due to E_2 is given by [13]:

$$\Delta n_2 = -\frac{1}{2} n_p^3 r_{33} E_2 \qquad \textbf{(2.3)}$$

in which r_{33} is the polymer EO-coefficient. Assuming that $\Delta n_2 << n_p$, we approximate

$$n_2 = n_p + \Delta n_2 \approx n_p \qquad \textbf{(2.4.a)}$$

or equivalently

$$\varepsilon_2 \approx \varepsilon_p \qquad \textbf{(2.4.b)}$$

This yields

$$V \approx -[\frac{2\Delta n_2}{r_{33} n_2^3}][t_2 + t_1 \frac{\varepsilon_2}{\varepsilon_1} + t_3 \frac{\varepsilon_2}{\varepsilon_3}] \qquad \textbf{(2.5)}$$

The cutoff frequency of such circuits can reach $20-100\,GHz$ [12], [51] for which $\varepsilon_3 = 1.956^2 \varepsilon_o$ and $\varepsilon_1 = 3.41775^2 \varepsilon_o$ [52] where ε_o is the air permittivity. Polymers exhibit a small variation in the RI with frequency [53-54] which implies that the value of $n_2 = 1.612$ in the optical range can be used as is in the microwave frequency range ($20-100\,GHz$), and hence we can use $\varepsilon_2 = 1.612^2 \varepsilon_o$. Thus, from equation (2.5) to minimize V, t_2 must be reduced. On the other hand, for smaller t_2 values, the field overlaps more with the gold electrode augmenting the absorption loss. We therefore employ the semi-vectorial beam propagation method (BPM) [22-28], [55] to compute

the variation of the losses in the gold layer with t_2 for both the TE and TM modes where we employ the complex refractive index value of the gold layer, $0.55-11.5i$ [50]. The absorption loss in dB/cm due to the gold layer is then plotted versus t_2 in

Figure 2.3, from which it is obvious that the absorption loss of the TM mode is greater than that of the TE mode for the same polymer thickness t_2. This is expected since the TM mode is more weakly confined in the direction normal to the substrate and therefore overlaps more with the polymer and gold layers. Therefore, in order to eliminate the gold absorption, t_2 should be greater than $1\,\mu m$ for the TM-like and greater than $0.8\,\mu m$ for the TE-like mode.

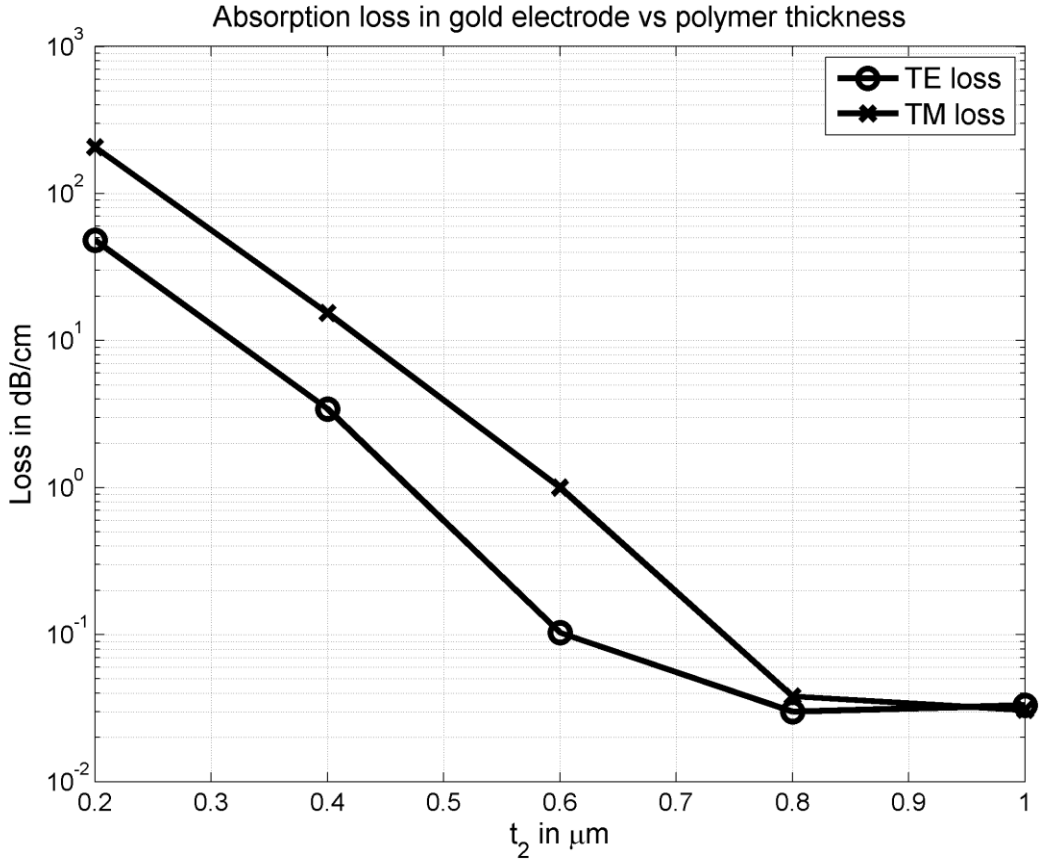

Figure 2.3: The absorption loss induced by the gold layer as a function of polymer thickness. The inset shows the losses for $t_2 > 0.8\,\mu m$

Finally, to determine which polarization and t_2 value to select, we examine the sensitivity of n_e to variations in n_2. Here we take $t_2 = 0.8\mu m$ for the TE-like mode and $t_2 = 1\mu m$ for the TM-like mode as just discussed. Again, we employ the semi-vectorial BPM to calculate $n_e(\lambda_o)$ for different values of n_2 yielding the results of Figure 2.4. We first observe that both polarizations are nearly

equally affected by the wavelength variation as $\frac{\partial n_e}{\partial \lambda_o} = -1.26/\mu m$ for the TE-like mode and $\frac{\partial n_e}{\partial \lambda_o} = -1.3/\mu m$ for the TM-like mode at constant V. Secondly, the response of the TM-like mode to the polymer RI variation ($\frac{\partial n_e}{\partial n_2} = 0.28$) is nearly one order of magnitude larger than that of the TE-like mode ($\frac{\partial n_e}{\partial n_2} = 0.025$) at constant wavelength. This again can be explained by the increased overlap of the TM mode with the polymer. Therefore, we do not consider the TE mode in this chapter. The corresponding layer refractive indices and thicknesses are summarized in Table 2.1 and Table 2.2 respectively where we employ WG1 characteristics in Table 1.1 .

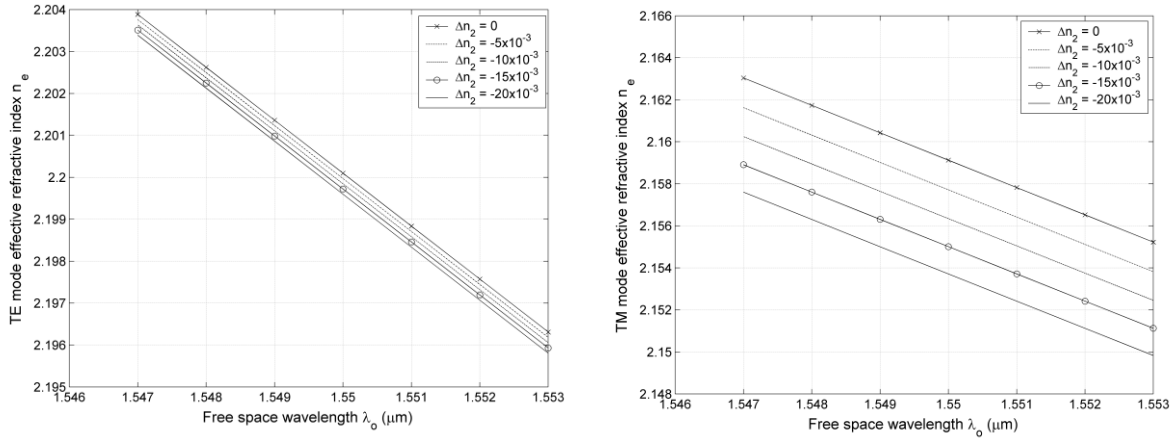

a b

Figure 2.4: Mode refractive index (n_e) as a function of the free space wavelength (λ_o) for different polymer RI (n_2) values. (a) TE mode with $t_2 = 0.8\,\mu m$ (b) TM mode with $t_2 = 1\,\mu m$

n_1	n_2	n_3	n_4	n_5	n_6
3.474[29]	$= n_p = 1.612$ [29]	1.444 [29]	$0.55 - 11.5i$ [50]	$\approx n_1$	$= n_3$

Table 2.1: Waveguide refractive indices.

t_1	t_2	t_3	t_4	t_5	w
$0.3\mu m$ [29]	$1\,\mu m$	$1\,\mu m$ [21]	$0.1\,\mu m$ [11]	$0.2\,\mu m$	$0.3\,\mu m$ [29]

Table 2.2: Waveguide cross section dimensions.

At this point we have deduced the parameters of the structure except the mean radius of the ring (R) and the ring-bus gap (g_o), which are determined according to the desired device operation. In the following sections we tune the transmission characteristics of the hybrid structure by altering the ring resonance or the ring-bus coupling.

2.2 Hybrid structure application

The device transmission characteristics of an electro-optic device are tuned through the dependence of n_e on V. Here we assume that $R >> w$ and that the modes in the bus and the ring have identical values of n_e as discussed in Chapter 1. If both the ring and the bus experience the same V, the induced refractive index change Δn_e is normally identical in both waveguides preventing phase-mismatch. This way, the resonance condition of the ring can be altered. Another way is to apply V to the bus only so that the phase mismatch alters the coupling with the ring while the ring resonance is maintained. Either way, the transmission characteristics of the device become tunable.

2.2.1 Power transmission tuning

2.2.1.1 Design

The power transmission coefficient for the circuit in Figure 2.1 is defined as the ratio of the output power to the input power, namely [56]:

$$T = \frac{r^2 - 2r\chi\cos(\phi) + \chi^2}{1 - 2r\chi\cos(\phi) + (r\chi)^2} \tag{2.6}$$

while the quality factor is [5756]:

$$Q = \frac{2\pi^2 R n_e \sqrt{r\chi}}{(1 - r\chi)\lambda_o} = \frac{\lambda_o}{\delta\lambda_o} \tag{2.7}$$

Here, $r = \sqrt{1-k^2}$, k is the field coupling ratio defined as the ratio of the electric field coupled between the ring and the bus, $\chi = \exp(-\frac{\alpha l}{2})$ is the field loss coefficient, $l = 2\pi R$ is the ring mean circumference, ϕ is the round trip phase shift that can be expressed as $\varphi = \frac{2\pi}{\lambda_o} n_e l$ and $\delta\lambda_o$ is the 3 dB-bandwidth (B.W.). The transmission coefficient is a maximum for the off-resonance state with

$T_{\max} = (\frac{r+\chi}{1+r\chi})^2$ and a minimum at the on-resonance state with $T_{\min} = (\frac{r-\chi}{1-r\chi})^2$. The extinction ratio, ζ, can be defined as $\zeta = \frac{T_{\max}}{T_{\min}}$ [57] and is maximized when the critical coupling condition, $r = \chi$, is fulfilled [57]. The wavelength difference, $\Delta\lambda_o$, between two successive transmission maxima is called the free spectral range, FSR and is given by [12], [59]:

$$FSR = \Delta\lambda_o = \frac{\lambda_o^{\ 2}}{2\pi R n_g} \tag{2.8}$$

where $n_g = n_e - \frac{dn_e}{d\lambda_o}\lambda_o$ is the group refractive index [59]. The shift in the transmission characteristics due to V, is called the tuning range, TR. For maximum tuning of the ring transmission characteristics, R, is chosen to provide full tuning between on-resonance and off resonance states, so that $TR = \frac{1}{2}FSR$. Consequently, R should satisfy the conditions

$$2\pi R\frac{n_e}{\lambda_o} = m \tag{2.9.a}$$

for on-resonance operation at a specified wavelength λ_o and

$$2\pi R\frac{n_e + \Delta n_e}{\lambda_o} = (m - 0.5) \tag{2.9.b}$$

for off-resonance operation at the same wavelength, where m is integer. We can subtract equation (2.9.a) from (2.9.b) to find that the ring radius should satisfy the following condition:

$$R = R_{oo} = \frac{\lambda_o}{4\pi|\Delta n_e|} \tag{2.10}$$

for complete switching from on-resonance to off-resonance at the same wavelength. Equations (2.5) and (2.10) represent the primary tradeoff between V and R_{oo} since increasing the value of V increases both $|\Delta n_2|$ and $|\Delta n_e|$, while reducing R_{oo}. For a polymer with $r_{33} = 1000\ pm/V$ which is expected to be shortly available [60], we find the results for $\Delta n_2(V)$ and $\Delta n_e(V)$ displayed in Figure 2.5.a while the corresponding $R(V)$ is shown in Figure 2.5.b. The range of V for high speed switching applications is assumed to lie in the range of $1-10 Volt$ and the corresponding radii are computed to be $49.6 - 495.6\ \mu m$. The product VR, where $R = R_{oo}$, remains nearly equal to $496 Volt.\mu m$ over

this range of V, as could be predicted from the nearly linear dependence of n_e on n_2 in Figure 2.4.a and Figure 2.5.a.

The BPM has also been employed to calculate the bending losses for this range of R following the technique in [19] where the calculated mode is launched into an arc of the ring with a 20^o central angle and the power is monitored. Then the bending loss is scaled to 90^o to find the loss after a quarter trip. Simulations show that the bending loss is very small compared to the scattering loss so that α remains at the scattering loss value of $6\,dB/cm$.

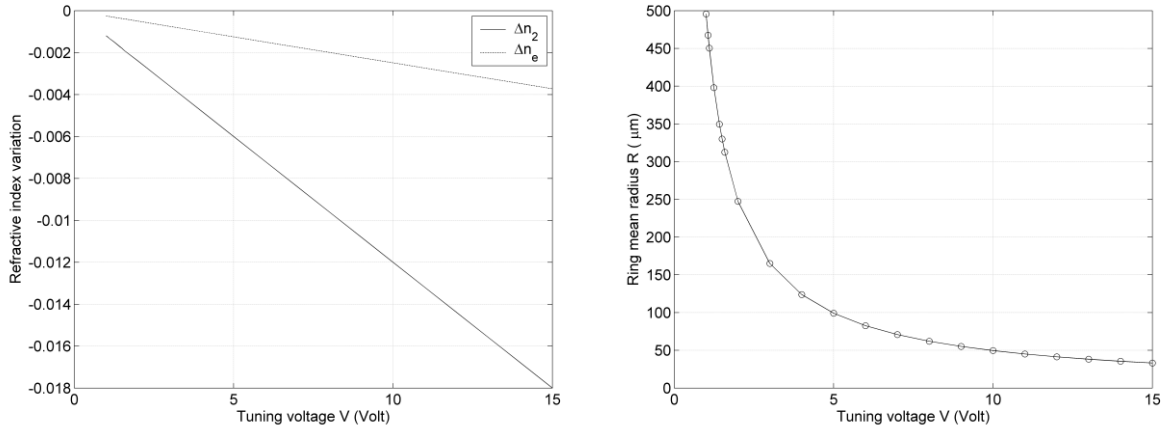

a b

Figure 2.5: (a) Variation of n_2 and n_e with V (b) the dependence of the $R = R_{oo}$ required on V for full ON-OFF switching.

The last parameter to study is the ring-bus separation g_o which is employed to control the field coupling ratio k. Again we apply our BPM program to calculate $k(R, g_o)$. We follow the method of [19] in which the calculated mode is launched into the bus which is next to an arc of the ring with 20^o central angle. The power in the bus is then monitored and the output power of the bus is identified with r^2. The results for $R = R_{oo}$ values for which g_o varies from $0.2\,\mu m$ to $0.6\,\mu m$ in steps of $0.1\mu m$ are shown in Figure 2.6 where χ is also plotted to demonstrate when the critical coupling condition can be fulfilled. For instance, two points are marked on Figure 2.6 that yield a maximum transmission extinction ratio since the critical coupling condition is fulfilled. At the 'First design point', we find, $R = 49.6\,\mu m$, $V = 10 Volt$, $g_o = 0.4\,\mu m$, $n_e = 2.159683$, $\Delta n_2 = -0.012$, $\Delta n_e = -0.0025$, $\chi = 0.978$ and $r = 0.982$ implying that R is minimized while V is large. For the second point, $R = 312.4\,\mu m$, $V = 1.6 Volt$, $g_o = 0.2\,\mu m$, $n_e = 2.161774$, $\Delta n_2 = -0.0019$, $\Delta n_e = -0.0004$, $\chi = 0.87$ and $r = 0.89$. The device response in both cases is studied in the next section. The normalized transmission for the device is shown in Figure 2.7.a and Figure 2.7.b for the first and second design points respectively. The first design has the following transmission

characteristics. $FSR = 2TR = 1.85\,nm$, $\varepsilon_e = 20\,dB$, $Q = 3.4\times10^4$, $\delta\lambda_o = 45.9\,pm$ while for the second design we have, $FSR = 2TR = 0.29\,nm$, $\varepsilon_e = 21\,dB$, $Q = 3.35\times10^4$, $\delta\lambda_o = 46.2\,pm$.

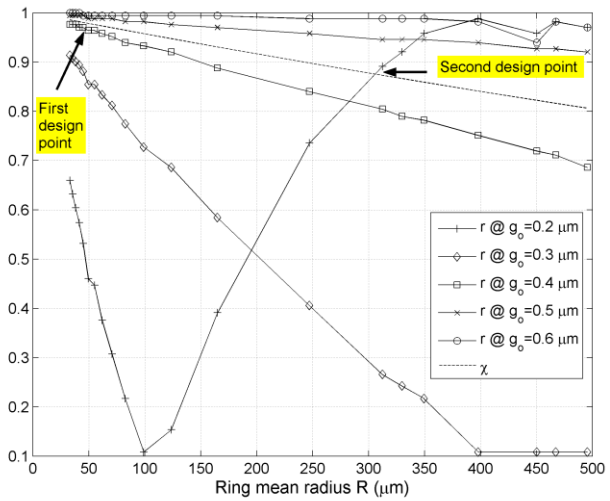

Figure 2.6. The variation of the field transfer coefficient r and the field loss coefficient χ with mean ring radius $R = R_{oo}$ and the ring-bus gap g_o

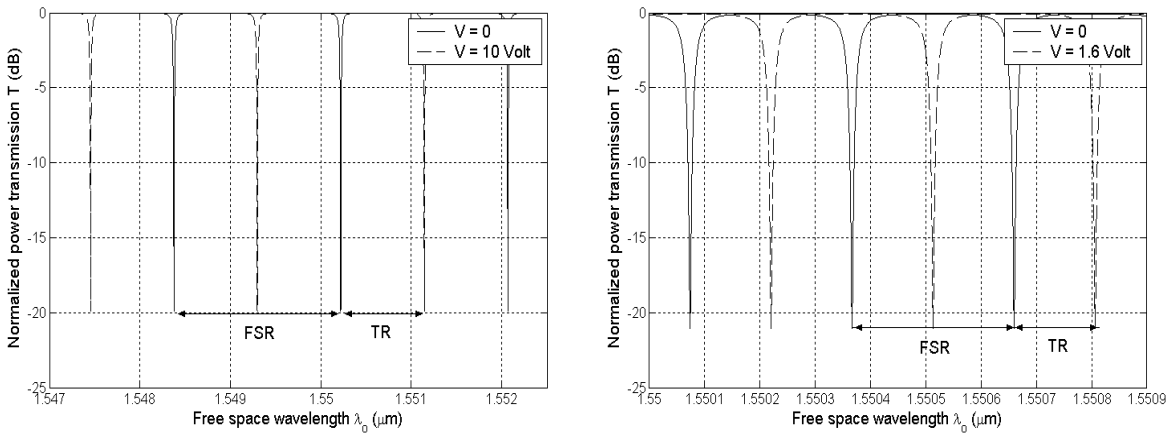

(a) (b)

Figure 2.7: The device normalized power transmission (a) first design point, (b) second design point

While the quality factor is high for both designs, the large ratio of the FSR in the two designs is the result of the large ratio of the two design radii.

2.2.1.2 Comparison with similar circuits

Table 2.3 compares the characteristics of the two designs for the proposed hybrid device to two other tunable RR circuits that were tested experimentally. The first of these employs Si/SiO_2 technology with plasma injection tuning [45] and the second is a pure polymer structure [12] that is tuned through the polymer EO coefficient (note that the circuit in [12] employs different waveguides for input and output). The features that are the same in our design and the two other designs are shaded. As we see, our design is compatible with silicon technology, exhibits a small waveguide cross section dimensions compared to polymer waveguides [12], and displays a high silicon/silica RI contrast and hence larger FSR and TR. The tuning in [45] depends on carrier injection into the waveguide core which shifts the transmission characteristics through a change in n_e. Then, the tuning speed of this device is limited by the carrier lifetime and further requires a bipolar V to efficiently inject and extract carriers from the waveguide. As well, the transmission quality then depends on the tuning. To achieve larger shifts more electrons must be injected, decreasing the quality factor. On the other hand, for the hybrid structure, the tuning depends on the electro-optic effect in polymers which is far faster, can be achieved with a single polarity V, and displays a quality factor that is nearly independent of the tuning voltage. The main fabrication difficulty is the doped silicon layer beneath the silica layer. One of the available alternatives is through fabricating the device in hydrogenated amorphous silicon with low absorption loss [61-62] since amorphous silicon can be grown over silica. A second possibility is using implantation of oxygen ions and subsequently annealing as in [63]. Finally, the substrate can be doped before the layer transfer step in the 'Smart-cut' process to fabricate silicon over oxide SOI [64].

	Si/SiO_2 [45]	First design (second design)	Full polymer [12]
$\lambda_{resonance}(\mu m)$	1.55	1.55	1.3
Waveguide cross section dimensions.	$0.45\,\mu m \times 0.25\,\mu m$	$0.3\,\mu m \times 0.3\,\mu m$	$5\,\mu m \times 1\,\mu m$
$R(\mu m)$	6	49.6 (312.4)	750
$V(Volt)$	V_{pp} = 3 {Different polarities for carrier injection and extraction}	10 (1.6) {Single polarity}	4.85 {Single polarity}
$TR(nm)$	0.05	0.925 (0.15)	0.023
$Q \times 10^4$	3.935	3.4 (3.35)	6.2
$\varepsilon\,(dB)$	15	20 (21)	Not given
Modulation frequency.	5 GHz	Up to $20-100\,GHz$	Up to $20-100\,GHz$ [12], [48], [65]
Transmission Characteristics	More carrier injection increases the losses and alters the transmission characteristics.	Does not depend on tuning.	Does not depend on tuning.
Difficult to fabricate.	Standard Silicon Technology. Requires many fabrication steps for p-i-n junction and electrode formation.	Silicon Technology with two extra steps for the polymer layer and buried doped silicon layer.	Many steps for different polymer layer treatment.
Compatibility with Silicon Technology.	Compatible.	Compatible.	Requires special treatment [65-66].

Table 2.3: Comparison of four tunable ring resonator circuits where our 'second design' parameters are shown between brackets.

2.2.2 Ring-bus coupling variation

In the next proposed circuit design, the tuning voltage is applied only to the bus electrodes inducing a phase mismatch between the bus and ring modes that alters the coupling and consequently the transmission characteristics. To simplify the coupling calculations, we investigate the racetrack-bus configuration in Figure 2.8 in place of a RR system. The racetrack-bus coupling is then approximated by the coupling between two parallel bus waveguides, neglecting the coupling in the bent regions.

2.2.2.1 Principle of operation

We first slightly modify several circuit parameters. All the parameters defined previously in this chapter are still present but ring parameters are replaced by racetrack parameters. Therefore, l is given by,

$$l = 2\pi R + 2L \tag{2.11}$$

with L is the length of the racetrack side representing the interaction length between the two straight waveguides (SWGs). Further, ϕ denotes the racetrack round trip phase shift, and for simplicity we eliminate the dependence on ϕ by designing the device such that the resonance condition:

$$\phi = 2m\pi \tag{2.12}$$

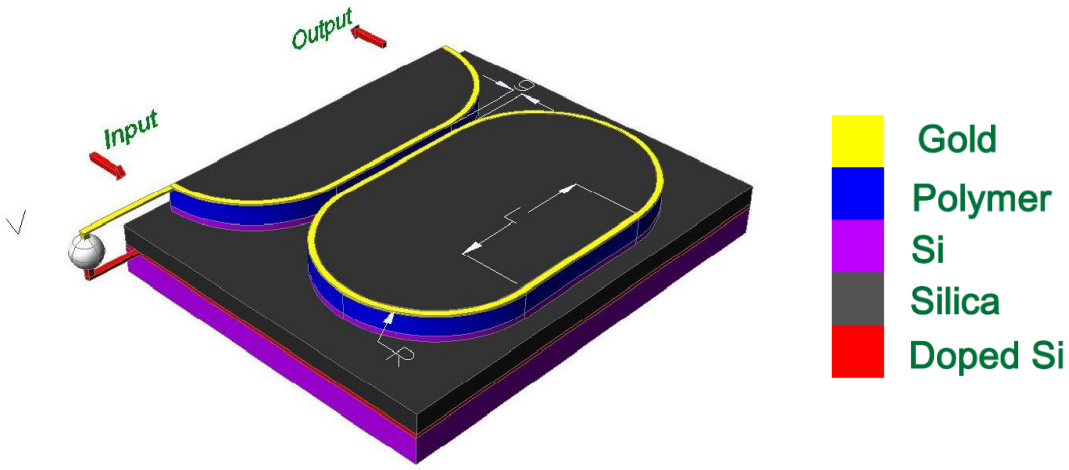

Figure 2.8: Racetrack-bus configuration. The silica layer surrounding the silicon core is not shown.

Is fulfilled, where m is integer. The maximum T is $T_{\max} = 1$, which occurs for zero power coupling, $r = 1$, while the minimum $T_{\min} = 0$ is obtained at $r = \chi$, as previously mentioned. From the variation of T with k presented in Figure 2.9, we conclude that small variation in k can shift T from a maximum to minimum, especially for low loss circuits with $\chi \approx 1$. Also, for $V = 0$ we find $n_{e1} = 2.16051$ at $\lambda_o = 1.55\ \mu m$.

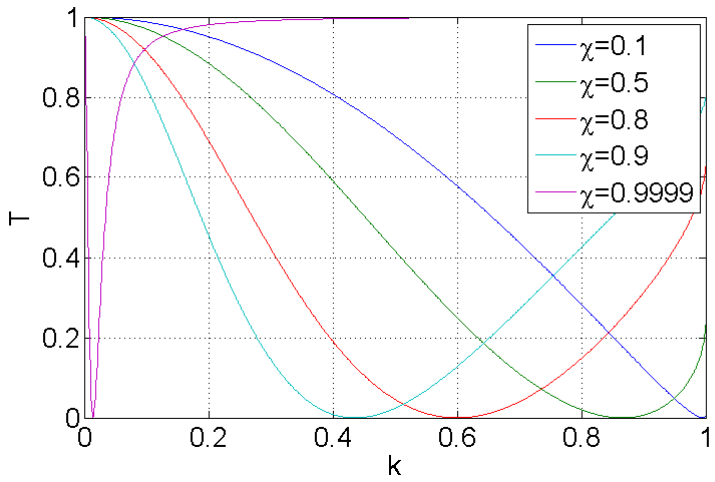

Figure 2.9: Variation of the power transmission factor (T) on resonance with the field coupling ratio (k) for different round-trip losses

As discussed in Chapter 1, for two parallel SWGs, k is given by [38]:

$$k = \sin\left(\int_{-L/2}^{L/2} \kappa e^{-j\Delta\beta z} dz\right) \tag{2.13}$$

in which κ represents the coupling coefficient between two parallel SWGs, $\Delta\beta_d = \frac{2\pi}{\lambda_o}\Delta n_d$ is the phase mismatch and $\Delta n_d = n_{e1} - n_{e2}$ is the difference in the effective RI between the coupled waveguides when power is coupled from waveguide (2), which is the bus, into waveguide (1), which is the racetrack side and z is the direction of propagation. From equation (2.13) we find:

$$k = \sin\left(\frac{\kappa L \sin(X)}{X}\right) \tag{2.14}$$

with

$$X = \Delta\beta_d L/2 = \frac{\pi \Delta n_d L}{\lambda_o} \tag{2.15}$$

We label X the 'tuning term', since it quantifies the degree to which k or equivalently the normalized power transmission (T) has been adjusted. Since $\sin(X)/X$ is an even function of X, these quantities are dependent on the absolute value of Δn_d. For $\Delta\beta_d = 0$, equation (1.20) reduces to the well known relation:

$$k = \sin(\kappa L) \tag{2.16}$$

Accordingly, for $T = T_{\max} = 1$, L should insure that with no phase mismatch, i.e. $\Delta\beta_d = 0$, the coupling vanishes corresponding to $r = 1$ and $k = 0$. From (2.16) , this yields

$$L = n\pi / \kappa \tag{2.17}$$

for integer $n = 1,2,\ldots$ (Note that $n = 0$ is unphysical since $L \neq 0$). However, $T = T_{\max} = 1$ as we will demonstrate below, is difficult to achieve and hence this condition is only applied to obtain an initial estimate of L which is then optimized. For an applied tuning voltage, V , the phase mismatch, $\Delta\beta_d$, should satisfy $T = T_{\min} = 0$. This yields the condition:

$$\left|\sin(\kappa L \frac{\sin(X)}{X})\right| = \sqrt{1-\chi^2} \tag{2.18}$$

which is our central equation. In the next section we design a device that realizes this condition.

2.2.2.2 Device design

To solve equation ((2.18), we first write the left and right hand sides of the equation as:

$$L.H.S = W(\kappa, L, \Delta n_e) = \sin(\kappa L \frac{\sin(X)}{X}) = \sin(\kappa L \frac{\sin(\pi \Delta n_d L / \lambda_o)}{\pi \Delta n_d L / \lambda_o}) \tag{2.19}$$

$$R.H.S = Z(m) = \sqrt{1-\chi^2} = \sqrt{1 - \exp(-\frac{m\lambda_o}{n_{e1}}\alpha)} \tag{2.20}$$

where Δn_d and m are independent variables and $Z(m)$ is a discrete function of m . *The objective now is to determine the dimensions* L *and* R . We can then employ a mode solver to find the value of Δn_2 corresponding to Δn_d , along with equation (2.5) in order to obtain V, while R can be calculated from m by employing equations (2.11) and (2.12). We select $|\Delta n_d| \prec 2 \times 10^{-3}$ to give $V < 8.3 Volt$, insuring a high switching speed, and $m \leq 1000$ to limit the value of R .

Next, employing equation (2.17) , we maximize the coupling coefficient, in order to minimize the racetrack dimensions, by setting $g = 0.2\ \mu m$ which yields a coupling length $\Lambda = 9.75\ \mu m$ and $\kappa = \frac{\pi}{2\Lambda} = 0.1611/\mu m$. Figure 2.10 displays W and Z for $L = \frac{n\pi}{\kappa}$ and $n = 1$ to $n = 8$.

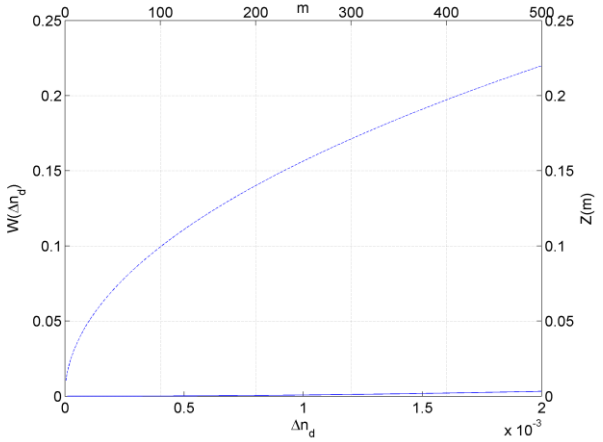
m
W(Δn_d)
Z(m)
Δn_d
x 10^-3

(a)

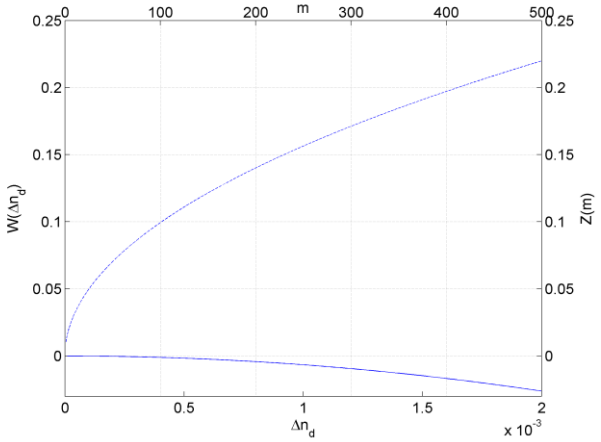
m
W(Δn_d)
Z(m)
Δn_d
x 10^-3

(b)

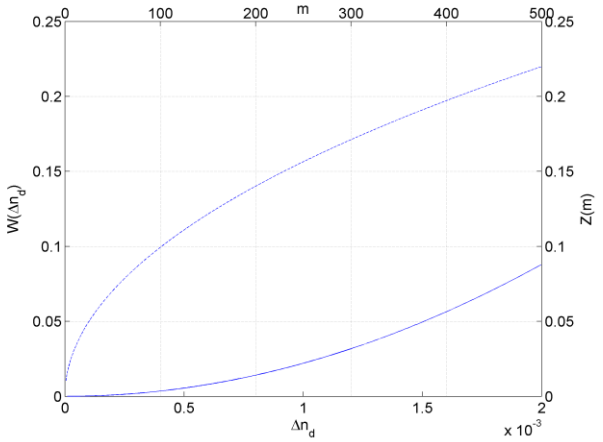
m
W(Δn_d)
Z(m)
Δn_d
x 10^-3

(c)

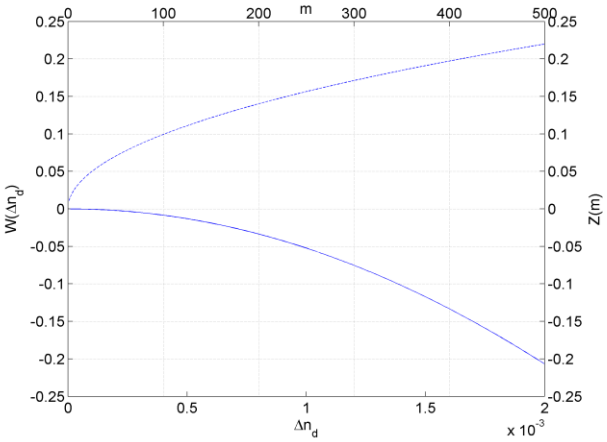
m
W(Δn_d)
Z(m)
Δn_d
x 10^-3

(d)

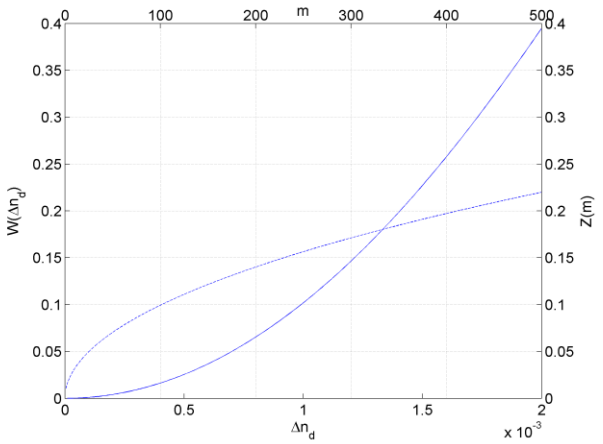
m
W(Δn_d)
Z(m)
Δn_d
x 10^-3

(e)

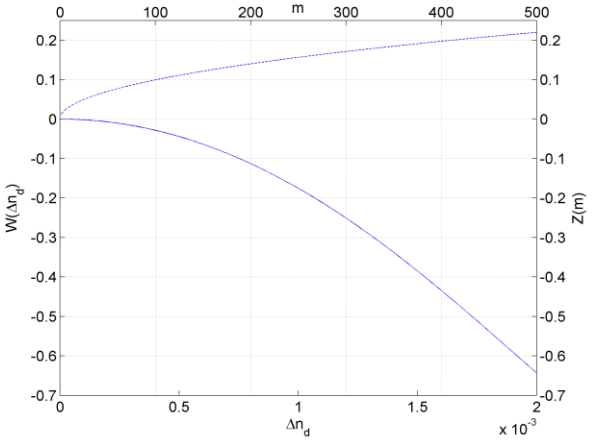
m
W(Δn_d)
Z(m)
Δn_d
x 10^-3

(f)

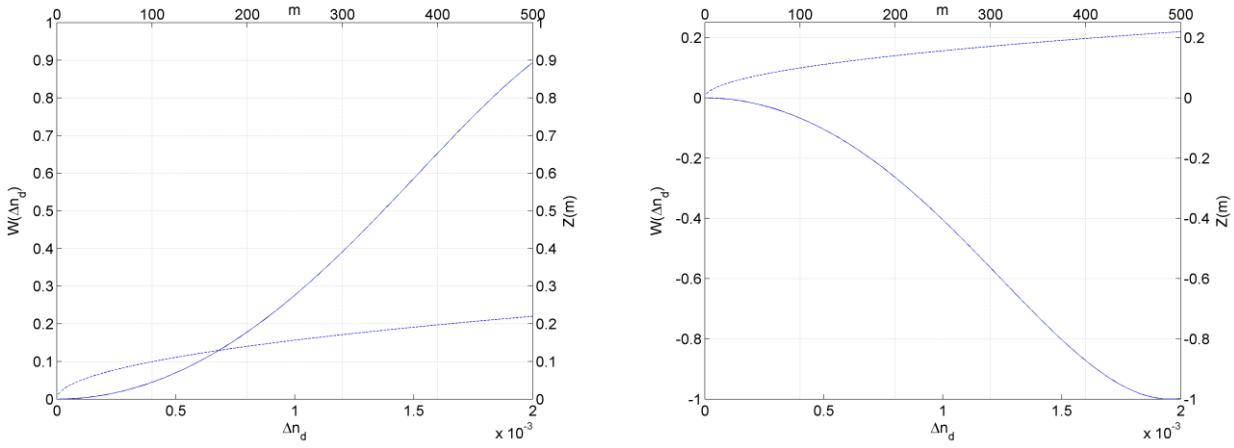

(g) (h)

Figure 2.10. $W(\Delta n_e)$ **(solid line) and** $Z(m)$ **(dashed line) for** $L = n\pi/\kappa$**, (a)** $n=1$**, (b)** $n=2$**, (c)** $n=3$**, (d)** $n=4$**, (e)** $n=5$**, (f)** $n=6$**, (g)** $n=7$**, (h)** $n=8$

For typical values $r = \cos(n\pi \frac{\sin(X)}{X})$ is negative with odd n. While many solutions of equation (2.18) exist, for these solutions equation (2.6) implies that $T_{\min} \approx T_{\max}$ so that the extinction ratio $\zeta = 10\log(\frac{T_{\max}}{T_{\min}}) \approx 0$. For even n, however, W and consequently k are equal or slightly smaller than 0 while $r \approx +1$, so that no solutions to equation (2.18) exist. Therefore, we relax the condition of equation (2.17) by permitting $T_{\max} < 1$, but we still employ this equation to estimate the value for L at which we begin a search for the exact solution. We also set a condition, $|L.H.S - R.H.S| \le 10^{-6}$, that defines the acceptable values for L. For the first solution we therefore start with an L value close to $2\pi/\kappa = 39\ \mu m$, and subsequently obtain $L = 40.05\ \mu m$. Figure 2.11.a then shows there exists possible solutions to equation (2.18), in the range $201 \le m \le 290$, while Table 2.4 identifies the corresponding circuit. Here we have employed $r_{33} = 1000\ pm/Volt$ which should be achievable in the near future [60]. We find the second relevant value for L in the vicinity of $4\pi/\kappa = 78\ \mu m$, which yields $L = 80\ \mu m$. Again, Figure 2.11.b and Table 2.5 show the corresponding solutions and circuit parameters in the range $97 \le m \le 1000$.

Both tables indicate a trade-off among V and (R and $T_{\max}$) since racetracks with smaller radii exhibit a smaller optical loss and consequently a larger $T_{\max}$, given that the bending losses are negligible. The optimum design is therefore given by the ninth entry of Table 2.5, shown in bold, since the last two entries have $R < 0$ and are therefore unphysical. As well, for typical SOI waveguides, the bending losses can be neglected for $R > 5\ \mu m$ [32], and we therefore neglect solutions that violate this assumption.

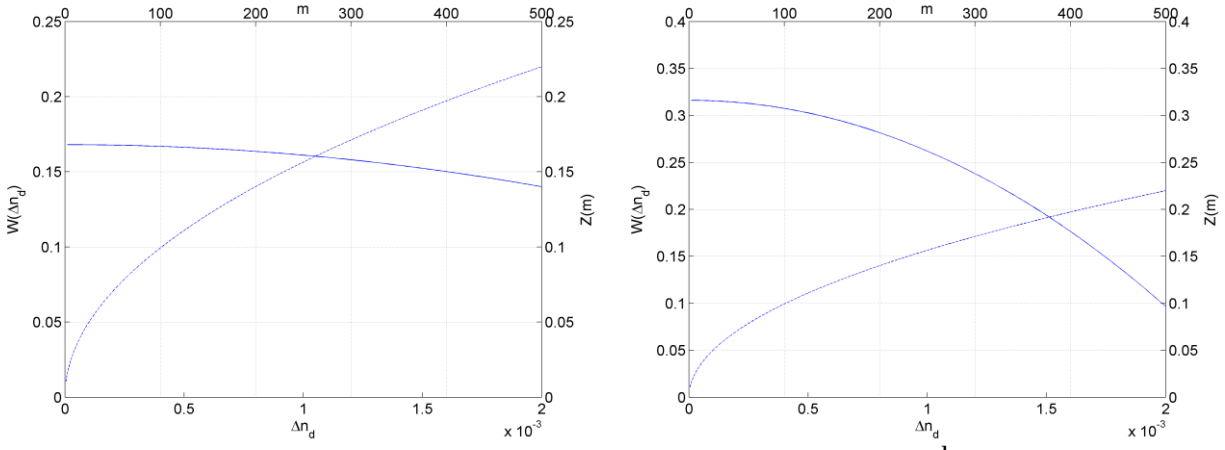

Figure 2.11: $W(\Delta n_e)$ **(solid line) and** $Z(m)$ **(dashed line)** for **(a)** $L = 40.05\mu m$ **, (b)** $L = 80\mu m$

Solution No.	m	$R(\mu m)$	$\lvert\Delta n_d\rvert \times 10^{-3}$	$\lvert\Delta n_2\rvert \times 10^{-3}$	$V(Volt)$	$T_{\max}(dB)$	$T_{\min}(dB)$	$\zeta(dB)$
1	290	20.4	0.06433	0.3	0.26	-75.09	-104.43	29.34
2	250	15.8	1.30572	6.4	5.27	-22.59	-104.37	81.78
3	201	10.2	1.998	10	8.08	-14.83	-102.98	88.15

Table 2.4: Circuit parameters for $L = 40.05\ \mu m$

Solution No.	m	$R(\mu m)$	$\lvert\Delta n_d\rvert\times10^{-3}$	$\lvert\Delta n_2\rvert\times10^{-3}$	$V(Volt)$	$T_{\max}(dB)$	$T_{\min}(dB)$	$\zeta(dB)$
1	1000	88.72	0.42048	2	1.67	-29.9	-109.96	80.06
2	900	77.3	0.67557	3.27	2.73	-21.47	-110.91	89.44
3	800	65.88	0.86774	4.2	3.54	-16.92	-114	97.08
4	700	54.46	1.03431	5	4.17	-13.67	-165.6	151.93
5	600	43.04	1.18799	5.75	4.79	-11.07	-120.38	109.31
6	500	31.6	1.33566	6.47	5.39	-8.84	-114.86	106.02
7	400	20.2	1.48245	7.18	5.99	-6.85	-109.31	102.46
8	300	8.8	1.63369	7.92	6.60	-5.02	-114.36	109.34
9	**267**	**5**	**1.68576**	**8.17**	**6.81**	**-4.45**	**-114.00**	**109.55**
10	224	0.1	1.75623	8.51	7.09	-3.70	-103.42	99.72
11	200	-2.6	1.79725	8.71	7.26	-3.30	-119.41	116.11
12	97	-14.4	1.99785	9.69	8.08	-1.59	-108.10	106.51

Table 2.5: Circuit parameters for $L = 80\ \mu m$

2.3 Conclusion

In this chapter we proposed a novel tunable ring resonator circuit and demonstrated two techniques for tuning the transmission characteristics, the first of which modifies the resonance states of the ring while the second alters the phase of the field at the ring-bus coupling region. Our circuit is compatible with SOI technology, is expected to exhibit a high switching speed of $20-100\,GHz$ [12] , [65] even when driven with a single voltage, while the circuit in [45] requires different polarities to enhance the carrier-lifetime limited circuit speed that is in any case far below that of our circuit. Further, the optical losses and therefore the transmission characteristics of our circuit are independent of *V*, in contrast to [45]. Our circuits incorporate the ease of manufacture and the small waveguide dimensions of silicon technology with the high switching speed of polymer technology. We therefore believe that our design could find application in practical integrated optic structures. The circuit is also compatible with silicon devices and could also be employed in WDM applications.

Additional wavelength selectivity should further be achievable by increasing the overlap between the propagating power and the polymer layer perhaps as in [67] where the modal field is shifted towards the polymer layer by an intermediate thin high RI layer between the silicon and the polymer. Alternatively, push-pull driving electrodes could decrease the tuning voltage by half [65]. Multiple ring circuits with more complex transmission characteristics can also be designed if required. Finally, while ring resonator circuits sensitive to fabrication tolerance through the coupling and resonance conditions, a tunable structure can compensate for such a tolerance through the adjustable external voltage.

Chapter 3
Compound ring resonators

The single ring circuit of the previous chapter exhibits a near-Lorentzian power transmission which is inadequate for some applications such as complex filters. Ring resonator circuits with additional rings coupled in series or parallel have previously been proposed to adapt the power transmission to different application requirements [43], [68]. Here we examine a different structure consisting of a closed loop of coupled rings which we term a "compound ring resonator circuit". The internal feedback between the rings facilitates the shaping of the transmission characteristics as we demonstrate through the design of a signal interleaver. We will analyze this circuit with the coupling of modes in space (CMS), and time (CMT) methods as well as through finite difference time domain (FDTD) simulations and contrast the accuracy of the three procedures. We then design, fabricate and characterize a WDM interleaver/ deinterleaver based on this circuit.

3.1 Transfer matrix approach

In this section we introduce the compound ring structure and calculate the electric field of the through and drop ports. The compound ring resonator (RR) circuit structure is shown in Figure 3.1 where identical rings with mean radius R are, for simplicity, evenly distributed within two outer bus waveguides such that their centers are located on the vertices of a uniform polygon. The number of rings, N, is chosen to be even to avoid electric field reflection at the input ports. The ring field components are denoted a_j, b_j, c_j and d_j with $1 \le j \le N$. The ports of the upper bus are labeled I and II for the input, a_o and output b_o fields while the lower bus ports are labeled III and IV with corresponding input and output fields a_{oo} and b_{oo} respectively. The gaps between two neighboring rings, between ring $j = 1$ and the first bus, and between ring $j = N/2 + 1$ and the second bus are denoted g, g_o and g_{oo} respectively. The corresponding field coupling ratios are k, k_o and k_{oo} defined as the ratio of the field coupled between two neighboring components. The width of all waveguides is denoted by w.

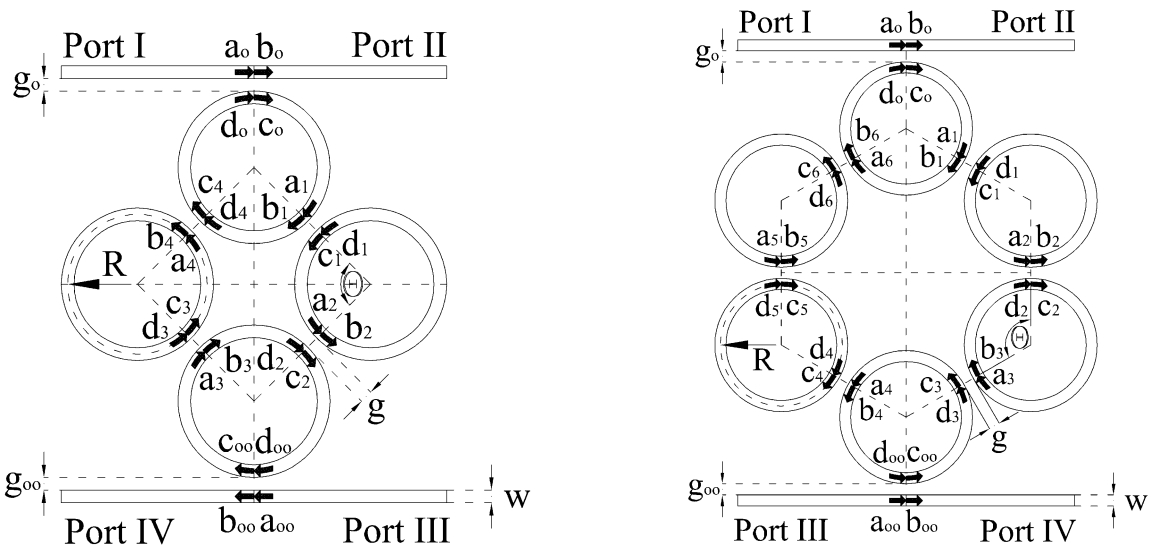

Figure 3.1: The compound ring resonator circuit with (a) $N=4$, (b) $N=6$ ring resonators.

To compute the circuit transmission characteristics we employ the transfer matrix method [43], [68] in which the electric field components are related through two types of matrices. These are the coupling matrices: $\begin{bmatrix} d_o \\ c_o \end{bmatrix} = Q_o \begin{bmatrix} a_o \\ b_o \end{bmatrix}$, $\begin{bmatrix} d_{oo} \\ c_{oo} \end{bmatrix} = Q_{oo} \begin{bmatrix} a_{oo} \\ b_{oo} \end{bmatrix}$, $\begin{bmatrix} d_j \\ c_j \end{bmatrix} = Q \begin{bmatrix} a_j \\ b_j \end{bmatrix}$, $1 \le j \le N$, with $Q_o = \frac{1}{ik_o}\begin{bmatrix} r_o & -1 \\ 1 & -r_o \end{bmatrix}$, $Q_{oo} = \frac{1}{ik_{oo}}\begin{bmatrix} r_{oo} & -1 \\ 1 & -r_{oo} \end{bmatrix}$, $Q = \frac{1}{ik}\begin{bmatrix} r & -1 \\ 1 & -r \end{bmatrix}$, $k_o^{\,2} + r_o^{\,2} = 1$, $k_{oo}^{\,2} + r_{oo}^{\,2} = 1$, and $k^2 + r^2 = 1$ and the phase matrices: $\begin{bmatrix} a_{2j} \\ b_{2j} \end{bmatrix} = P_1 \begin{bmatrix} d_{2j-1} \\ c_{2j-1} \end{bmatrix}$, $1 \le j \le N/2$ and $\begin{bmatrix} a_{2j+1} \\ b_{2j+1} \end{bmatrix} = P_2 \begin{bmatrix} d_{2j} \\ c_{2j} \end{bmatrix}$, $1 \le j \le N/2 - 1$ with $P_1 = \begin{bmatrix} 0 & e^{-i\delta_1} \\ e^{i\delta_2} & 0 \end{bmatrix}$, $P_2 = \begin{bmatrix} 0 & e^{-i\delta_2} \\ e^{i\delta_1} & 0 \end{bmatrix}$. Here $\delta = \phi - i\frac{\alpha}{2}l$, ϕ is the round trip phase shift, $l = 2\pi R$, α is the power loss coefficient, $\delta_1 = \delta \times \frac{\theta}{2\pi}$, $\delta_2 = \delta \times (1 - \frac{\theta}{2\pi})$ and $\theta = \frac{N-2}{N}\pi$ for a uniform polygon. By symmetry we have $P_1 = P_2^{-1}$ so that when all coupling coefficients are equal the matrix $U = P_2 Q P_1 Q$ is unimodular. Note that while coupling matrices have been introduced for all the rings in the circuit, the phase matrices equations above are only employed for the rings that are not coupled to buses. Special matrices, V_1 and V_2, are needed along with the phase matrices for the rings coupled to the buses as shown below. We consider the case that $a_{oo} = 0$ so that the input to the circuit is $a_o \neq 0$, and the circuit functions as a deinterleaver with through (b_o) and drop (b_{oo}) ports. Again because of the symmetry of the circuit, similar results

apply if $a_{oo} \neq 0$ and $a_o = 0$ and k_o and k_{oo} are interchanged. Operating as an interleaver both input fields are nonzero ($a_o \neq 0$ and $a_{oo} \neq 0$), which is a superposition of the two above cases. Accordingly, we take

$$b_1 = \rho_1 a_1 + \tau_2 d_N \quad \textbf{(3.1.a)}$$

$$c_N = \rho_2 d_N + \tau_1 a_1 \quad \textbf{(3.1.b)}$$

in which $\tau_{1,2}$ and $\rho_{1,2}$ are determined below. Setting

$$X = \begin{bmatrix} x_1 & x_2 \\ x_3 & x_4 \end{bmatrix} \quad \textbf{(3.2.a)}$$

$$Y = \begin{bmatrix} y_1 & y_2 \\ y_3 & y_4 \end{bmatrix} \quad \textbf{(3.2.b)}$$

and

$$\begin{bmatrix} d_N \\ c_N \end{bmatrix} = X \begin{bmatrix} a_1 \\ b_1 \end{bmatrix} \quad \textbf{(3.3)}$$

we have for odd $N/2$

$$\begin{bmatrix} a_{N/2+1} \\ b_{N/2+1} \end{bmatrix} = Y_1 \begin{bmatrix} a_1 \\ b_1 \end{bmatrix} \quad \textbf{(3.4.a)}$$

$$Y = Y_1 = V_1 (P_1 Q) U^{(N-2)/4} \quad \textbf{(3.4.b)}$$

$$V_1 = \begin{bmatrix} 1 & 0 \\ 0 & 1/r_{oo} \end{bmatrix} \quad \textbf{(3.4.c)}$$

$$X = P_1 U^{(N-2)/4} (P_2 Q) Y \quad \textbf{(3.4.d)}$$

If instead $N/2$ is even,

$$\begin{bmatrix} d_{N/2} \\ c_{N/2} \end{bmatrix} = Y_2 \begin{bmatrix} a_1 \\ b_1 \end{bmatrix} \quad \textbf{(3.5.a)}$$

$$Y = Y_2 = P_1 U^{N/4} \quad \textbf{(3.5.b)}$$

$$V_2 = \begin{bmatrix} r_{oo} & 0 \\ 0 & 1 \end{bmatrix} \tag{3.5.c}$$

$$X = X_2 = P_1 U^{N/4} V_2 P_2 Y \tag{3.5.d}$$

Applying the boundary condition

$$d_N = b_1 e^{-i\delta_1} \tag{3.6}$$

together with $d_N = x_1 a_1 + x_2 b_1$, $c_N = x_3 a_1 + x_4 b_1$, we find for $d_N = 0$

$$\rho_1 = \frac{b_1}{a_1} = -\frac{x_1}{x_2} \tag{3.7.a}$$

$$\tau_1 = \frac{c_N}{a_1} = x_3 - \frac{x_1 x_4}{x_2} \tag{3.7.b}$$

while for $a_1 = 0$

$$\rho_2 = \frac{c_N}{d_N} = \frac{x_4}{x_2} \tag{3.8.a}$$

$$\tau_2 = \frac{b_1}{d_N} = \frac{1}{x_2} \tag{3.8.b}$$

Therefore the internal device field reflection and transmission coefficients are

$$\rho_i = \frac{b_1}{a_1} = \frac{\rho_1}{1 - \tau_2 e^{-i\delta_1}} \tag{3.9.a}$$

and

$$\tau_i = \frac{c_N}{a_1} = \frac{\tau_1 + (\rho_1 \rho_2 - \tau_1 \tau_2) e^{-i\delta_1}}{1 - \tau_2 e^{-i\delta_1}} \tag{3.9.b}$$

Setting, $b_o = -ik_o d_o + r_o a_o$, $c_o = -ik_o a_o + r_o d_o$, $d_o = c_N e^{-i\delta_2/2}$ and $c_o = a_1 e^{+i\delta_2/2}$ we obtain $\frac{a_1}{a_o} = \frac{-ik_o}{e^{i\delta_2/2} - \tau_i r_o e^{-i\delta_2/2}}$. With $\rho_o = \frac{b_o}{a_o} = r_o - ik_o \frac{d_o}{a_o}$ and $\frac{d_o}{a_o} = \frac{d_o}{c_N} \times \frac{c_N}{a_1} \times \frac{a_1}{a_o}$ we have $\rho_o = \frac{b_o}{a_o} = r_o - \frac{k_o{}^2 e^{-i\delta_2/2}}{e^{i\delta_2/2} - \tau_i r_o e^{-i\delta_2/2}} \tau_i$ which leads to the through-port transmission,

$$\rho_o = \frac{b_o}{a_o} = \frac{r_o - \tau_i e^{-i\delta_2}}{1 - r_o \tau_i e^{-i\delta_2}} = |\rho_o| e^{i\Phi_o} \qquad \textbf{(3.10)}$$

This is identical to the expression for reflection from a single ring if the round trip complex phase shift term, $e^{-i\delta}$, replaces the term $\tau_i e^{-i\delta_2}$. For $N/2$ odd $\frac{b_{oo}}{a_o} = \frac{b_{oo}}{d_{oo}} \times \frac{d_{oo}}{b_{N/2+1}} \times \frac{b_{N/2+1}}{a_1} \times \frac{a_1}{a_o}$ so that $\frac{b_{oo}}{a_o} = -ik_{oo} \times e^{-i\delta_2/2} \times (y_3 + y_4 \rho_i) \times \frac{a_1}{a_o}$. The drop-port transmission for the circuit is therefore,

$$\tau_o = \frac{b_{oo}}{a_o} = \frac{-k_o k_{oo}(y_3 + y_4 \rho_i)}{e^{i\delta_2} - \tau_i r_o} = |\tau_o| e^{i\Psi_o} \qquad \textbf{(3.11)}$$

in which Φ_o and Ψ_o represent the phase shift of the fields relative to the input field phase. For even $N/2$, $\tau_o = \frac{b_{oo}}{a_o} = \frac{b_{oo}}{d_{oo}} \times \frac{d_{oo}}{c_{N/2}} \times \frac{c_{N/2}}{a_1} \times \frac{a_1}{a_o}$ again yielding equation (3.11) with the matrices of equations (3.5.a) – (3.5.d). To conclude this section, the compound ring transmission characteristics are given by equations (3.10) and (3.11) for the through and drop ports respectively. In the following section, those characteristics are optimized to match the standard WDM interleaver / deinterleaver circuit specifications.

3.2 WDM compound ring resonator structure interleaver circuit

In this section we employ the compound RR structure presented in the previous section to build a standard WDM deinterleaver circuit. An interleaver circuit combines signals from two different optical channels carrying odd and even signals into one stream with half the channel spacing, while a deinterleaver splits one stream into two [69]. The requirements on this circuit are as follows [43], [69]: The channel spacing was taken to be $50GHz$ and the free spectral range, FSR, of a channel was set to $100GHz$. The cross-talk, defined as the maximum transmission of a channel within $\pm 10GHz$ of the maximum transmission frequency of the neighboring channel should be $< -23dB$. The absolute value of the signal dispersion should likewise be limited to $< 30ps/nm$ within the channel bandwidth ($\pm 10GHz$). Finally, the shape factor of the pass-band, arbitrarily defined as the ratio of the $-1dB$ bandwidth to the $-10dB$ bandwidth, is preferably greater than 0.6.

We study two cases to illustrate the dynamics of the circuit response before we discuss the optimum design. We first transform the field transmission of the two output ports into the Z-domain [70-71]. The Z-transform analysis enables an improved understanding of the circuit pole-zero dynamics therefore facilitates design optimization as illustrated by the three examples below. Here we first substitute $z_o = e^{i\phi}$ in equations (3.10) and (3.11) such that $\phi = \beta l$ represents a normalized frequency. We follow the same assumptions as in [43] and [69], so that the power loss after a round trip around a ring is 10% [43] while the straight waveguides are considered lossless. The free space wavelength is taken as $\lambda_o = 1.55\mu m$. This leaves three adjustable parameters, k, k_o and k_{oo} of which we take $k_o = k_{oo}$ for simplicity and, more importantly, for symmetry. For each choice of the two remaining coupling coefficients, we can then evaluate ρ_o and τ_o numerically in terms of z_o. The zeros are the solutions of $\rho_o = 0$ and $\tau_o = 0$, while the poles are computed from the solutions to $1/\rho_o = 0$ and $1/\tau_o = 0$. Since one revolution around the unit circle in Z-domain corresponds to a $FSR = 100GHz$, while the passband of each channel is $\pm 10\,GHz$ about the channel maximum transmission, the passband of a channel is $\pm\pi/5 = \pm 36^o$ around the angle corresponding to the channel maximum transmission. In the following results, the solid (dashed) line on the graphs represents the results for the through (drop) channel. We have studied the filter response for numerous values of the coupling coefficients. Two illustrative examples of the filter dynamics are presented in cases A and B below while the optimal design is given in case C

Case A: We set $k_o = k_{oo} = 0.935$, while increasing k from 0.5 to 0.6 in steps of 0.025. This leads to the circuit response of Figure 3.2.a through 3.2.g. For our compound ring resonator circuit, as all RR circuits, the through (drop) port has the spectrum maximum (minimum) centered at $\phi/\pi = \pm 1, \pm 3, ..$ and the minimum (maximum) centered at $\phi/\pi = 0, \pm 2, \ldots$ since the electric field interferes destructively within an off-resonance ring i.e. $\phi/\pi = \pm 1, \pm 3, ..$ and constructively within an on-resonance ring, $\phi/\pi = 0, \pm 2, ...$ The transmission spectra of the two channels are complementary for lossless rings. Also, when k increases, more power is exchanged between the two channels and consequently the cross-talk is higher as in Figure 3.2.a. Both channels represent autoregressive moving average (ARMA) filters since both have poles and zeros, as shown in Figure 3.2.f and 3.2.g. The numbers in the diagrams indicate the multiplicity of the poles and zeros. The through port has the poles and zeros outside the passband, $\phi/\pi = 1 \pm 0.2$, while the drop port has its poles and zeros inside or close to the passband $\phi/\pi = 0 \pm 0.2$. The pole-zero dynamics clearly explain the dispersion curve since increasing k displaces the poles and zeros towards the passband of the through port and away from the passband of the drop port. Consequently, the absolute value of the dispersion increases for the through port field and decreases for the drop port field within the corresponding passbands.

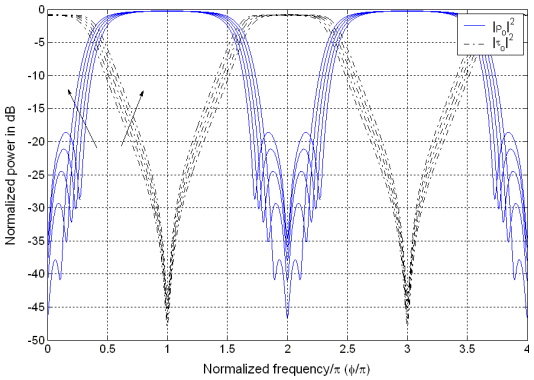
Normalized power in dB
Normalized frequency/π (ϕ/π)

(a)

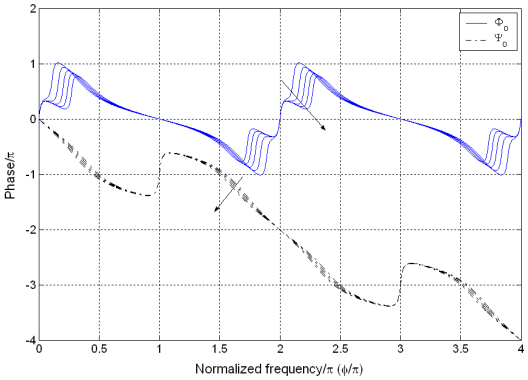
Phase/π
Normalized frequency/π (ϕ/π)

(b)

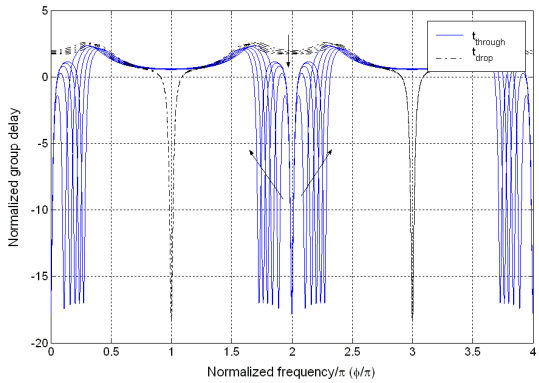
Normalized group delay
Normalized frequency/π (ϕ/π)

(c)

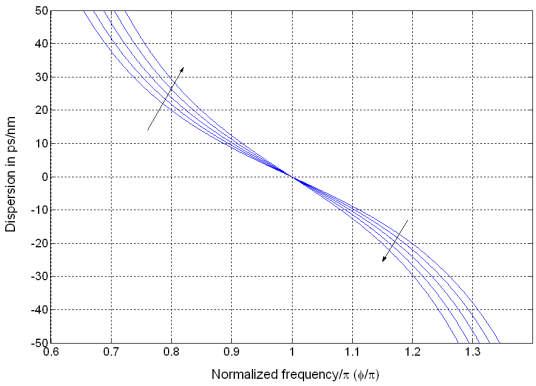
Dispersion in ps/nm
Normalized frequency/π (ϕ/π)

(d)

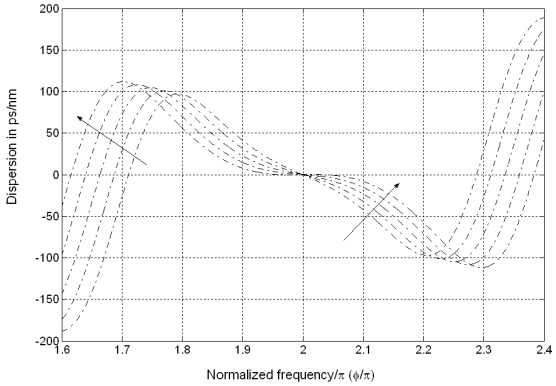
Dispersion in ps/nm
Normalized frequency/π (ϕ/π)

(e)

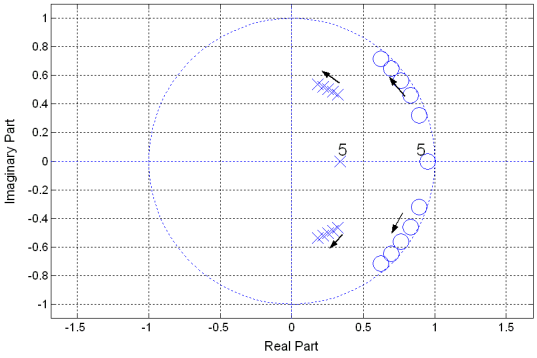
Imaginary Part
Real Part

(f)

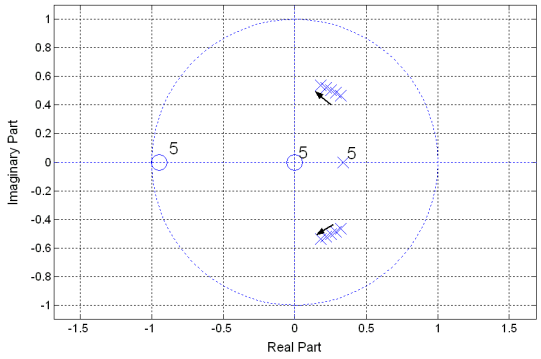

(g)

Figure 3.2: The circuit response with $k_o = k_{oo} = 0.935$ and k increasing from 0.5 to 0.6 in steps of 0.025. The arrows indicate increasing parameter values. The round trip power loss is 10%. (a) The power spectra. (b) The phase variation. (c) The normalized group delay. (d) The through port dispersion. (e) The drop port dispersion. (f) The through port pole-zero diagram. (g) The drop port pole-zero diagram.

Case B: Here we set $k = 0.525$, while $k_o = k_{oo}$ is increased from 0.885 to 0.985 in steps of 0.025. The circuit response is now that of Figure 3.3.a through Figure 3.3.g. Again, increasing the coupling coefficients, k_o and k_{oo} increases the cross-talk for the channels. For the through port, we observe from Figure 3.3.a and 3.3.f that the channel possesses three zeros, a real one lying at angle "0" that generates the minimum at $\phi/\pi = 0 \pm 2\pi$ on Figure 3.3.a and a complex conjugate pair that is associated with the local minima and the side lobes on the sides of the passband. The complex zeros are displaced towards the real axis, as k_o increases, and then divide so that the zeros posses real and reciprocal values. In this case, only one minimum appears in the power spectrum which then lacks of side-lobes. The motion of the zeros and poles in Figure 3.3.f agrees with the decrease in the absolute value of the dispersion of the through channel as shown in Figure 3.3.d since they move away from the passband as k_o and k_{oo} increase. Additionally, Figure 3.3.f and 3.3.g indicate that the distance of the pole positions from the origin decreases with increased k_o so that the influence of the poles on the power spectrum is diminished. This also explains the decreased dispersion magnitude for the drop port evident in Figure 3.3.e.

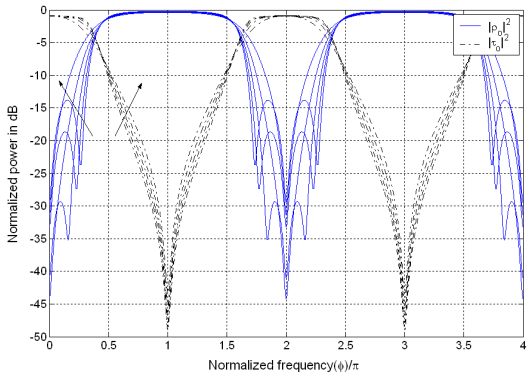
Normalized power in dB
Normalized frequency(ϕ)/π

(a)

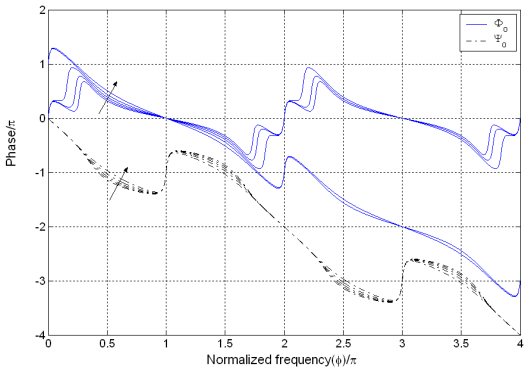
Phase/π
Normalized frequency(ϕ)/π

(b)

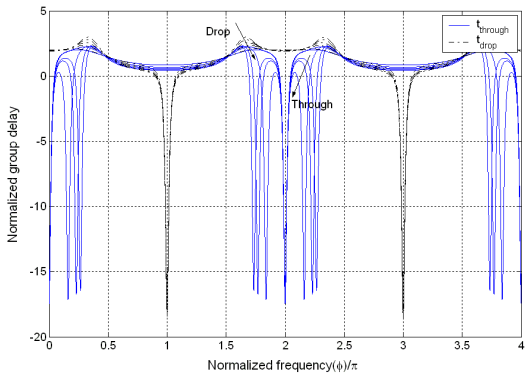
Drop
Through
Normalized group delay
Normalized frequency(ϕ)/π

(c)

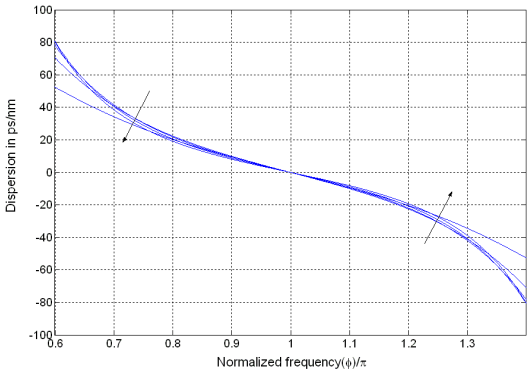
Dispersion in ps/nm
Normalized frequency(ϕ)/π

(d)

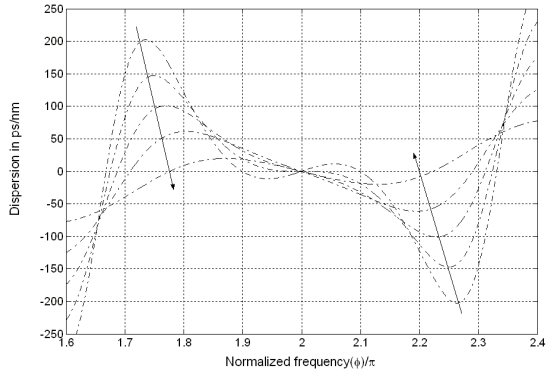
Dispersion in ps/nm
Normalized frequency(ϕ)/π

(e)

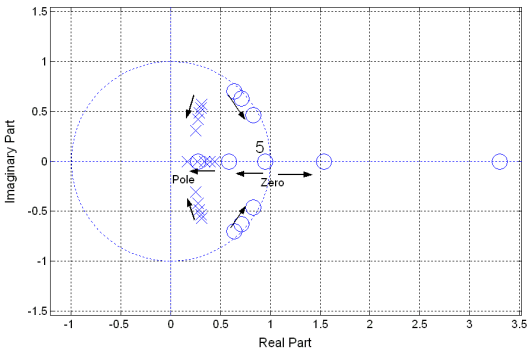
Imaginary Part
Real Part
Pole
Zero

(f)

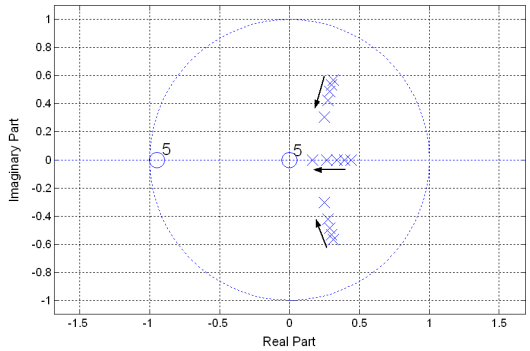

(g)

Figure 3.3: The circuit response with $k = 0.525$ and $k_o = k_{oo}$ increasing from 0.885 to 0.985 in steps of 0.025. The arrows indicate increasing parameter values. The round trip power loss is 10%. (a) The power spectra. (b) The phase variation. (c) The normalized group delay. (d) The through port dispersion. (e) The drop port dispersion. (f) The through port pole-zero diagram. (g) The drop port pole-zero diagram.

Case C: From the discussion of cases A and B, the optimum values of the coupling coefficients in the circuit are $k = 0.525$ and $k_0 = k_{oo} = 0.935$ with the circuit response presented in Figure 3.4.a through 3.4.g. The cross-talk for both channels is found to be $-24\,dB$ while the maximum dispersion of the through channel is $\pm 22\ ps/nm$ which satisfies our stated design requirements. However the drop port exhibits a maximum dispersion ($\pm 93\ ps/nm$) that exceeds the maximum allowed dispersion ($\pm 30\ ps/nm$). Therefore, a second stage must be employed at the drop port formed from a single ring resonator circuit, as shown in Figure 3.5. The ring is coupled to the drop port and is designed to act close to a unity filter, where the transmission amplitude is nearly equal to $0dB$, as shown in Figure 3.6.a. This does not add significant ripples to the drop channel spectrum. The pole and zero of the single ring possess real and reciprocal values as displayed in Figure 3.6.e. Note that $k_{oo} = 0$ for this stage since only one bus is coupled to the fifth ring.

The combined circuit response at the drop port is shown in Figure 3.7.a through 3.7.e. Since the dispersion of the two stages is equal in magnitude but opposite in sign, the absolute value of the total dispersion is decreased. We have also studied the possibility of using a Mach Zender Interferometer (MZI) to reduce the dispersion at the drop port. From Figure 3.4.g we observe that by placing two MZIs in series with the drop port of our circuit we can create two zeros in the Z-transform domain that are located in close proximity to the two complex poles thus decreasing the dispersion. Unfortunately, we have found that such a procedure generates ripples (transmission amplitude variations) in the passband and of course also increases the circuit area.

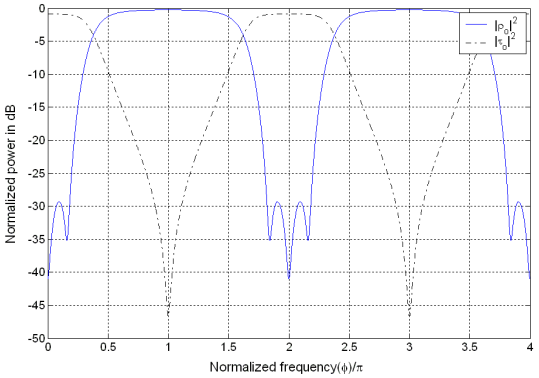
Normalized power in dB
Normalized frequency(ϕ)/π

(a)

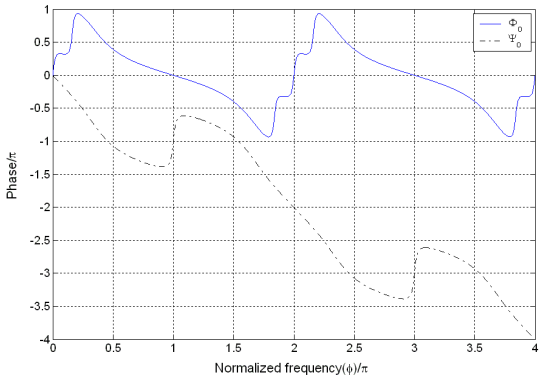
Phase/π
Normalized frequency(ϕ)/π

(b)

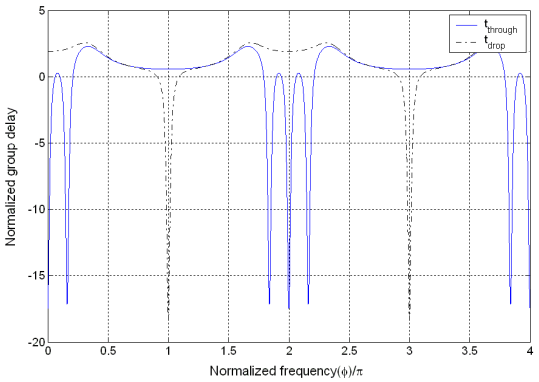
Normalized group delay
Normalized frequency(ϕ)/π

(c)

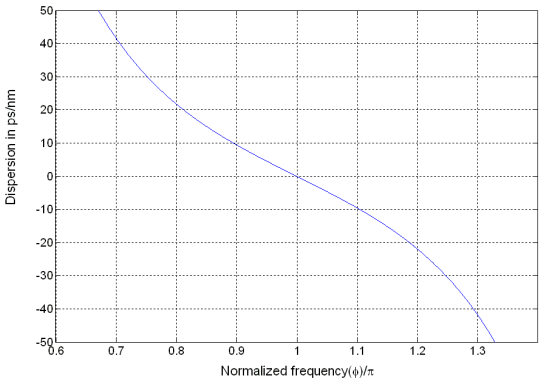
Dispersion in ps/nm
Normalized frequency(ϕ)/π

(d)

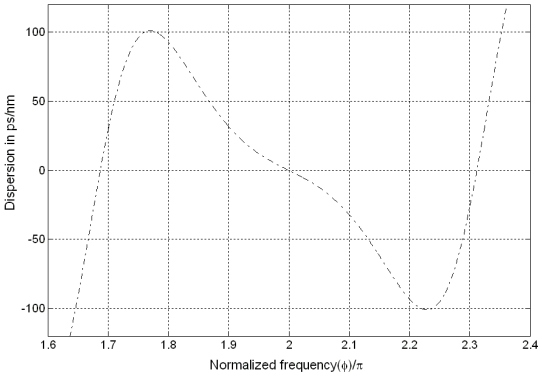
Dispersion in ps/nm
Normalized frequency(ϕ)/π

(e)

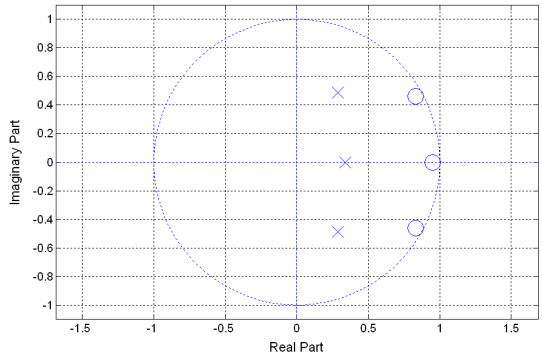
Imaginary Part
Real Part

(f)

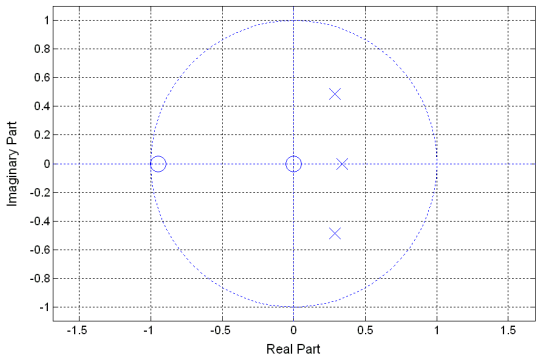

(g)

Figure 3.4: The circuit response with $k = 0.525$ and $k_o = k_{oo} = 0.935$ for a round trip power loss of 10%. (a) The power spectra. (b) The phase variation. (c) The normalized group delay. (d) The through port dispersion. (e) The drop port dispersion. (f) The through port pole-zero diagram. (g) The drop port pole-zero diagram.

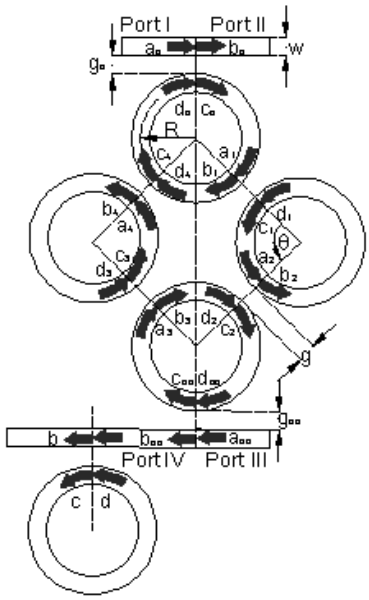

Figure 3.5: A compound four ring circuit attached to a single ring stage.

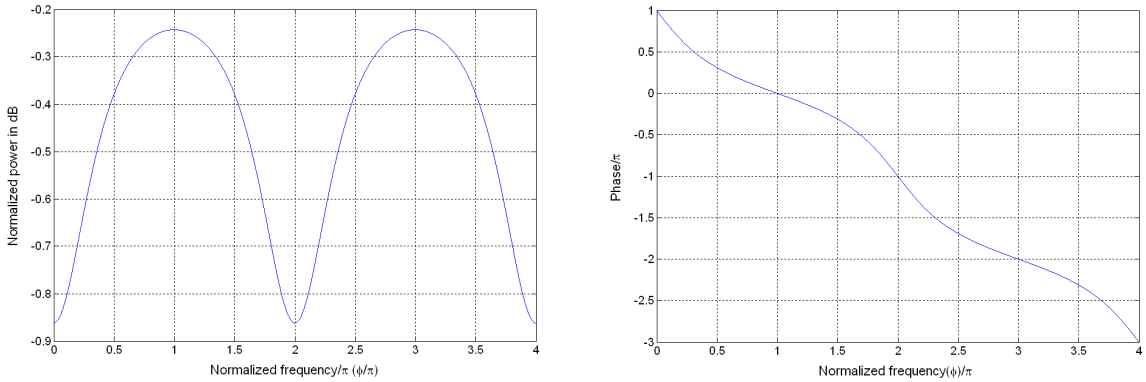

(a)

(b)

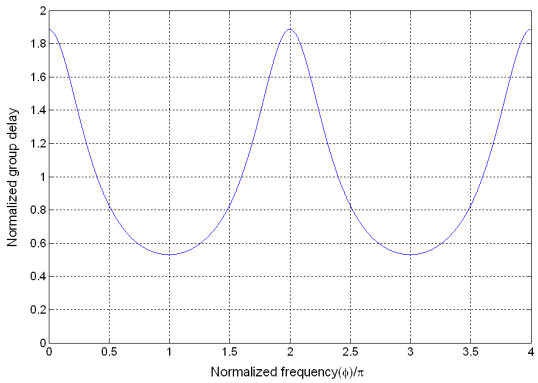

(c)

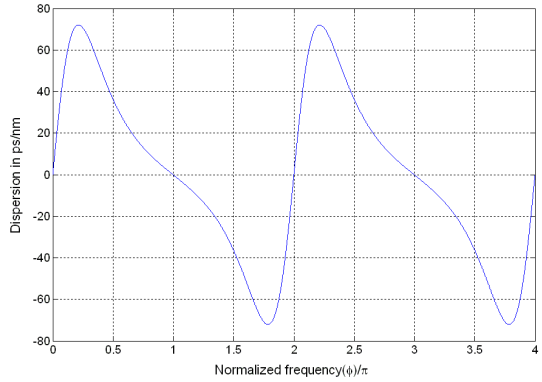

(d)

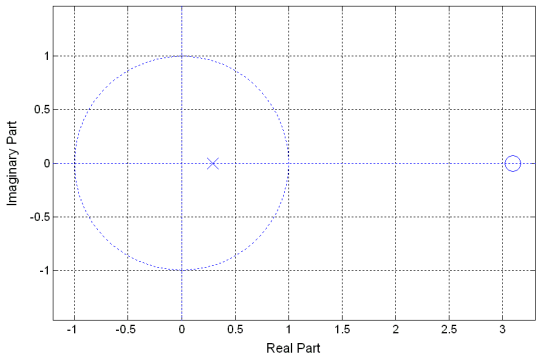

(e)

Figure 3.6: The single ring stage response with $k_o = 0.952$ and $k_{oo} = 0$ for a round trip power loss of 10%. (a) The power spectra. (b) The phase variation. (c) The normalized group delay. (d) The through port dispersion. (e) The through port pole-zero diagram.

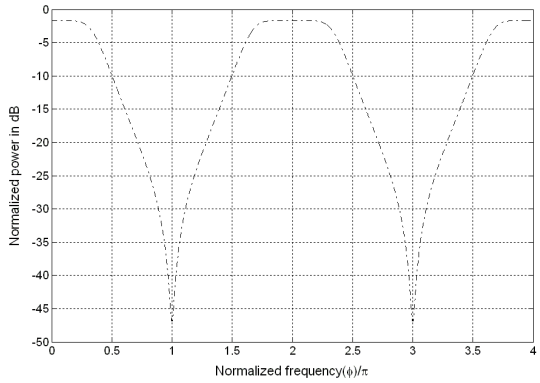

(a)

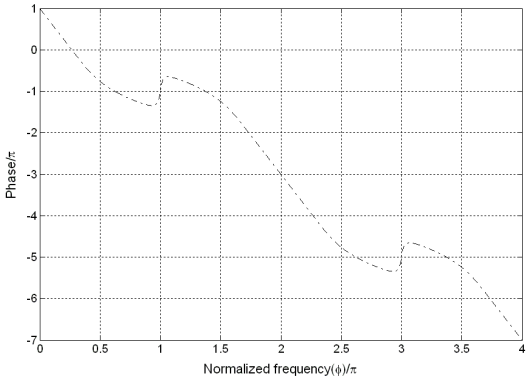

(b)

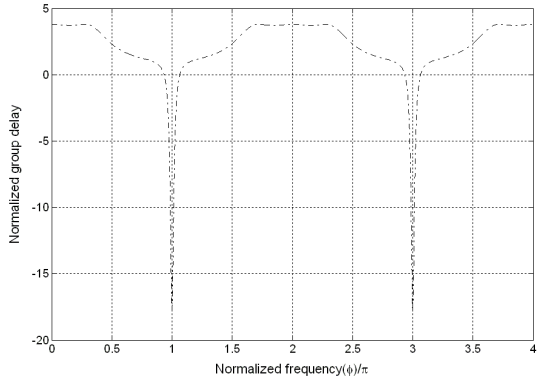

(c)

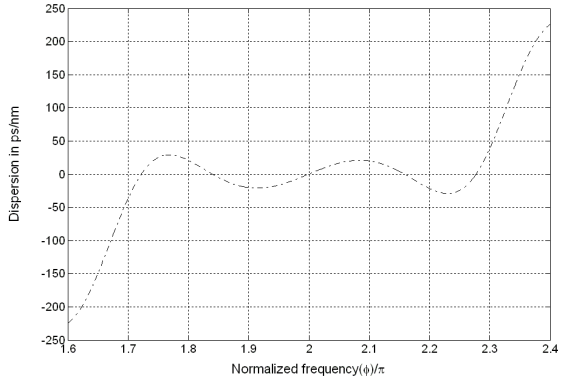

(d)

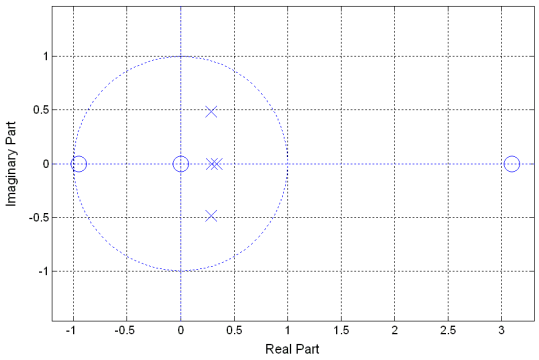

(e)

Figure 3.7: The drop port response with an additional single ring stage for a round trip power loss equal to 10%. (a) The power spectra. (b) The phase variation. (c) The normalized group delay. (d) The drop port dispersion. (e) The drop port pole-zero diagram.

3.3 Comparison of interleavers

We found that the best circuit of the same nature, i.e. a RR based interleaver circuit; to compare with is found in [43] where many RR based interleaver circuits were studied before the authors got to their optimal design. Hence we present in Table 3.1 a comparison of our proposed WDM interleaver circuit, based on the compound RR structure, to the previously published [43] two stage interleaver circuit formed from four rings in parallel followed by three rings in series which matches the same WDM requirements. The circuit area in [43] and in this work are obtained by neglecting the gaps between the rings and the bus-lines with respect to the ring radius. We also assume that for the circuit in [43], the distance between the two stages is half the ring circumference in the same manner as the distance between two consecutive ring centers in the first stage. Finally, the circuit area corresponds to the area of a rectangle of two sides representing the largest two perpendicular dimensions of the circuit. Our new circuit clearly satisfies the interleaver/deinterleaver circuit requirements but offers additional advantages compared to the other circuit [43]. Namely, our RR circuit occupies 38% of the area of [43] and only requires 5 rings instead of 7, simplifying the design and fabrication. While the values of k from one end of the ring array to the other were varied symmetrically (apodization) in [43], the fabrication must be extremely accurate for the gap distance between coupled rings to be sufficiently precise enough that the desired value of k is obtained. Moreover, since the difference between the coupling values is about 0.08 [43], fabrication tolerances in the range of nanometers would affect the circuit performance. Moreover, apodization increases the design parameters and consequently the design complexity. On the other hand, in our compound ring circuit, apodization is unnecessary and in fact we found in additional calculations that it did not significantly affect our results. Therefore, our compound RR based interleaver has a greater fabrication tolerance compared with the optimal design in [43]. Finally, the compound circuit exhibits competitive values of the dispersion, the insertion loss and the passband shape factor as presented in Table 3.1.

	Crosstalk dB (through/drop)	Dispersion ps/nm (through/drop)	Area	Shape factor (through/drop)	Insertion loss dB (through/drop)
Requirements [43], [60]	$-23/-23$	$\pm 30/\pm 30$	min	>0.6	Minimum
Circuit in [43]	$-37/-35$	$\pm 25/\pm 25$	$87.4R^2$	$0.552/0.516$	$0.5/0.5$ [1]
Compound RR circuit	$-24/-24$	$\pm 22/\pm 21$	$33R^2$	$0.662/0.5$ [2]	$0.3/1.7$

Table 3.1: The performance of the optimal design in [43] compared to the "compound RR circuit" performance.

As a conclusion of this section, the new WDM interleaver exceeds the performance and simplicity of previously reported ring resonator interleaver circuits. The layout of the rings is also approximately circular, which reduces fabrication area and thus increases the package density with a greater fabrication tolerance. Additionally, such a design might also function as a building block in other applications such as optical delay lines.

3.4 CMT analysis

In this section, we analyze the compound ring resonator structure for small coupling, with both the CMT and the FDTD methods. With the CMT, the RR is modeled as a lumped oscillator [3], [72] such that, for sufficiently small coupling, i.e. the energy coupling coefficient μ^2 defined below is much smaller than the resonance frequency of the ring, the electric field amplitude changes negligibly across the region over which two elements in the circuit are coupled. This leads to simpler equations than in the CMS. However, this procedure requires that the power coupling ratio between two adjacent elements is small, the power loss is small, and further only evaluates the circuit transmission characteristics over narrow frequency bands around the resonance frequencies.

We also show that, while the FDTD is a robust technique [3], it demands substantial computational resources especially for three dimensional (3D) complicated structures with large RR radii. Although the effective index technique [17] can in certain cases be applied to generate an equivalent 2D waveguide profile, for design purposes, the device transmission spectra must be calculated for numerous values of the loss and coupling coefficients which is very time consuming with the FDTD simulations.

[1] The shape factor and the insertion loss of the presented design in [43] are not specified. Therefore, we calculated these values based on the equations presented in [43].

[2] The passband shape factor for the drop port is defined here as the ratio of the $-2dB$ bandwidth to the $-11dB$ bandwidth because of the additional stage loss.

We also show that for small coupling and losses, the results of these techniques agree with each other and with the CMS procedure employed previously. We also find the relationship between the loss factors in the CMS and the CMT models and apply the CMT to a lossy circuit. We find that the CMT yields rapid and accurate results for the transfer characteristics about the resonance frequencies despite the complexity of our example, which is considerably more demanding than that analyzed in [3].

3.4.1 CMS circuit parameters

To compare the CMS and CMT models, we now examine the compound RR structure in Figure 3.8 but with the coupling and loss coefficients given in [3] in 2D, which satisfy the limits of small coupling and losses. The bus and ring structures possess a core and cladding refractive index (RI) of $n_1 = 3$, and $n_2 = 1$, and a width of $w = 0.2\ \mu m$. For these values, a mode solver yields $n_e = 3.08 - 0.536 \times 10^6 \lambda_o$ for the transverse electric (TE) field mode in the vicinity of $\lambda_o = 1.334\ \mu m$, from which $n_e = 2.37$ at $\lambda_o = 1.334\ \mu m$. The group RI is given by $n_g = n_e - \lambda_o \frac{dn_e}{d\lambda_o}$, which yields $n_g = 3.08$ at $\lambda_o = 1.334\ \mu m$.

We next determine the coupling coefficients for $R = 1.7 \mu m$ and $g = g_o = g_{oo} = 0.2\ \mu m$. First we apply the analytic result, based on coupled mode theory, in the appendix of [3], for the coupling coefficient between two straight parallel waveguides (buses), κ, which yields, $k_b = \sin(\kappa l_b)$ for the fraction of the coupled field where l_b is the interaction length. For the coupling between a bus and a ring or between two rings, we employ $l_m = \sqrt{\frac{\lambda_o R_m}{2\sqrt{n_e^{\ 2} - n_2^{\ 2}}}}$, with $R_m = R_1 R_2 / (R_1 + R_2)$ where R_1 and R_2 are the radii of the two coupled elements, instead of l_b. Additionally, for small coupling we can approximate $k_m = \sin(\kappa l_m) \approx \kappa l_m$. In this manner, we find $\kappa = 25.3 / \mu m$, $k_o = k_{oo} = 18\%$ and $k = 13\%$. We have also repeated this calculation with the BPM , by launching power into one of the two straight waveguides separated by a distance of $0.2\ \mu m$. Monitoring the power in the two waveguides yields a coupling coefficient $\kappa = 26.18 / \mu m$. Similarly, we investigated the coupling between a straight waveguide and 20 degrees of a neighboring ring [19]. Equating the power coupled into the ring to the power lost from the straight waveguide, yields $k_o = k_{oo} = 14.14\%$. However, we adopt the result of the coupled mode theory technique, just as in [3], in order to compare more directly the CMT model of [3] with the FDTD and CMS procedures. Finally, we evaluate the formulas of the CMS model studied previously for the through-port transmission $\rho_o = \frac{b_o}{a_o} = |\rho_o| e^{i\Phi_o}$, and the drop port transmission $\tau_o = \frac{b_{oo}}{a_o} = |\tau_o| e^{i\Psi_o}$, in which Φ_o and Ψ_o represent the phase shift of the fields relative to the input field phase.

3.4.2 CMT circuit parameters

We now employ the RR circuit model of Figure 3.8, with f_j ,$1 \le j \le N$, representing the energy amplitude in ring j with $N = 4$. The quantity $\left|f_j(t)\right|^2$ is normalized to the energy stored in ring j. Further s_i and s_f represent the input fields while s_t and s_d represent the through and drop port transmitted fields respectively and are normalized such that the corresponding field powers are given by $\left|S_i(t)\right|^2$,$\left|S_f(t)\right|^2$, $\left|S_t(t)\right|^2$ and $\left|S_d(t)\right|^2$ respectively [3]. The resonant mode of the RR though is described by the energy amplitude f and total energy $\left|f(t)\right|^2$. The CMT coupling coefficients are μ_o , μ_{oo} and μ_j in place of the CMS coupling coefficients k_o , k_{oo} and k_j respectively. As above, we set $\mu_o = \mu_{oo}$ and $\mu_j = \mu \ \forall j$. The amount of power coupled out of a ring is parameterized by three decay rates τ_e , τ_d and τ_l where the first two represent the decay into the through and the drop ports respectively, while the third is the decay due to waveguide losses. The relations between the coupling coefficients in both models are given by [3], where $\mu_o = k_o\sqrt{v_g/(2\pi R)}$ and $\mu_j = k_j v_g/(2\pi R)$ with $v_g = c/n_g$ the group velocity, $\mu_o = \sqrt{2/\tau_e}$ and $\mu_{oo} = \sqrt{2/\tau_d}$ [3], and in the present case $\tau_e = \tau_d$. As in the CMS model, we examine the device transmission for a single input signal, so that $a_{oo} = 0$ and $s_f = 0$ in the CMS and CMT models respectively.

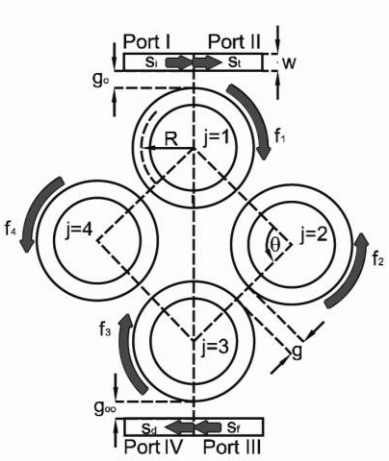

Figure 3.8: The CMT model of the compound ring resonator circuit.

While no relationship between α and τ_l is specified in [3], we can obtain this following the same procedure employed in [3] to relate μ_o , k_o and τ_e . Hence, for an isolated ring, the power decay results purely from waveguide losses. Consequently, in the CMT model, the power flowing in a lossy ring decays as e^{-2t/τ_l} , with $t = l/v_g$ for one turn while in the CMS model, the power decays as $e^{-\alpha l}$ for

one turn. Accordingly, $\tau_l = \frac{2}{\alpha v_g}$. Following the technique in [3], we have for the configuration of Figure 3.8

$$f = A_1^{-1} A_2 s \qquad \textbf{(3.12.a)}$$

$$f^T = [f_1 \; f_2 \; f_3 \; f_4] \qquad \textbf{(3.12.b)}$$

$$s = [s_i] \qquad \textbf{(3.12.c)}$$

$$A_1 = \begin{bmatrix} i\Delta\omega_1 + \frac{1}{\tau_e} + \frac{1}{\tau_l} & i\mu_1 & 0 & i\mu_4 \\ i\mu_1 & i\Delta\omega_2 + \frac{1}{\tau_l} & i\mu_2 & 0 \\ 0 & i\mu_2 & i\Delta\omega_3 + \frac{1}{\tau_d} + \frac{1}{\tau_l} & i\mu_3 \\ i\mu_4 & 0 & i\mu_3 & i\Delta\omega_4 + \frac{1}{\tau_l} \end{bmatrix} \qquad \textbf{(3.12.d)}$$

$$A_2^T = [-i\mu_o \; 0 \; 0 \; 0] \qquad \textbf{(3.12.e)}$$

in which $\Delta\omega_j = \omega - \omega_j$ with ω the input signal angular frequency, ω_j is the j^{th} ring resonance angular frequency given by $\omega_j = \frac{2m\pi c}{n_e l}$, with $m = 1,2,\ldots$ is the azimuthal resonance order, and c is velocity of light in free space. The through and drop port transmission is further $\rho_L = \frac{s_t}{s_i} = |\rho_L| e^{i\Phi_L}$ ($\tau_L = \frac{s_d}{s_i} = |\tau_L| e^{i\Psi_L}$) with:

$$s_t = s_i - i\mu_o f_1 \qquad \textbf{(3.13.a)}$$

$$s_d = s_f - i\mu_{oo} f_3 \qquad \textbf{(3.13.b)}$$

and Φ_L and Ψ_L represent the phase shifts of the fields relative to the input.

3.4.3 Numerical results

We now calculate the transmission according to the CMT model which is then compared to the results from the CMS and FDTD techniques for three representative ring waveguides. In our first calculation, we set the loss coefficient to zero, $\alpha = 0$ in the CMS model so that accordingly $1/\tau_l = 0$ in the CMT model. The transmission characteristics of the two ports in both models is then evaluated and plotted against the round trip phase shift, $\phi = \beta l$ with $l = 2\pi R$ in Figure 3.9. Next we consider the loss coefficients corresponding to 5% and 10% power loss per turn, representing different possible losses due to fabrication process tolerance in sidewall etching, oxide layer thickness or material intrinsic absorption, which yield the graphs of Figure 3.10 and Figure 3.11 respectively. The FDTD results are here fitted, for simplicity, to rational functions through equations (9) and (11) of [3] for the through and drop port transmission respectively.

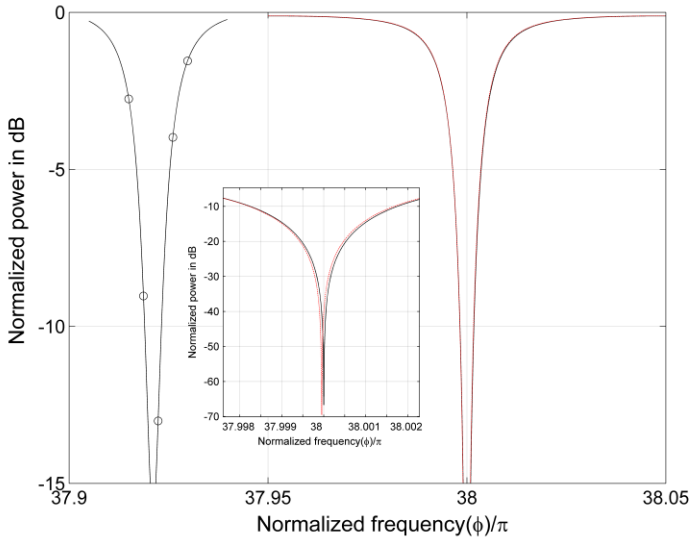

(a)

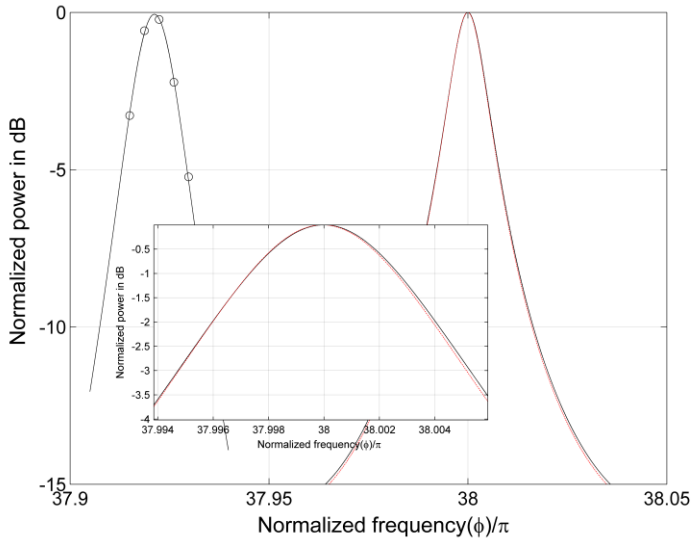

(b)

Figure 3.9: (a) The through port and (b) the drop port transmission characteristics for a lossless circuit, - - by the CMT model (red line), - by the CMS model and–o by the FDTD model. The small shift of results by the CMS and the CMT models is shown in the inset. The resonance wavelength corresponds to $m = 19$

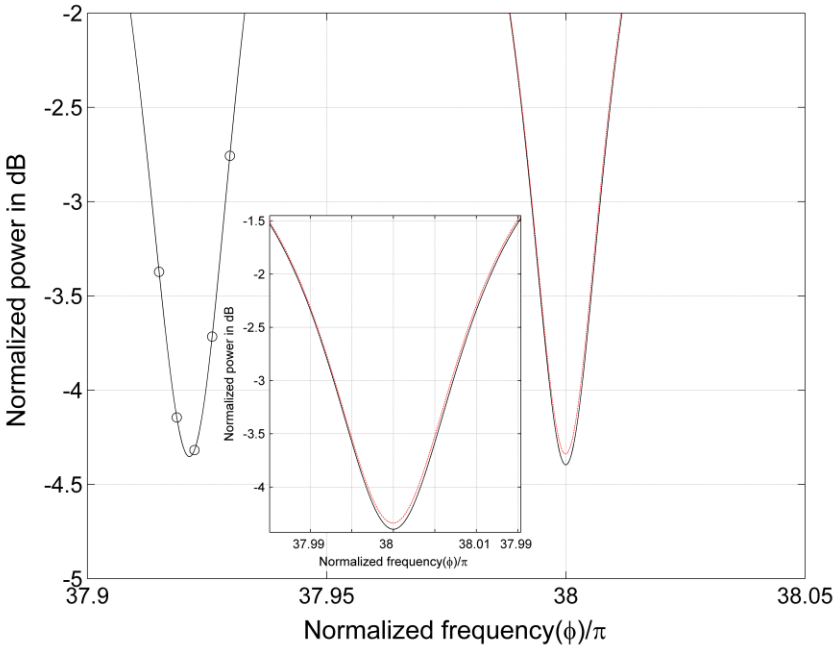

(a)

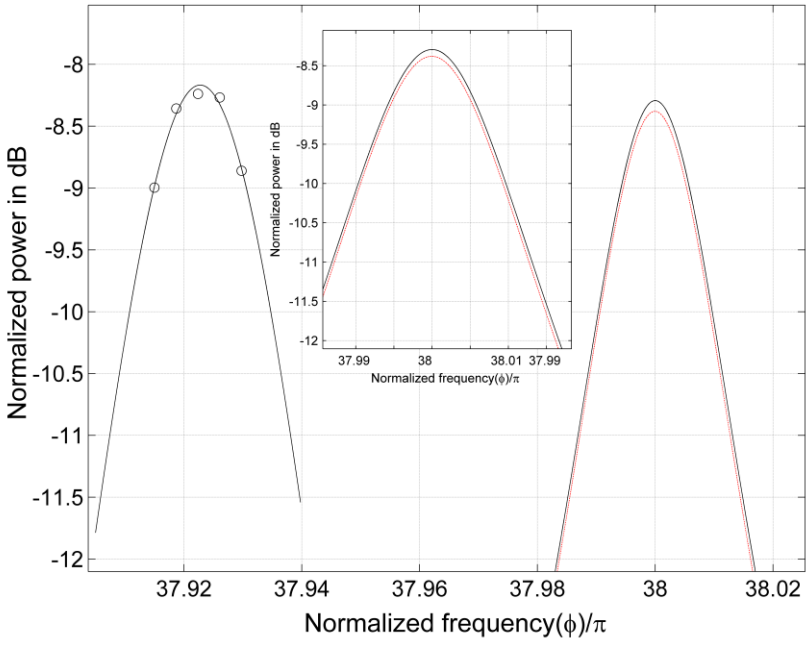

(b)

Figure 3.10: As in Figure (3.9) but for (a) The through port and (b) the drop port transmission characteristics for a circuit with 5% **power loss per round trip**

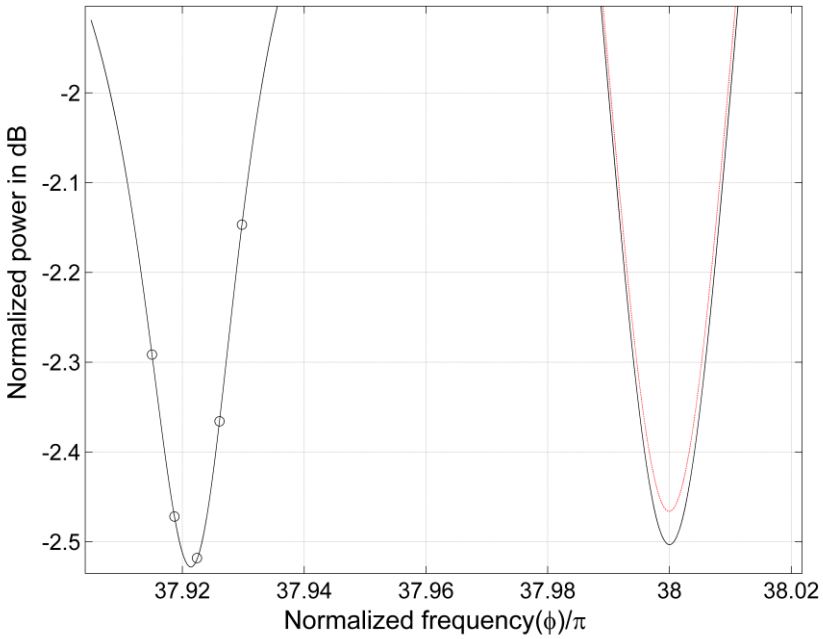

(a)

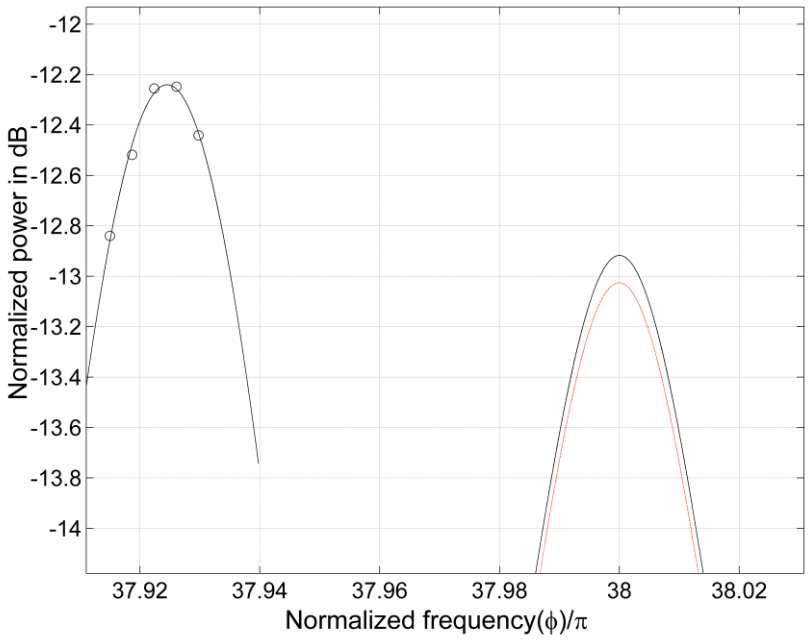

(b)

Figure 3.11: As in Figure 3.9 but for (a) The through port and (b) the drop port transmission characteristics for a circuit with 10% power loss per round trip.

In our FDTD simulations, the normalized mode of the slab waveguide is launched into the input port and the overlap between the output port power and the launch power is evaluated at the output. The time step is set to $0.007\,\mu m/c$ and the perfectly matched layer (PML) boundary conditions are employed. The grid size is varied in both the lateral direction (x) and the longitudinal direction (z) starting with $0.08\,\mu m$ down to $0.01\,\mu m$ when the values of power transmission over the range of wavelength of interest, i.e. around resonance, start to strongly saturate. The FDTD resonance wavelengths shown in Figure 3.9, Figure 3.10 and Figure 3.11 are shifted from those generated by the other techniques by less than $2\,nm$. This is primarily the result of the finite grid point spacing as we have found that the FDTD transmission curves approaches those of the other techniques as the interval between successive grid-points decreases. This tendency is evident for the three values of losses that we have examined. However, since the time required for a calculation for our two-dimensional square mesh implementation rapidly increases with the number of grid points, the CPU time even for our small ring radius of $R = 1.7\,\mu m$ reaches several days for the smallest grid point spacing of $0.01\mu m$. This effectively precludes the application of the FTDT method to structures which requires a ring resonator circumference of about $700 - 800\,\mu m$ to achieve the free spectral range of $FSR = 100\,GHz$ typically associated with WDM applications.

Otherwise, the bandwidth and the transmission peaks are in excellent agreement among the three techniques which therefore also verifies our relationships between the loss coefficients in the CMS and the CMT models.

Accordingly, we have analyzed a compound RR circuit based on the CMT technique and have compared our results to those of the CMS and FDTD methods for both lossless and lossy circuits. Here we observed that while the CMS yields a complicated analytic description of the problem, the accuracy of the FDTD, can however be insufficient for large RR circuits unless extensive computational resources are available. Additionally, while the CMT can be well-suited to ring resonator based circuit analysis as suggested in [3], the examples chosen in this reference of rings coupled in series or in parallel do not conclusively establish the relative advantages of the CMT since these structures can be modeled simply by multiplying the parametric matrices appearing in the CMS method. In contrast, our circuit includes an internal feedback path for power propagation that considerably complicates the formalism as detailed previously in this chapter. In our more involved example, the relative simplicity of the CMT analysis becomes far more evident since two sets of CMT equations replace 11 sets of CMS equations when the coupling and losses are small. We also examined the relationship between the loss coefficient of the CMT and CMS models. Finally, we obtained FDTD results that agree well with the CMS and CMT methods, and additionally demonstrated that the effects of radiation modes are negligible for our structure.

Note that we have employed the circuit parameters in [3] in order to facilitate our comparison between the CMS, CMT and FDTD techniques for the compound RR circuit configuration since for these parameters the coupling and losses are sufficiently small that the CMT is applicable. However, the CMT method cannot analyze the compound RR based interleaver circuit that we investigated above with the CMS method, since the coupling coefficients are too large.

In the following section we discuss the design, fabrication and characterization of a interleaver circuit that implements our CMS method results.

3.5 Design, fabrication and characterization

To satisfy the WDM interleaver/deinterleaver specifications of section 3.2 we apply the following design steps. First, the free spectral range $FSR = 100GHz$ and hence the ring circumference, l, is found from:

$$FSR = \frac{c}{n_g l}(Hz) \equiv -\frac{\lambda_o^{\,2}}{n_g l}(m) \qquad \textbf{(3.14)}$$

where $c = 3\times10^8\ m/s$ is the speed of light in space, $n_g = n_e - \lambda_o \frac{dn_e}{d\lambda_o}$, is the mode group RI and n_e is the mode effective RI. To avoid multimode broadening, single-mode silicon over insulator (SOI) waveguide, with the cross section shown in Figure 3.12 and parameters of Table 3.2 is employed. Through a beam propagation method (BPM) simulation [73] we find, neglecting material dispersion, that the TE-like mode, with the dominant electric field component parallel to the substrate, has $n_e = 2.431056$, $n_g = 3.98$, $\frac{dn_e}{d\lambda_o} \approx -1\times10^6\ /m$ at $\lambda_o = 1550\ nm$ and thus $l = 755\ \mu m$ for the required FSR. The device is then on-resonance at $\lambda_o = 1550.13\ nm$, with $n_e = 2.43092$ and resonance order $m = 1184$ while the waveguide power loss is $2.4\ dB/cm$ [31-32], with negligible

bending losses as $R > 5\,\mu m$ [32]. The $2\,\mu m$ thick silica layer suppresses power leakage to the substrate leading to an overall power loss per cycle of $2.4 \times 0.0755 = 0.18\,dB$ or 4% per cycle. Additional losses in real devices as a result of imperfections can then further increase losses up to the permitted 10% per cycle [43].

To simplify the coupling ratio calculations we replaced the circular ring with a straight-sided racetrack and employed our BPM simulator to determine the coupling coefficient, κ, between two straight waveguides separated by a gap, g, by first determining the required coupling length Λ as detailed before in Chapter 1.

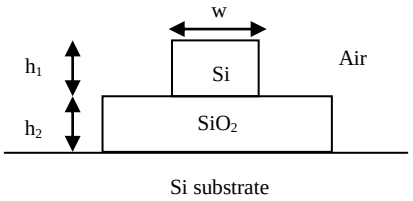

Figure 3.12: The single-mode SOI waveguide cross-section.

Parameter	Value
Silicon RI (n_{Si})	3.474[29]
Silica RI (n_{Silica})	1.444[29]
Air RI (n_a)	1
w	$0.5\mu m$
h_1	$0.22\mu m$
h_2	$2\mu m$

Table 3.2: Single mode SOI waveguide parameters.

The racetrack dimensions are determined by first considering the mutually coupled racetracks of Figure 3.13. If L_1, L_2 represent the length of the straight sides and R is the corner radius, section 3.2 sets the shortest path on the racetrack between the interaction regions with neighboring racetracks equal to 25% of the racetrack circumference yielding the design rules:

$$L = 2\pi R + 2L_1 + 2L_2 = 755\,\mu m \qquad \textbf{(3.15.a)}$$

$$L_1 = 2R + s + 2l_2 \qquad \textbf{(3.15.b)}$$

$$L_2 + l_2 + \pi R = \frac{L}{4} \qquad \textbf{(3.15.c)}$$

$$k_o = k_{oo} = \sin(\kappa l_1) \quad \textbf{(3.15.d)}$$

$$k = \sin(\kappa l_2) \quad \textbf{(3.15.e)}$$

where l_1, l_2 and s are the racetrack-bus and racetrack-racetrack interaction lengths and the separation between the two side racetracks, c.f. Figure 3.13. For the additional racetrack at port IV, the circumference should satisfy $L = 755\,\mu m$ yielding an interaction length with the bus l_a given by :

$$k_a = \sin(\kappa l_a) \quad \textbf{(3.15.f)}$$

The shape of the additional stage is therefore dependent on the available area on the chip. Table 3.3 displays the racetrack dimensions that satisfy the conditions $g = g_o = g_{oo}$ with $g = 0.2\,\mu m, 0.3\,\mu m$ and $0.4\,\mu m$, where we have set $L_2 = 0$ to decrease the mode mismatch loss in the transition between the bent and straight waveguides and also to decrease the circuit area.

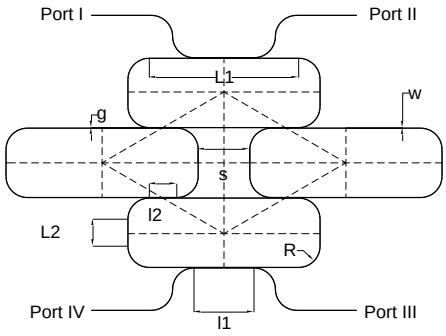

Figure 3.13: A schematic of the proposed circuit with rings replaced with racetracks.

g	$\Lambda = \frac{\pi}{2\kappa}$	l_1	l_2	L_1	s	R	l_a
0.2	47.74	36.9	16.8	205.55	62.48	54.73	38.38
0.3	120.78	92.9	42.5	231.25	53.14	46.55	96.86
0.4	293.29	225.5	103.2	291.95	31.08	27.23	235.2

Table 3.3: Dimensions of the racetracks in μm with $L_2 = 0$

The layout was designed using Design Workshop 2000 [74]. The devices were fabricated with $193nm$ photolithography by ePIXfab at IMEC. Integrated grating couplers were employed to couple light into and out of the TE waveguide mode.

In the setup shown in Figure 3.14 , light from a tunable laser power is launched into a polarization maintaining fiber tilted by 10^o with respect to the vertical. The grating coupler is connected to the input port of the deinterleaver under test through a tapered waveguide. A similar arrangement, with a regular fiber though, couples power out of the through and the drop ports of the device.

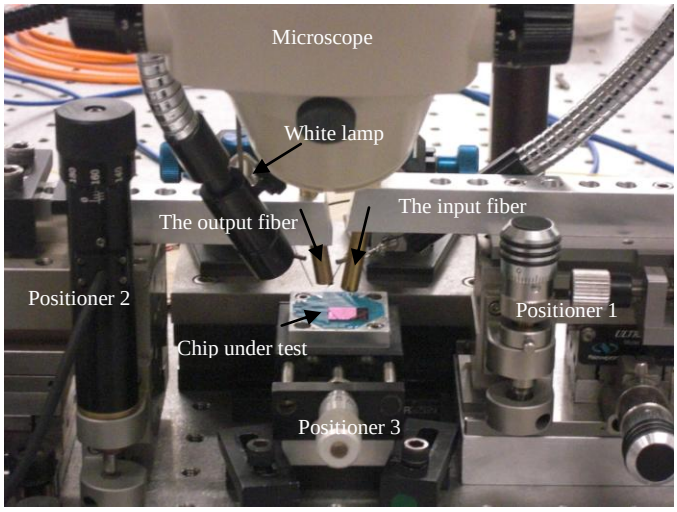

Figure 3.14: The characterization setup with different parts labeled. Positioner (1) holds the input fiber; while positioner (2) holds the output fiber and positioner (3) holds the chip under test.

After aligning the input and output fibers, the laser wavelength is swept over a range of a few nanometers around $\lambda_o = 1550\,nm$ with a $0.01nm$ step, and the transmission power is recorded using a detector connected to a PC. The power transmission is normalized with respect to its peak value and plotted as a function of wavelength for each device.

Two copies of each circuit as in the layout shown in Figure 3.15, all with theoretically equivalent performance, were copied onto 6 different positions on the wafer each with a different exposure. The positions are indicated by a row number: -4,-2,-1,0,+2,+4, with +4, 0, -4 being the positions with the maximum, ideal (corresponding to $w = 500nm$) and minimum exposure level respectively. Therefore, there are 36 devices to test. SEM pictures of three of the fabricated devices are presented in Figure 3.16. A photograph of some of the fabricated devices is shown in Figure 3.17. Measurement results for the two devices with best performance, labeled as device (A) and device (B), are reported here and displayed in (d)

Figure 3.18. Device (A) is device number (4) with exposure degree (-2) while Device (B) is device number (6) with exposure degree (0).

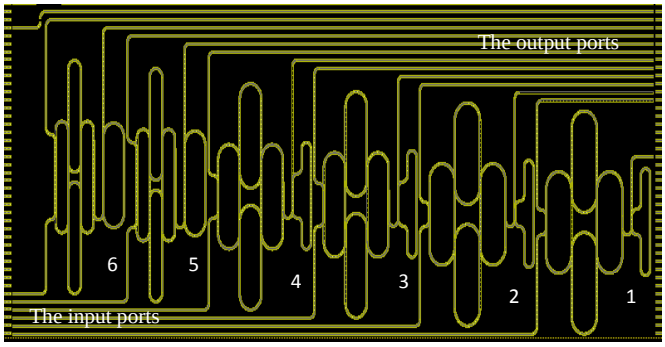

(a)

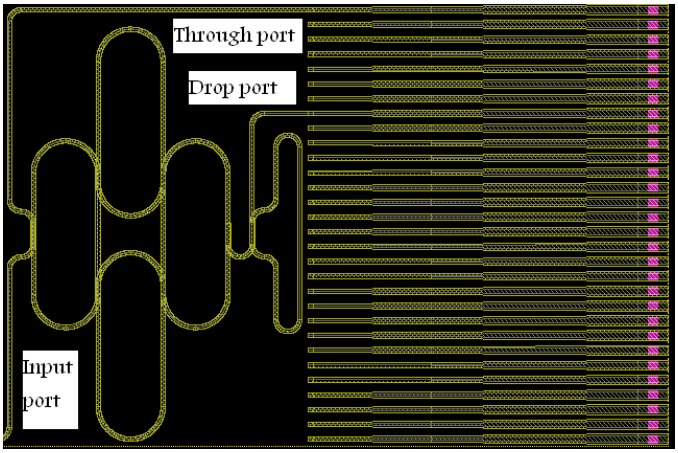

(b)

Figure 3.15: (a) the layout of the six copies of the proposed circuit in section 3.2. The two devices on the right most (1, 2), two in the middle (3, 4) and two on the left most (5, 6) of the chip correspond to the dimensions on the 1st, 2nd and 3rd entries in Table 3.3 respectively, (b) the layout of device (1) showing the input, through and drop ports. On the right is the tapered waveguides followed by the grating couplers.

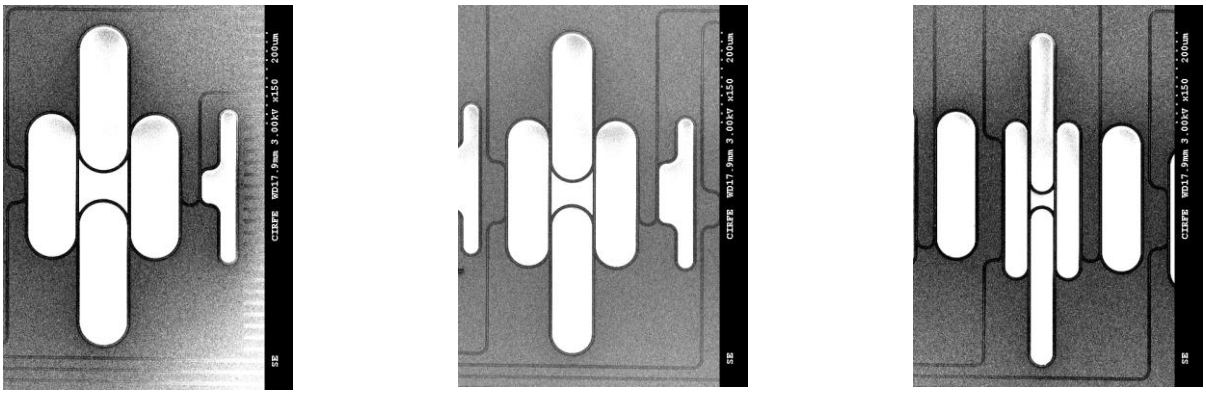

Figure 3.16: SEM pictures for the fabricated (a) device (1) with $g = 0.2\mu m$, (b) device (3) with $g = 0.3\mu m$ and (c) device (5) with $g = 0.4\mu m$

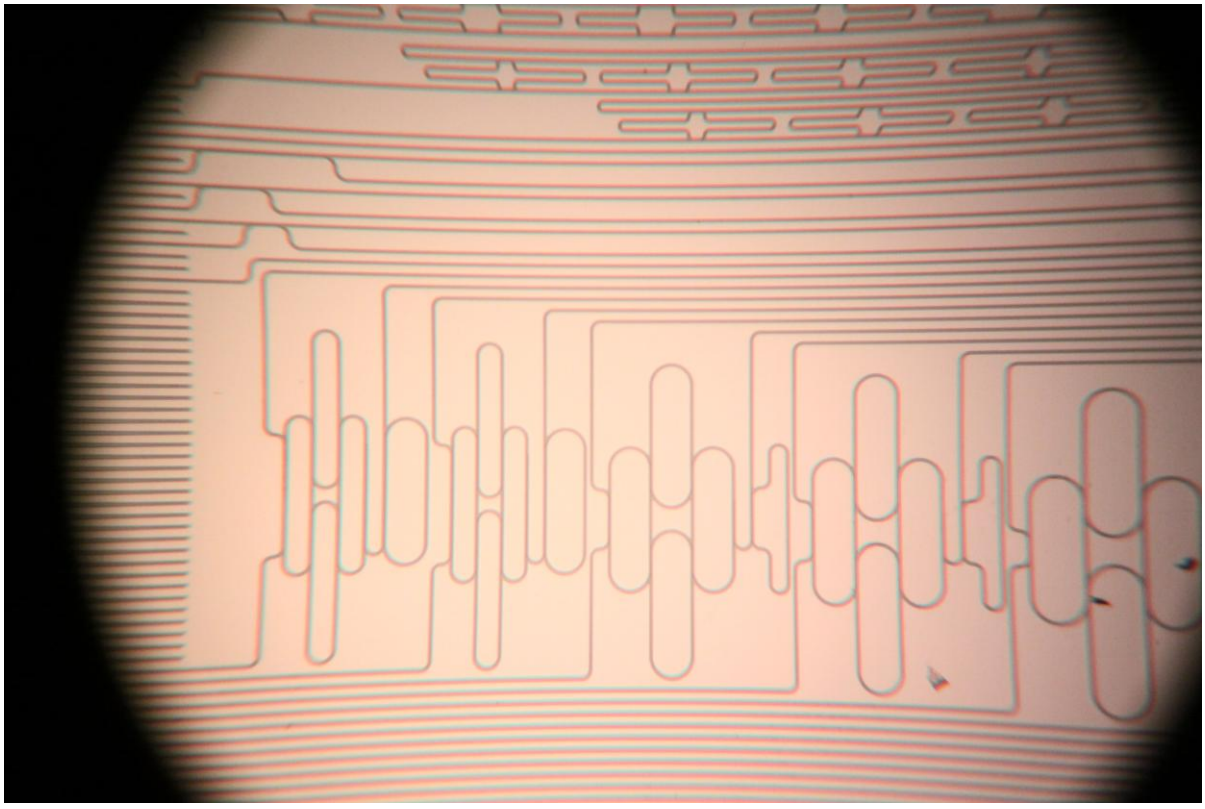

Figure 3.17: An optical photo for some the fabricated circuits.

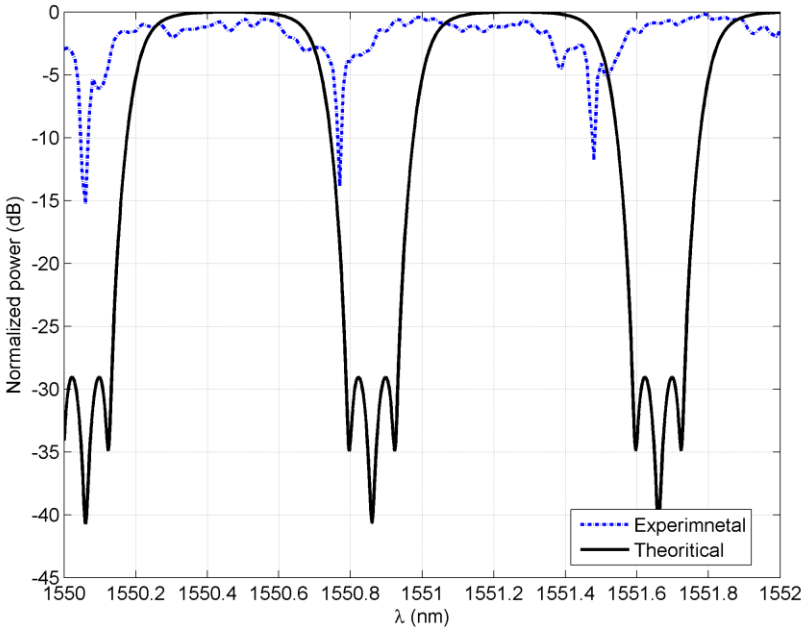
Normalized power (dB)
λ (nm)
Experimnetal
Theoritical

(a)

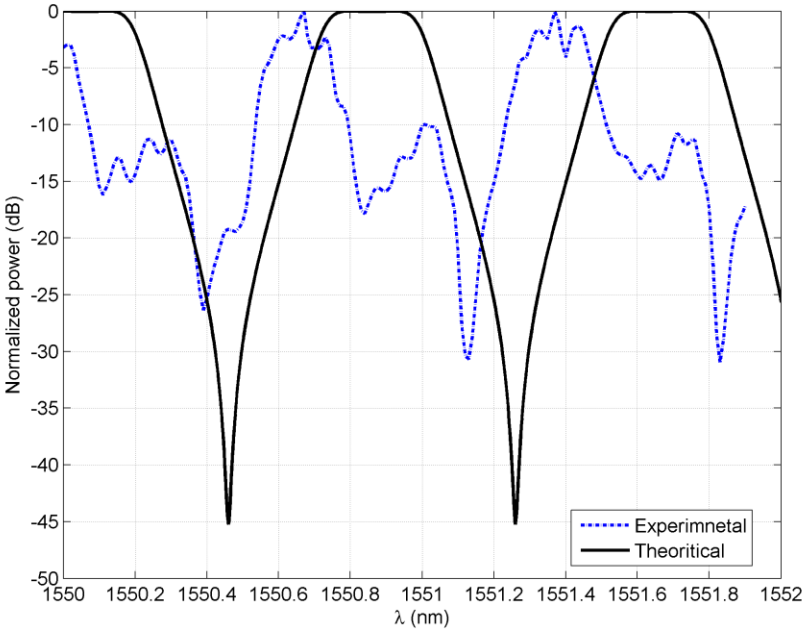
Normalized power (dB)
λ (nm)
Experimnetal
Theoritical

(b)

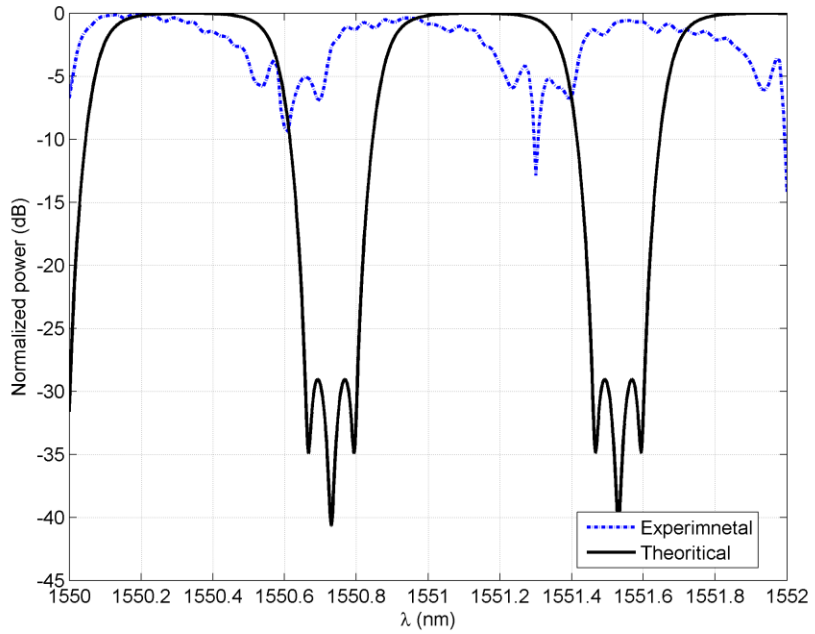

(c)

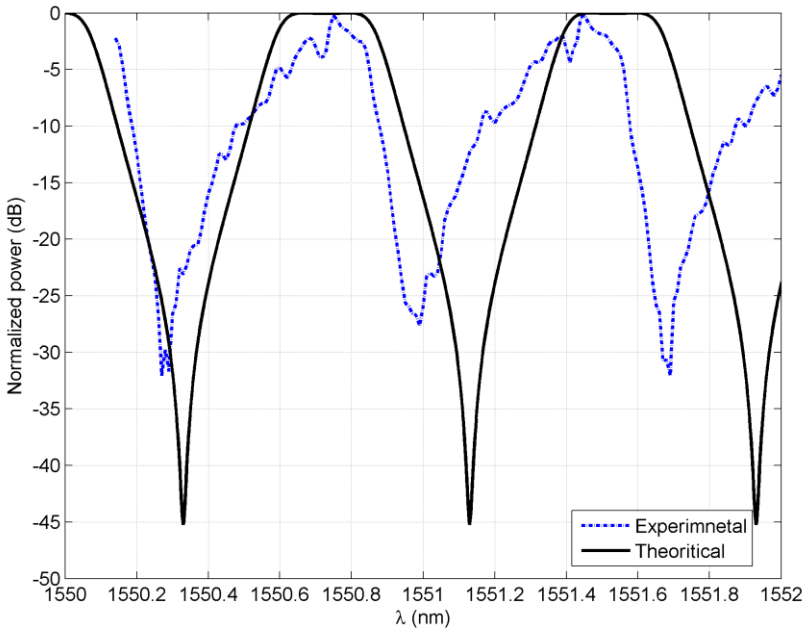

(d)

Figure 3.18: Measured and theoretical transmission characteristics of (a) the though port of device (A), (b) the drop port of device (A), (c) the through port of device (B) and (d) the drop port of device (B).

3.6 Post fabrication study

The measured free spectral range for these devices is $FSR \approx 0.7\,nm$, as opposed to the theoretically calculated $FSR = 0.8nm$, indicating that the actual group refractive index is $n_g \approx 4.5$ not $n_g = 4$. Consequently for a $FSR = 0.8\,nm$ the optimum racetrack circumference should have been $L \approx 670\,\mu m$ instead of $L \approx 755\mu m$. The resonance wavelength was additionally shifted from the theoretically calculated $\lambda_o = 1550.13\,nm \pm FSR$. Hence we have shifted the theoretical transmission curves to best match the experimental transmission curves as indicated in Figure 3.19.

The deviations from the theoretical expectations also include ripples in the transmission band that probably result from slight differences in the dimensions of the five racetracks in each device which lead to small resonance shifts. The steep roll off of the curves near the transmission minima requires a more accurate scanning step than $0.01nm$ to display the theoretically predicted minimum values. However the general features of the transmission bandwidth and roll off agree with the theoretical curves.

The apparent deviations from the theoretical expectations may come as a result of the fabrication tolerance of the waveguide and the gap dimensions as well as the theoretical assumptions that we followed to simplify the calculations [75], [76-79]. In a previous study [75], a ring resonator circuit based on identical waveguide dimensions, i.e. $w \times h_1 = 500\ nm \times 220\ nm$, was fabricated using the same technology but the actual waveguide width was found to be $w = 420nm$ instead of the desired $w = 500\,nm$. Through BPM simulations, we find that such a fabrication dimensional error of $80\,nm$ results in a change of n_g by 0.2 and of the power coupling coefficient by 0.4. Similarly, changing w by $1nm$ shifts the transmission spectrum by a wavelength of $0.96\,nm$, or equivalently $76\,GHz$. Moreover, as in [75] the waveguide walls might be slanted with an angle up to 9^o and finally, we have neglected the coupling to the round portions of the racetracks. A detailed study on the effect of fabrication tolerance on the phase disorder and the coupling disorder in ring resonator circuits is given in [79].

Accordingly, we introduced fabrication tolerance into our simulations by first adding a random, uniformly distributed error within $[-0.1,0.1]$ to the field coupling coefficients, while restricting the coupling to values <1, then employing the experimental value, $0.7\,nm$ of the FSR in place of $0.8\,nm$, or equivalently $n_g = 4.5$ instead of $n_g = 4$, and finally shifting the transmission spectra for best matching between theoretical and experimental curves. The corresponding simulation results for these devices are given in Figure 3.19 , demonstrating a far better agreement between the numerical and the experimental results. The coupling ratios are here: $k_o = k_{oo} = 0.97$, $k_a = 0.95$, for both devices, while $k_1 = 0.43$, $k_2 = 0.57$, $k_3 = 0.49$ and $k_4 = 0.44$ for Device (A) and $k_1 = 0.425$, $k_2 = 0.6$, $k_3 = 0.49$ and $k_4 = 0.47$ for Device (B), where k_1, k_2, k_3 and k_4 are respectively the field coupling coefficients across the top-right, bottom-right, bottom-left and top-left gaps in Figure 3.13.

Noting that the field coupling ratios in the original design were: $k_0 = k_{oo} = 0.935$, $k_a = 0.952$ and $k = k_1 = k_2 = k_3 = k_4 = 0.525$, we conclude that small coupling coefficient changes can strongly affect the device performance, which more generally presents a serious challenge in fabricating complex devices such as the interleaver. However, more careful subsequent fabrication runs could presumably yield improved devices.

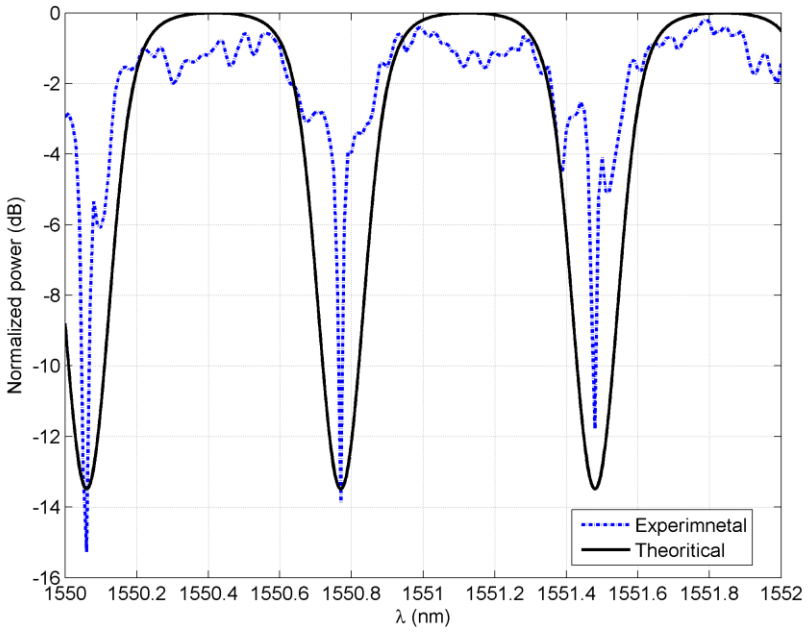

(a)

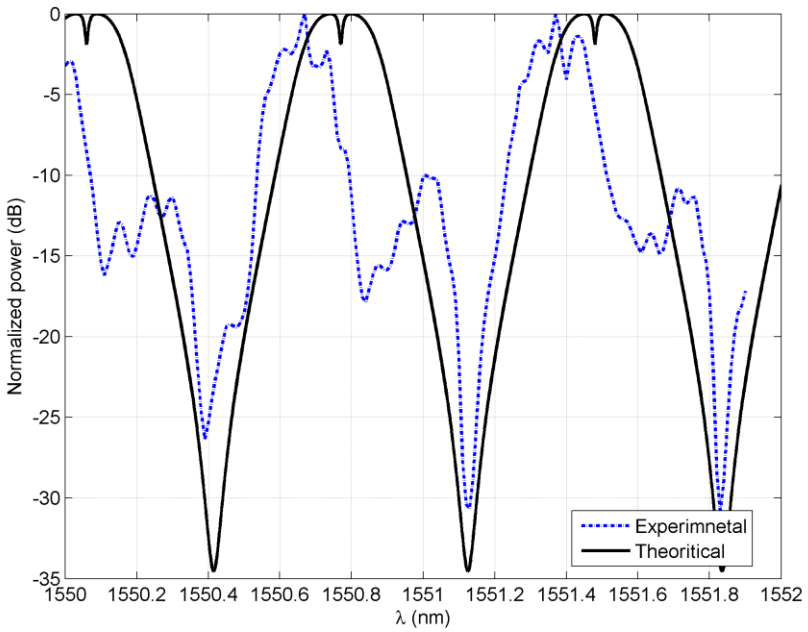

(b)

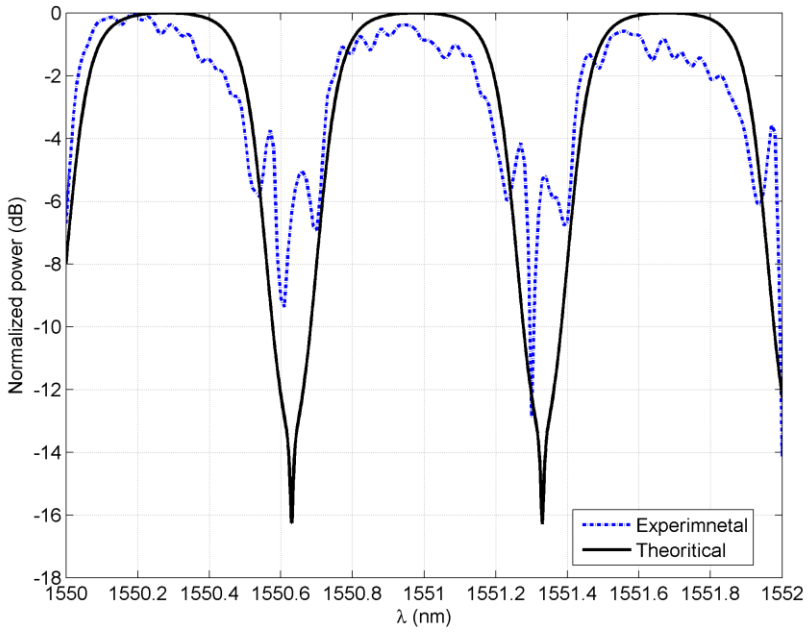

(c)

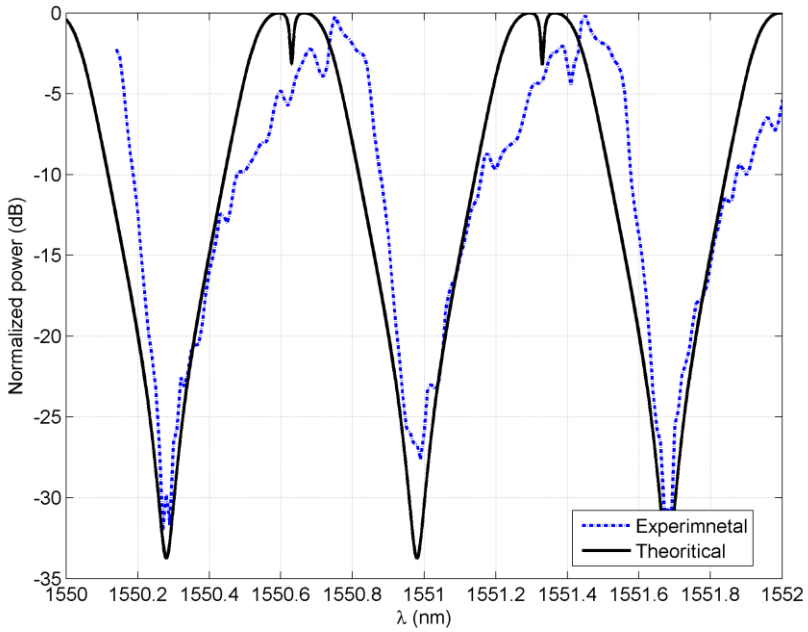

(d)

Figure 3.19: Measured and theoretical transmission characteristics as in Figure 3.18 but with modified field coupling coefficients.

3.7 Conclusion

In this chapter we studied in detail our "compound ring resonator circuit". We customized the design for WDM interleaver/deinterleaver applications, generating a layout with simpler design rules, smaller area and competitive performance compared to other circuits of the same nature. This circuit was then employed to benchmark the CMS, CMT and FDTD modeling techniques. Despite the generality of the CMS procedure and the accuracy of the FDTD, the CMT model yields rapid and accurate results for small coupling and small losses. We then designed, fabricated and characterized an interleaver/deinterleaver circuit for WDM operation. Many copies of the circuit were fabricated with different waveguide separation gaps and bending radii to establish the fabrication tolerance. Our experimental measurements are in qualitative agreement with theoretical predictions for the circuit performance. Deviations between the two sets of results resulting from fabrication errors could presumably be largely eliminated through multiple design-test cycles that would clearly establish optical properties such as the effective indices and losses of the waveguides and couplers and identify the optimal design parameters that would compensate, for example, lithography proximity effects.

Chapter 4

High sensitivity ring resonator Gyroscopes

In the previous chapter we analyzed the compound ring resonator circuit which is simply a closed loop of rings (CLR), and introduced a design that matches the requirements of a standard WDM interleaver/ deinterleaver circuit. Next we customize the same structure for a waveguide gyroscope that detects rotational motion through the "Sagnac Effect" [80]. Here we first outline rotational motion detection with ring waveguides and then overview previous mathematical techniques for investigating ring gyroscopes including the fiber optic gyroscope (FOG), the resonant FOG (RFOG), and the coupled resonant optical waveguide (CROW) gyroscope. Finally, we analyze our CLR gyro and compare our results to previously published CROW and FOG results.

4.1 Overview

Rotational motion can be detected by launching two counter propagating waves into a rotating loop waveguide through the Sagnac effect as the rotational contribution to the phase accumulated by the two waves is equal and opposite [80]. Consequently, the interference signal generated by mixing the two waves at the output is a function of the rotational motion. While ring resonator circuits have been proposed for rotational motion detection [81], the authors of [7] demonstrate that a conventional FOG with the same footprint and transmission losses is still more sensitive to rotational motion than the corresponding CROW structure, where the sensitivity is defined as the rate of variation of the circuit output power with rotational speed. However, a standard FOG requires long fiber lengths.

In this work, we provide a comparison of CROW and FOG gyroscopes to the CLR structure discussed below by varying the wavelength, coupling coefficients, waveguide losses, number of rings and ring radius. We find that the performance of the CLR device exceeds that of the other structures; however, the optimal structure corresponds to the one in which the field circles around the rings of the device with maximum coupling between rings. This corresponds effectively to a single ring, and indeed, we subsequently demonstrate that a simple ring structure yields improved performance. Thus, the approach in this work provides an alternate method to establish that a single loop resonant gyro displays greater sensitivity to rotation than other proposed structures of the same area, as already noted in [8].

4.2 Circuit analysis

4.2.1 Sagnac effect

Consider a ring resonator with a mean radius R rotating at an angular velocity $\vec{\Omega}$ with a center located at a distance R_o from the center of rotation as shown in Figure 4.1.a. If an electric field propagates through the ring from a position at angle θ_1 with the horizontal to a position at angle θ_2, the ratio of the electric field at the latter and former locations is $e^{-i\delta\frac{|\theta_2-\theta_1|}{2\pi}+i\varphi_s}$ where $\delta = \phi - i\frac{\alpha}{2}l$,

$\phi = \beta l$ is the round trip phase shift, $l = 2\pi R$, $\beta = \frac{2\pi}{\lambda_o} n_e$ is the field propagation constant, n_e is the field effective index, λ_o is the free space wavelength, α is the power loss coefficient in m^{-1} and the Sagnac phase shift induced by the rotational motion [80-81] is $\varphi_s = \int_{\theta_1}^{\theta_2} d\varphi_s$, with $d\varphi_s = \frac{\omega}{c^2}\vec{V}.d\vec{r}$ where $\vec{V} = \vec{\Omega} \times (\vec{R} + \vec{R}_o)$ is the linear velocity of the segment $d\vec{r}$. Here c is the vacuum speed of light and $\omega = \frac{2\pi c}{\lambda_o}$ is the angular frequency of the field. From Figure 4.1.a, $\varphi_s = \varphi_\Omega(\theta_2 - \theta_1) + \varphi_v(\sin(\theta_1 - \theta_o) - \sin(\theta_2 - \theta_o))$, with $\varphi_\Omega = \frac{\omega\Omega}{c^2} R^2 = \frac{R}{R_o}\varphi_V$. The first term $\varphi_\Omega(\theta_2 - \theta_1)$ is associated with the phase shift due to the rotational motion if the ring is centered at the center of rotation, i.e. $R_o = 0$, while $\varphi_v(\sin(\theta_1 - \theta_o) - \sin(\theta_2 - \theta_o))$ is the additional phase shift due to the shift between the ring center and the center of rotation.

In the following we assume a clockwise rotation direction and denote the input field and power by a_o and p_o while the fields and powers at the output ports A and B are denoted by a_A, p_A and a_B, p_B respectively. We assume further that the rings of all gyroscopes are on-resonance as in [7] to maximize the sensitivity to rotational motion, which implies that $\beta l = 2m\pi$, with m an integer, where we employ the convention that for a forward travelling wave both phase terms are negative for the case of Figure 4.1.a, when the field travels in the clockwise direction of rotation, so that $d\vec{r}.\vec{V} > 0$ for $\theta_2 < \theta < \theta_1$. If the wave travels opposite the direction of rotation, $\theta_2 > \theta_1$ and the term $\varphi_\Omega(\theta_2 - \theta_1)$ is positive, while if the field propagates such that $d\vec{r}.\vec{V} < 0$, the term $\varphi_v(\sin(\theta_1 - \theta_o) - \sin(\theta_2 - \theta_o))$ is positive.

For an FOG, as shown in Figure 4.1.b, with number of turns N_f, loop radius R_f and total length $l_f = 2\pi R_f N_f$ the normalized field transmission of the two ports can be easily proven to be $\tau_{fA} = \frac{a_A}{a_o} = \frac{-i}{2}(\tau_{fI} + \tau_{fII})$ and $\tau_{fB} = \frac{a_B}{a_o} = \frac{1}{2}(\tau_{fI} - \tau_{fII})$, where $\tau_{fI} = e^{-\alpha l_f/2 - i\beta l_f - i2\pi N_f \varphi_\Omega}$ and $\tau_{fII} = e^{-\alpha l_f/2 - i\beta l_f + i2\pi N_f \varphi_\Omega}$.

For a single ring with radius R_s between the two arms of a Mach-Zender centered at rotation axis, c.f. Figure 4.1.c, the normalized transmitted field through is then $\rho_s = \frac{a_B}{a_o} = \frac{1}{2}(\rho_{sI} + \rho_{sII})$, with $\rho_{sI} = \frac{r_o - r_{oo} e^{-\alpha l_s/2 - i\beta l_s - i2\pi\varphi_\Omega}}{1 - r_o r_{oo} e^{-\alpha l_s/2 - i\beta l_s - i2\pi\varphi_\Omega}}$, $\rho_{sII} = \frac{r_o - r_{oo} e^{-\alpha l_s/2 - i\beta l_s + i2\pi\varphi_\Omega}}{1 - r_o r_{oo} e^{-\alpha l_s/2 - i\beta l_s + i2\pi\varphi_\Omega}}$, $l_s = 2\pi R_s$, $k_o^2 + r_o^2 = 1$, $k_{oo}^2 + r_{oo}^2 = 1$ where k_o (k_{oo}) is the field ratio coupled between the ring and the upper (lower) bus.

The normalized field drop transmission is similarly $\tau_s = \frac{a_A}{a_o} = \frac{1}{2}(\tau_{sI} + \tau_{sII})$ with $\tau_{sI} = \frac{-k_o k_{oo}\sqrt{e^{-\alpha l_s/2 - i\beta l_s - i2\pi\rho_\Omega}}}{1 - r_o r_{oo} e^{-\alpha l_s/2 - i\beta l_s - i2\pi\rho_\Omega}}$ and $\tau_{sII} = \frac{-k_o k_{oo}\sqrt{e^{-\alpha l_s/2 - i\beta l_s + i2\pi\rho_\Omega}}}{1 - r_o r_{oo} e^{-\alpha l_s/2 - i\beta l_s + i2\pi\rho_\Omega}}$.

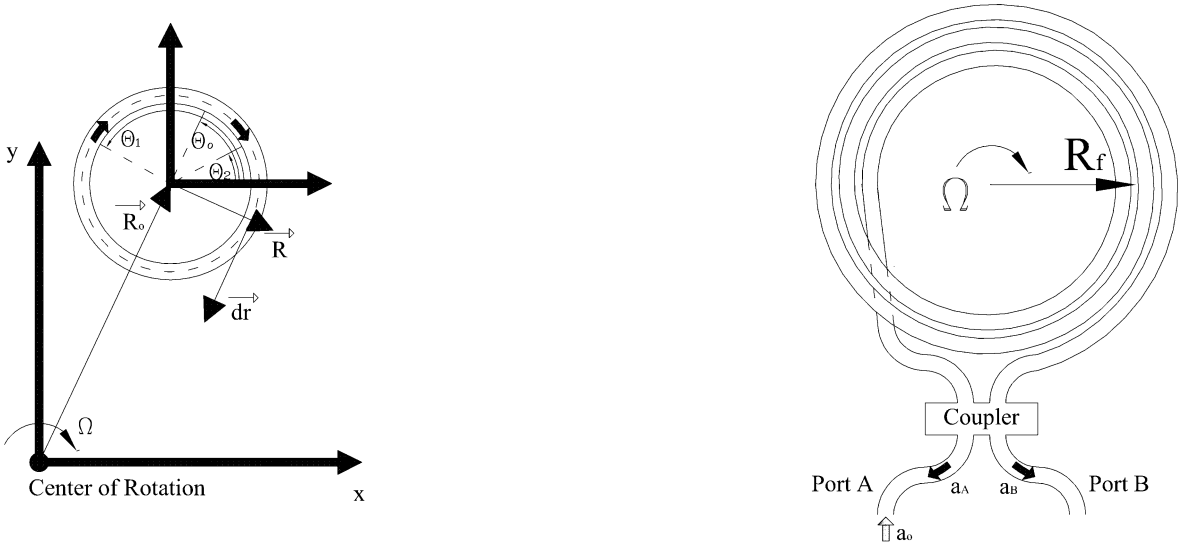

(a) (b)

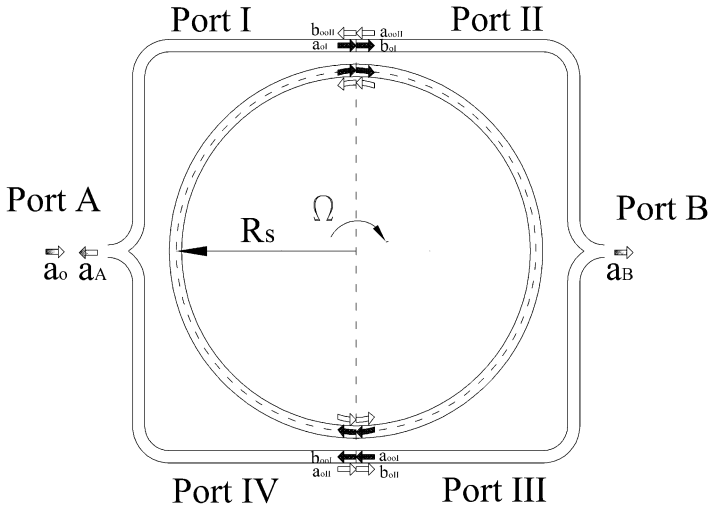

(c)

Figure 4.1: (a) A ring rotating about a center of rotation at a distance R_o from its center, (b) a fiber optic gyroscope (FOG) and (c) a single ring gyroscope.

4.2.2 Crow gyroscope

The coupled resonator optical waveguide (CROW) gyroscope proposed in [81] and [7] consists of a closed loop with an odd number, N [7], of cascaded rings coupled in series and fed through $3dB$ couplers as in Figure 4.2. The ratio of the field coupled between the leftmost (rightmost) rings and the neighboring buses is denoted by k_o (k_{oo}), while that between two neighboring rings is denoted by k. Note that in [81] the definition of the field coupling ratio is the square root of the power coupling coefficient κ. We then define the coupling matrices, $Q_o = \frac{1}{ik_o}\begin{bmatrix} r_o & -1 \\ 1 & -r_o \end{bmatrix}, Q_{oo} = \frac{1}{ik_{oo}}\begin{bmatrix} r_{oo} & -1 \\ 1 & -r_{oo} \end{bmatrix}$, $Q = \frac{1}{ik}\begin{bmatrix} r & -1 \\ 1 & -r \end{bmatrix}$ and the phase matrices: $P_1 = \begin{bmatrix} 0 & p_1 \\ p_2^{-1} & 0 \end{bmatrix}$, $P_2 = \begin{bmatrix} 0 & p_4 \\ p_3^{-1} & 0 \end{bmatrix}$, $P_3 = \begin{bmatrix} 0 & p_3 \\ p_4^{-1} & 0 \end{bmatrix}$, $P_4 = \begin{bmatrix} 0 & p_2 \\ p_1^{-1} & 0 \end{bmatrix}$. where $k^2 + r^2 = 1$, $p_1 = e^{-i\delta_2 - i\varphi_\Omega(2\pi-\theta) - i2\varphi_V \sin(\theta/2)}$, $p_2 = e^{-i\delta_1 - i\varphi_\Omega\theta + i2\varphi_V \sin(\theta/2)}$, $p_3 = e^{-i\delta_2 + i\varphi_\Omega(2\pi-\theta) + i2\varphi_V \sin(\theta/2)}$, $p_4 = e^{-i\delta_1 + i\varphi_\Omega\theta - i2\varphi_V \sin(\theta/2)}$, $\delta_1 = \delta \times \frac{\theta}{2\pi}, \delta_2 = \delta \times (1 - \frac{\theta}{2\pi})$ and $\theta = \frac{N}{N+2}\pi$ for a uniform polygon the vertices of which are the centers of the rings as shown in Figure 4.2 . Then $\begin{bmatrix} a_{ooI} \\ b_{ooI} \end{bmatrix} = T_1 \begin{bmatrix} a_{oI} \\ b_{oI} \end{bmatrix}$ and $\begin{bmatrix} a_{ooII} \\ b_{ooII} \end{bmatrix} = T_2 \begin{bmatrix} a_{oII} \\ b_{oII} \end{bmatrix}$, with a_{oI} and a_{oII} as defined in Figure 4.2 producing two output field components, the through b_{oI} (b_{oII}) and the drop b_{ooI} (b_{ooII}), while $a_{ooI} = a_{ooII} = 0$. Then, we have $T_1 = Q_{oo}P_1Q(P_2QP_1Q)^{\frac{N-1}{2}}Q^{-1}Q_o$ and $T_2 = Q_oP_3Q(P_4QP_3Q)^{\frac{N-1}{2}}Q^{-1}Q_{oo}$. Hence it is easy to prove that $\tau_{cI} = \frac{b_{ooI}}{a_{oI}} = \frac{-\Delta T_1}{T_1(1,2)}$ and $\tau_{cII} = \frac{b_{ooII}}{a_{oII}} = \frac{-\Delta T_2}{T_2(1,2)}$ are the field drop-port transmission coefficients, while $\rho_{cI} = \frac{b_{oI}}{a_{oI}} = \frac{-T_1(1,1)}{T_1(1,2)}$ and $\rho_{cII} = \frac{b_{oII}}{a_{oII}} = \frac{-T_2(1,1)}{T_2(1,2)}$ are the field through-port transmission coefficients. Finally, the normalized field transmission at the two output ports A and B are given by $\tau_{cA} = \frac{a_A}{a_o} = \frac{-i}{2}(\tau_{cI} + \tau_{cII})$ and $\tau_{cB} = \frac{a_B}{a_o} = \frac{1}{2}(\tau_{cI} - \tau_{cII})$ respectively.

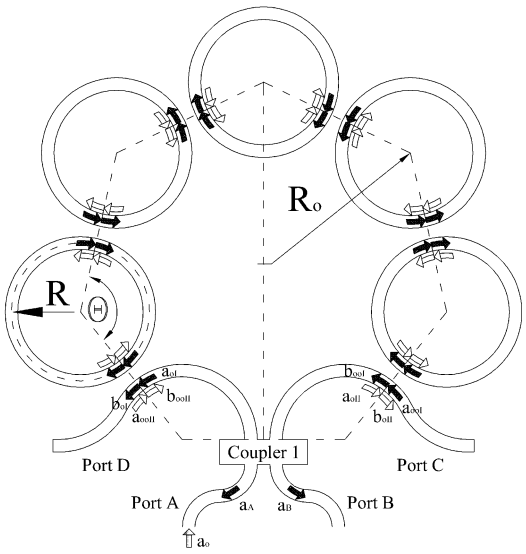

Figure 4.2: CROW gyroscope with $N = 5$

4.2.3 Loop of ring gyroscope

A CROW gyroscope contains a complete circle of waveguide rings terminated by a $3dB$ coupler. Therefore, the field can propagate multiple times through each ring accumulating additional Sagnac phase shift in the case of weak coupling between rings. If the $3dB$ coupler is replaced by an additional ring we therefore arrive at the CLR gyroscope in which the field can propagate multiple times around the entire structure, accumulating an additional Sagnac shift.

We accordingly consider an even number of rings; N coupled around a circle, as shown in Figure 4.3. The coupling between the top (bottom) ring and the neighboring bus is represented by Q_o (Q_{oo}) and the coupling between two neighboring rings is Q. The phase matrices are $P_5 = \begin{bmatrix} 0 & p_5 \\ p_6^{-1} & 0 \end{bmatrix}$ and $P_6 = \begin{bmatrix} 0 & p_8 \\ p_7^{-1} & 0 \end{bmatrix}$, with $p_5 = e^{-i\delta_1 + i\varphi_\Omega \theta - i2\varphi_V \sin(\theta/2)}$, $p_6 = e^{-i\delta_2 + i\varphi_\Omega (2\pi - \theta) + i2\varphi_V \sin(\theta/2)}$, $p_7 = e^{-i\delta_1 - i\varphi_\Omega \theta + i2\varphi_V \sin(\theta/2)}$ and $p_8 = e^{-i\delta_2 - i\varphi_\Omega (2\pi - \theta) - i2\varphi_V \sin(\theta/2)}$. We therefore modify the formalism of Chapter 3 by substituting P_5 and P_6 in place of P_1 and P_2. This yields a field through port transmission coefficient $\rho_{oI} = \dfrac{b_{oI}}{a_{oI}} = \dfrac{r_o - \tau_i p_8}{1 - r_o \tau_i p_8}$ and drop-port transmission coefficient $\tau_{oI} = \dfrac{b_{ooI}}{a_{oI}} = \dfrac{-k_o k_{oo}(y_3 + y_4 \rho_i)}{p_4^{-1} - r_o \tau_i}$. The transmission coefficient expressions are then as given in Chapter 3 except that $\rho_i = \dfrac{\rho_1}{1 - \tau_2 p_7}$ and $\tau_i = \dfrac{\tau_1 + (\rho_1 \rho_2 - \tau_1 \tau_2) p_7}{1 - \tau_2 p_7}$ in place of $\rho_i = \dfrac{\rho_1}{1 - \tau_2 e^{-i\delta_1}}$

and $\tau_i = \dfrac{\tau_1 + (\rho_1\rho_2 - \tau_1\tau_2)e^{-i\delta_1}}{1-\tau_2 e^{-i\delta_1}}$ respectively. The transmission coefficients for counter clockwise electric field flow, i.e. $\rho_{oII} = \dfrac{b_{oII}}{a_{oII}}$ and $\tau_{oII} = \dfrac{b_{ooII}}{a_{oII}}$, are given by the same expressions but with Ω replaced by $-\Omega$. Finally, $\tau_o = \dfrac{a_A}{a_o} = \dfrac{1}{2}(\tau_{oI} + \tau_{oII})$ and $\rho_o = \dfrac{a_B}{a_o} = \dfrac{1}{2}(\rho_{oI} + \rho_{oII})$. The design for odd values of $N/2$ yields more complex circuit layouts since the output signal ports must be coupled through cross-over waveguides, hence we restrict our attention to $N = 4,8,12\ldots$

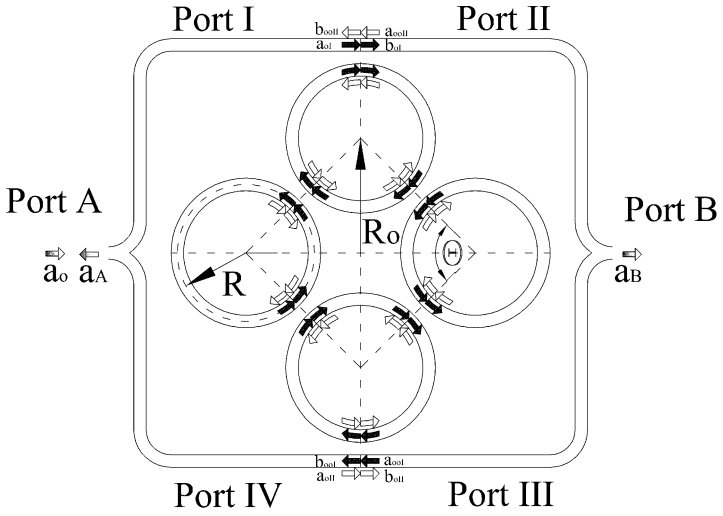

Figure 4.3: CLR gyroscope with $N = 4$

4.3 Summary of previous CROW and FOG results

Before presenting results on our new structures, we first elucidate the features of the CROW and FOG designs of [81] and [7] that are required in the comparison with the additional waveguide structures examined in the next section. First, we note that if the CROW gyroscope calculations leading to Figure (3) in [81], which we believe were carried out for $\lambda_o = 1.55\ \mu m$, $\kappa > 0.01$ and $\alpha = 0$ are graphed in S.I. units, we arrive at the results of Figure 4.4 where Ω is given in rad/s such that $1Hz = 2\pi\, rad/s$. As expected, the magnitude of the CROW gyroscope sensitivity S increases as $(N+1)^2$ while from Figure 4.4.a, the normalized power level at the output port (B) is $\approx 10^{-9}$ for a single ring CROW and $\approx 10^{-7}$ for a 21-ring structure. Note that even with the more physical input values of [7], S varies as $(N+1)^2$, but while equation 3 in [7] indicates that the output power at port B varies as $\sin^2(\Delta\varphi_s) \approx \Delta\varphi_s{}^2 \propto (N+1)^2$ for small and moderate κ, Figure 5 of this reference demonstrates immediately that this does not apply to lossy waveguides.

Thus detecting the output signal is challenging for a lossless structure with many rings. This problem is not evident in [81] since employing arbitrary units for physical quantities such as the output field intensity at port B masks S values in the order of $10^8\,[1/Hz]$. To prove that our units correspond to those employed in the calculations of [81], in Figure 4.4.b, we plot instead the relative sensitivity $S|_{N>1}/S|_{N=1}$ against Ω which coincides with Figure 3.b in [81]. Finally, we note that while S is a function of Ω, Figures 3.c and 3.d of [81] graph S against κ and R respectively without specifying Ω. However, if we identify the corresponding Ω with the magnitude of the maximum rotational angular velocity in Figure 3.a of [81], namely $\Omega = 1000\,Hz = 2000\pi\ rad/s$, and plot S against κ and R, we arrive at Figure 4.4.c and Figure 4.4.d respectively for unit input power which indeed again agrees with [81]. However, an input power of $p_o = 1\,mW$ yields $S \approx 10^{-14}\ Ws/rad = 2\pi \times 10^{-14}\ W/Hz$, which implies that the device is clearly impractical especially if we consider realistic values for $\alpha > 0$ and $\Omega << 1000\,Hz$. We believe this is the effect of employing miniature radius ($R = 25\mu m$) in this calculation as well of the power loss through the unused ports in the circuit as noted in [7].

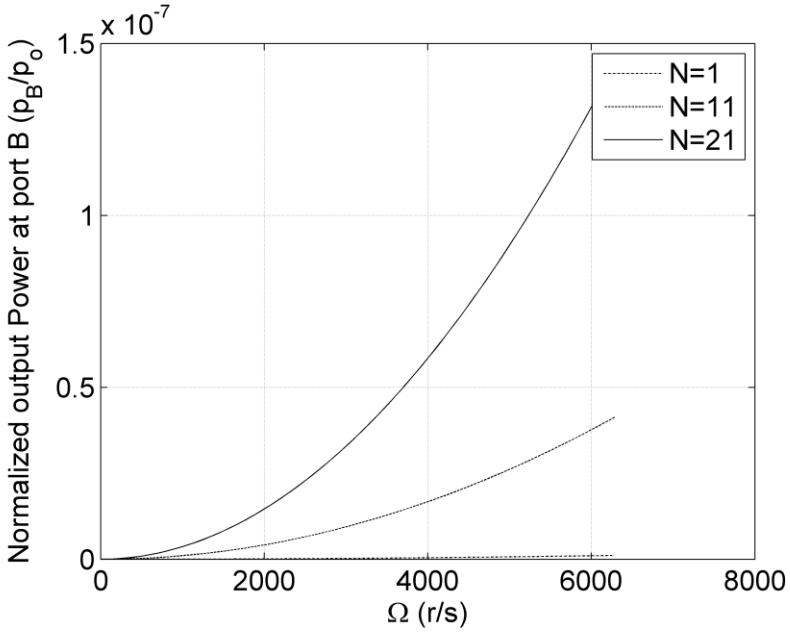

(a)

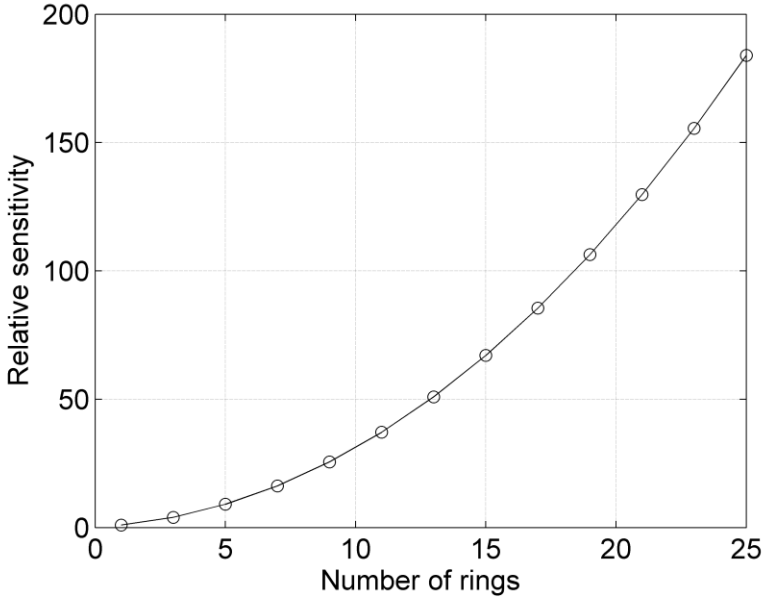
Relative sensitivity
Number of rings
0
50
100
150
200
0
5
10
15
20
25

(b)

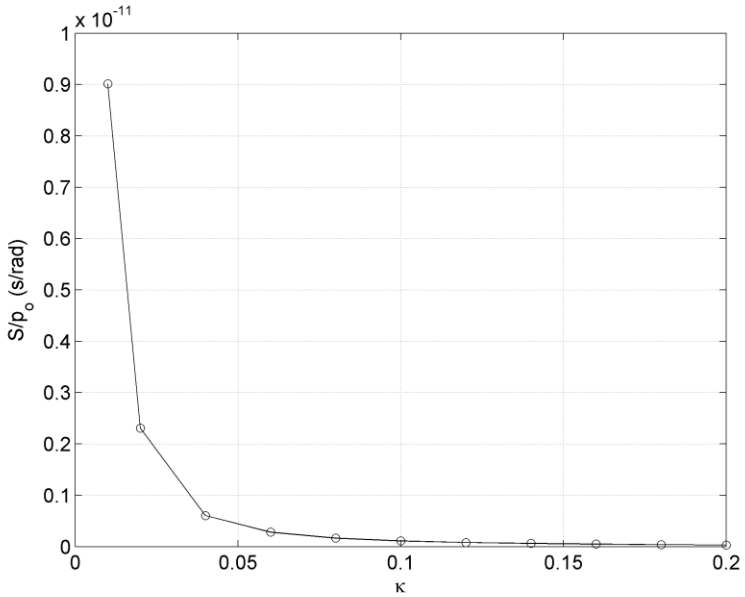
x 10^-11
S/p_o (s/rad)
κ
0
0.1
0.2
0.3
0.4
0.5
0.6
0.7
0.8
0.9
1
0
0.05
0.1
0.15
0.2

(c)

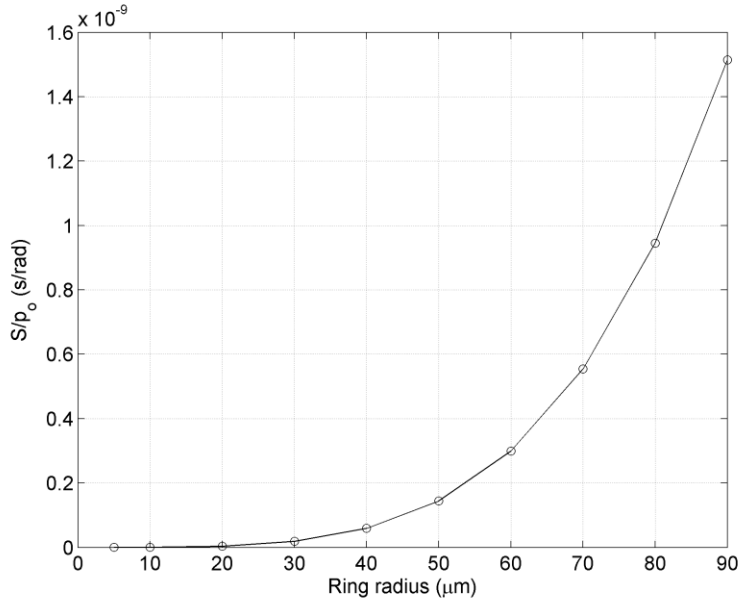

(d)

Figure 4.4: A CROW circuit performance with $\lambda_o = 1.55\,\mu m$ (a) The normalized output power at port B as a function of rotational speed (Ω) for a CROW with $R = 25\,\mu m$, $\alpha = 0$ and $k = k_o = k_{oo} = \sqrt{\kappa} = 0.1$, (b) The relative sensitivity as a function of the rotational speed for the same CROW with $R = 25\,\mu m$, $\alpha = 0$, and $k = k_o = k_{oo} = \sqrt{\kappa} = 0.1$, (c) The CROW sensitivity as a function of the power coupling coefficient (κ) with $N = 9$, $\Omega = 1000Hz = 2000\,\pi\, r/s$, $R = 25\mu m$ and $\alpha = 0$, (d) The CROW sensitivity as a function of the ring radius (R) with $N = 9$, $\alpha = 0$, $\Omega = 1000Hz = 2000\,\pi\, r/s$ and $k = k_o = k_{oo} = \sqrt{\kappa} = 0.1$

In [7] a procedure is given for calculating the CROW gyroscope dimensions that yield the same footprint and loss as a given FOG; namely, $R_f = R\sqrt{N}$, and $e^{-\alpha L_f} = p_A / p_o$, respectively where p_A / p_o is the normalized detected power at port A of a CROW. Since, for the case of Figure (5.c) of [7] $N = 81$, $\kappa = 0.001$ and $R = 5\,cm$, the equivalent FOG has $R_f = 45\,cm$ and $L_f = -\dfrac{\ln(p_A / p_o)}{\alpha} = -\dfrac{\ln(0.6)}{0.2/1000/4.343} = 11093\,m$, yielding $N_f = \dfrac{L_f}{2\pi R_f} \approx 3923$ fiber turns.

The CROW power transmission and sensitivity are shown in Figure 4.5.a and Figure 4.5.b, where the latter is seen to coincide with the Figure 5.c of [7]. Evidently then, the CROW gyroscope, while not as sensitive as a FOG, the far smaller dimensions favor this structure in integrated gyroscope applications.

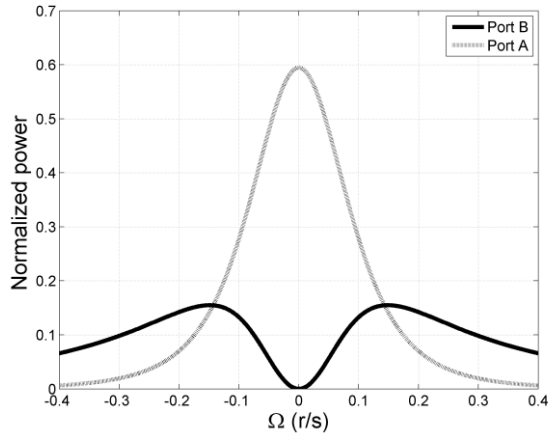

(a)

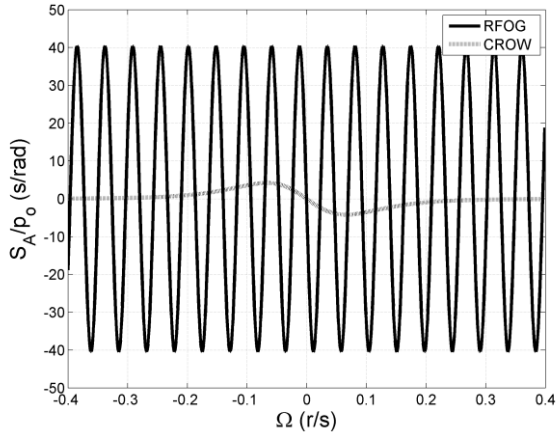

(b)

Figure 4.5: (a) The normalized power transmission of a CROW gyroscope with $N = 81$, $R = 5\,cm$, $\kappa = 0.001$ and $\alpha = 0.2\,dB/km$ at $\lambda_o = 1.55\,\mu m$. (b) The sensitivity of the CROW gyroscope and its equivalent FOG of $R_f = 45\,cm$, $N_f = 3923$ turns, and $L_f = 11093\,m$.

4.4 Numerical results:

In this section we compare the CLR gyroscope to equivalent CROW and FOG structures and then demonstrate that a gyroscope consisting of a single ring in fact generally demonstrates superior performance. To do this, in contrast to [7],[81] where the ring-ring and the ring-bus coupling coefficients are identical we only assume equal coupling between the buses and their neighboring rings, e.g. $k_o = k_{oo}$ but regard the ring-ring field coupling ratio k as an independent value that ranges here from 0.001 to 0.99. In our calculations, we define the sensitivity at ports A and B for

FOG, CROW and CLR gyroscopes by $S_A = \frac{dp_A}{d\Omega}$ and $S_B = \frac{dp_B}{d\Omega}$ respectively and employ unit input power so that $p_o = 1W$. We also graph the value of S at the rotational speed Ω and coupling values for which it is a maximum and finally employ the sensitivity value of the port for which this quantity is again maximized.

We first set $\lambda_o = 1.55\,\mu m$ and $\alpha = 0$, which of course in practice would require active waveguides to compensate for the losses. This yields the dependence of S on N and R for CROW and CLR gyroscopes of Figure 4.6.a and Figure 4.6.b respectively. Here we have found that a CROW gyroscope is more sensitive for $N < 9$, but less sensitive if $N \geq 8$. In this case, the optimal coupling values are equal and << 1 for CROW gyroscopes, for example $k = k_o = k_{oo} = 0.001$, as noted in [81] and [7] since a CROW gyroscope maximizes the Sagnac shift for small coupling coefficients. In contrast, the optimal ring-bus coupling for CLR gyroscopes is typically small ($k_o = k_{oo} << 1$) while ring-ring coupling is large ($k > 0.9$), corresponding to a structure for which the electric field circles repeatedly around the entire device rather than each ring separately.

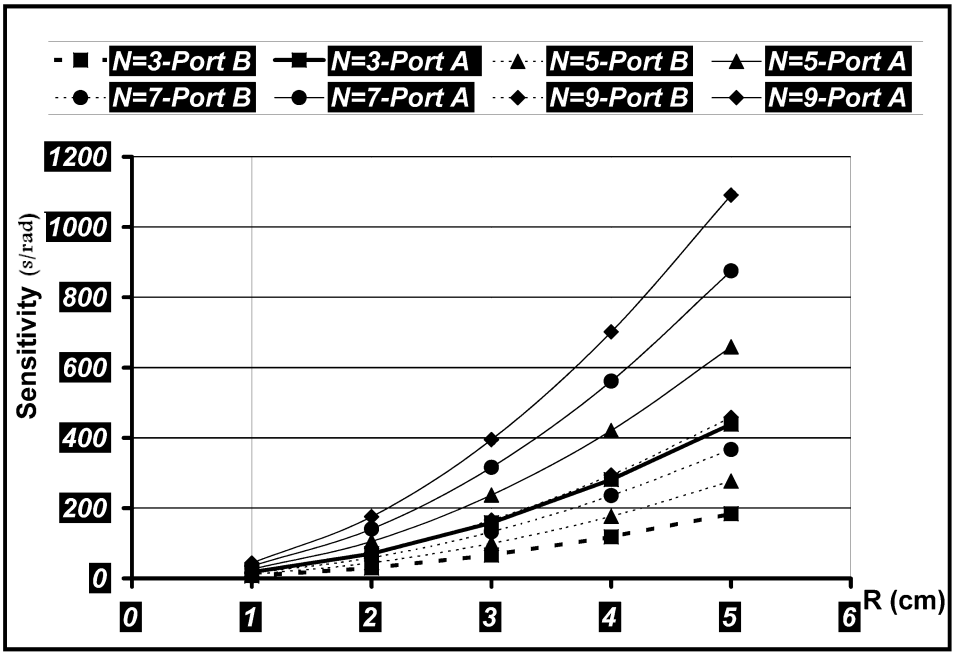

(a)

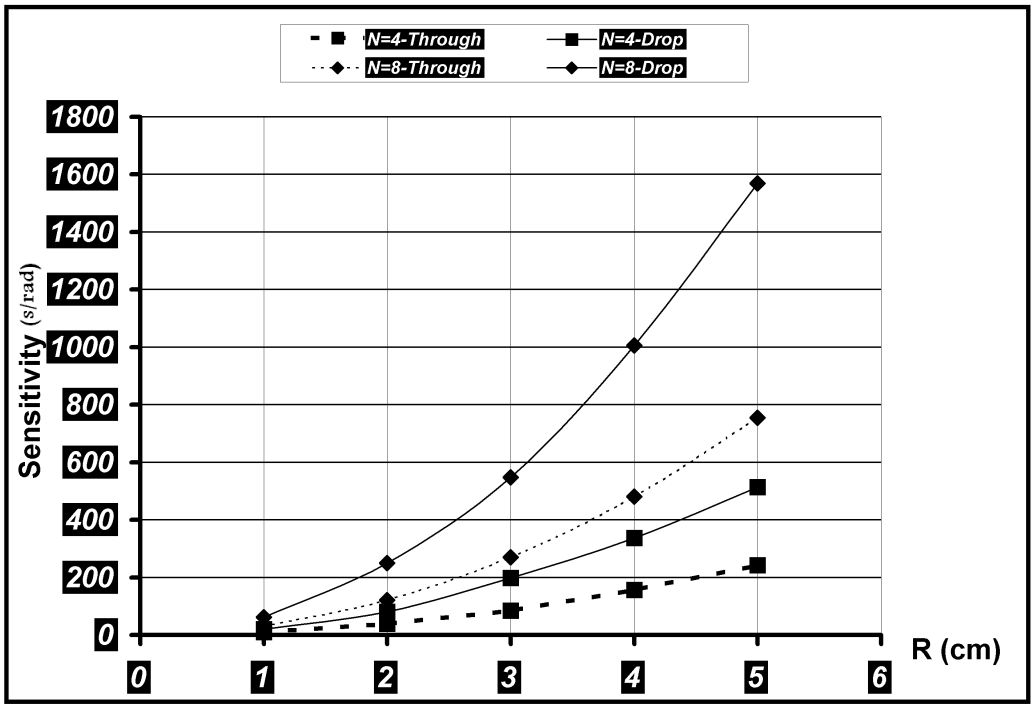

(b)

Figure 4.6: The sensitivity as a function of N and R with $\lambda_o = 1.55 \mu m$ and $\alpha = 0$, (a) a CROW gyroscope, (b) a CLR gyroscope.

If we repeat our calculations for typical fiber parameters, i.e. $\lambda_o = 1.55\ \mu m$ with $\alpha = 0.2\, dB/km$ and $\lambda_o = 0.633\ \mu m$ with $\alpha = 7\, dB/km$ [57], we find the sensitivity curves of Figure 4.7 and Figure 4.8 for the two device structures. Evidently the $S - R$ curves fall into two nearly coinciding families of curves for ports A and B of the CROW gyroscopes, indicating that the sensitivity is nearly independent of N, unlike CLR gyroscopes where S increases with N. However, for any *N* the CLR gyroscope is more sensitive than the CROW. Additionally, to maximize *S* of CROW gyroscopes, $k_o = k_{oo}$ while still << 1, should exceed their values when $\alpha = 0$, and k must be << 1 so that the waveguide couples power to the input and output waveguides lessening the impact of the waveguide losses. In contrast, the optimal values of these quantities are similar for lossy CLR and lossless CLR devices.

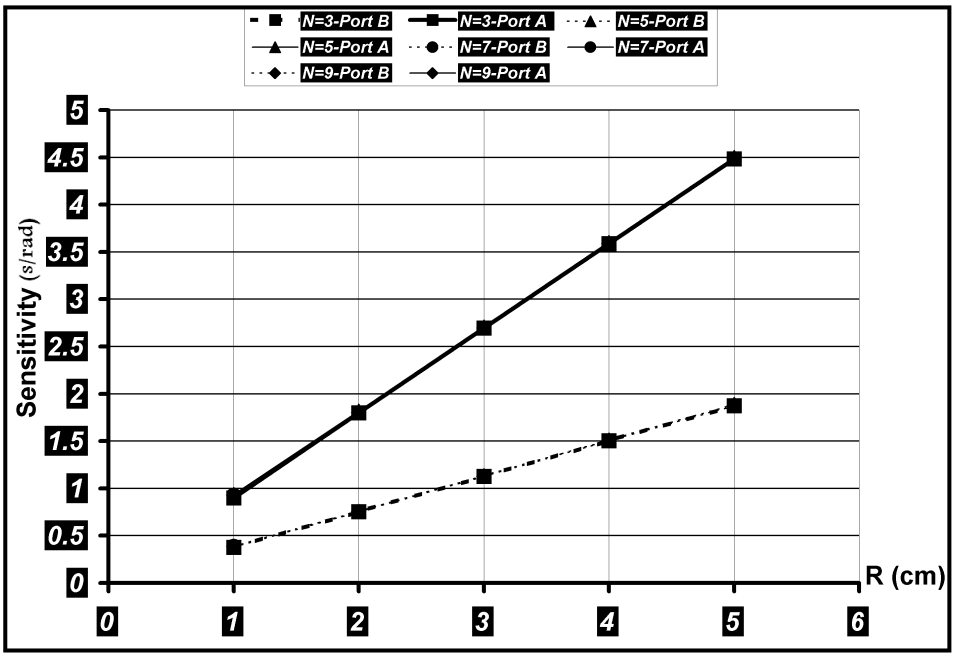

(a)

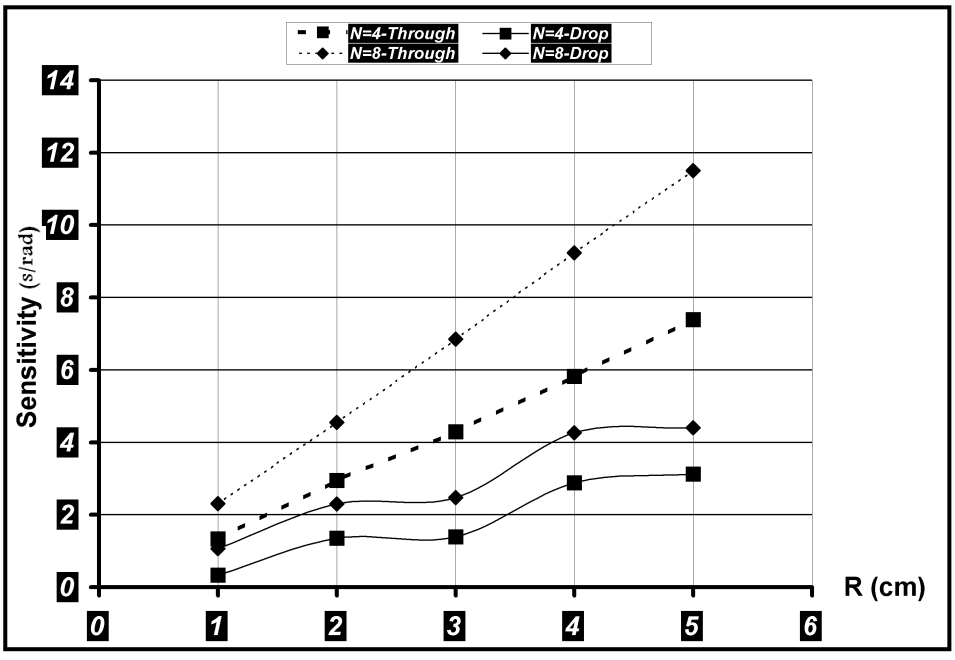

(b)

Figure 4.7: The sensitivity as a function of N and R with $\lambda_o = 1.55\ \mu m$ and $\alpha = 0.2\ dB/km$, (a) a CROW gyroscope, (b) a CLR gyroscope.

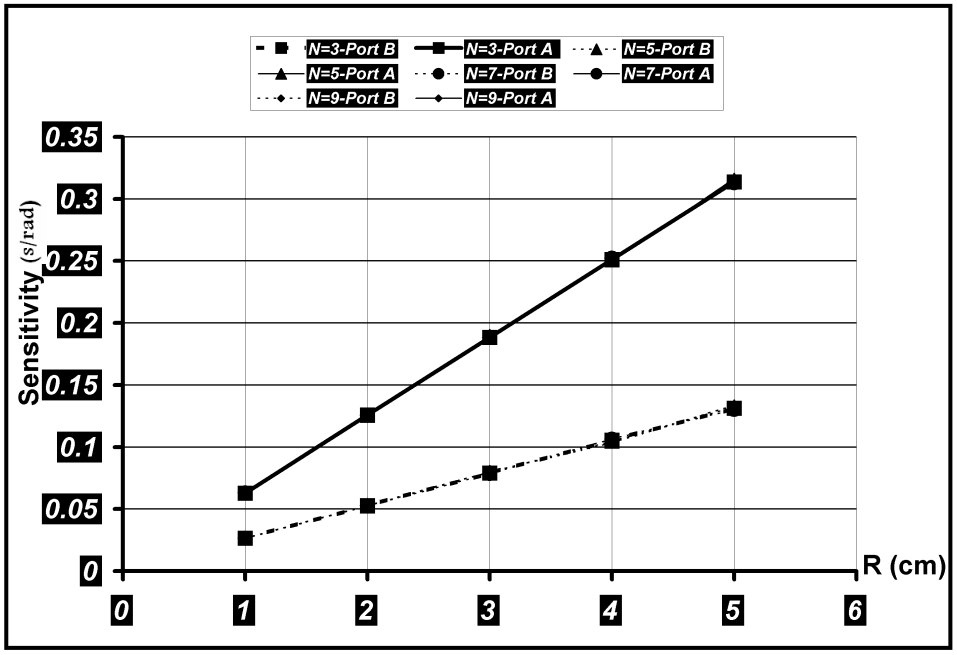

(a)

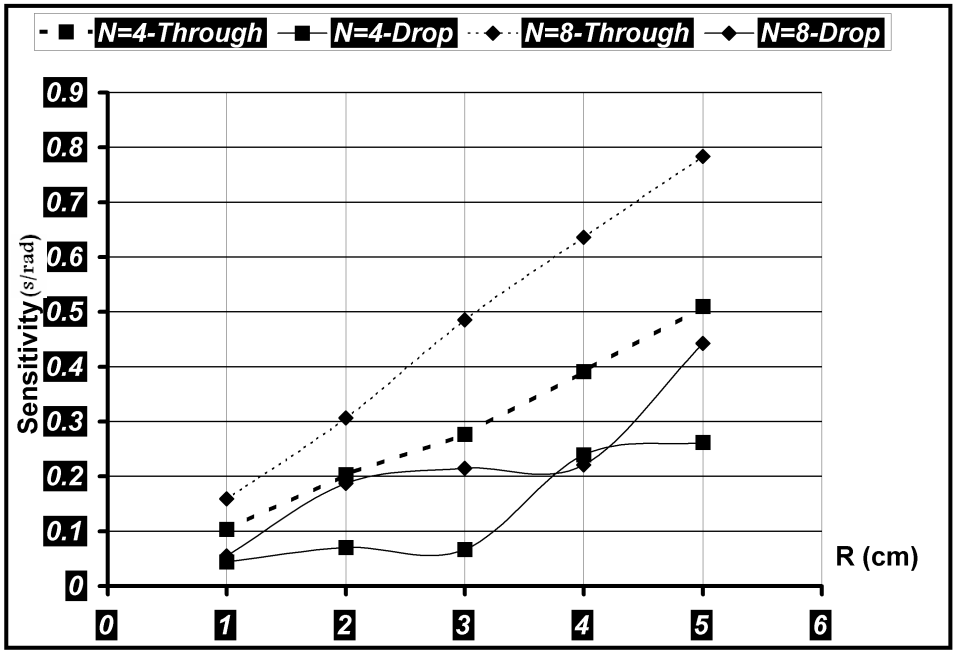

(b)

Figure 4.8: The sensitivity as a function of N and R with $\lambda_o = 0.633\ \mu m$ and $\alpha = 7\ dB/km$, (a) a CROW gyroscope, (b) a CLR gyroscope.

To design an equivalent FOG [7] according to the criterion discussed above for $\lambda_o = 1.55\ \mu m$ and $\alpha = 0.2\ dB/km$, we compute the sensitivity of the FOG as a function of R that is equivalent to a CROW gyroscope of given radius R and number of rings N. Our results are displayed in Figure 4.9.a, where the legends are labeled as FN, in which F stands for "fiber" and N is the number of the counterpart CROW rings. In Figure 4.9.b we examine the FOG structures that are equivalent to a CLR gyroscope. Since $S_A = S_B$ for a FOG only S_A is shown in Figure 4.9. Clearly the sensitivity of a CROW gyroscope is less than that of the equivalent FOG, as noted above while the sensitivity of a CLR gyroscope exceeds that of the equivalent FOG. Since the FOG requires very long fibers, for example $L_f = 41932\ \text{m}$, $N_f = 66737\ \text{turns}$, $Rf = 0.1\text{m}$ for the structure equivalent to a CLR gyroscope of $R = 5cm$ and $N = 5$, we conclude that a CLR gyroscope can potentially replace a FOG.

However, if the ring-ring coupling is close to 100%, while the ring-bus coupling is near zero, the electromagnetic field effectively only propagates through the region of each ring of the CLR between the coupling regions. However, the resulting circuit around the circle ring waveguides is transverse multiple times indicating that single large ring with an area equal to that of the CLR yields an optimal Sagnac shift. Accordingly, we considered the *equivalent* single ring gyroscope, i.e. that with an area approximately equal to that of the CROW and CLR gyroscopes with *N* rings of radius *R* for $\lambda_o = 1.55\ \mu m$ and $\alpha = 0.2\ dB/km$. The corresponding $S - R$ curves are shown in Figure 4.10.a and Figure 4.10.b respectively. Here we denote our results by SNA and SNB for ports A and B respectively. Evidently the single ring gyroscope yields superior performance when the ring-bus coupling coefficients are set equal, $k_o = k_{oo}$, and as small as possible. Thus CROW gyroscope of $N = 9$ and $R = 5\,cm$ displays a maximum sensitivity of 4.483, while the same value for the equivalent FOG is 15.8899 and for the equivalent single ring gyroscope 29.2645. Similarly, a CLR gyroscope with $N = 8$ and $R = 5\,cm$ exhibits a maximum sensitivity of 11.5071 (exceeding that of the CROW with $N = 9$), while the corresponding value for the equivalent FOG is 10.8712 and for equivalent single ring gyroscope 23.4783. Note that our calculation differs from that of [7], in which the ratio of the sensitivity of a CROW gyroscope to its equivalent FOG was reported to have a maximum value near unity for $N = 1$, since in [7], R is held fixed, leading to a larger FOG circuit size for larger *N*, while the circuit area is instead invariant in our calculations.

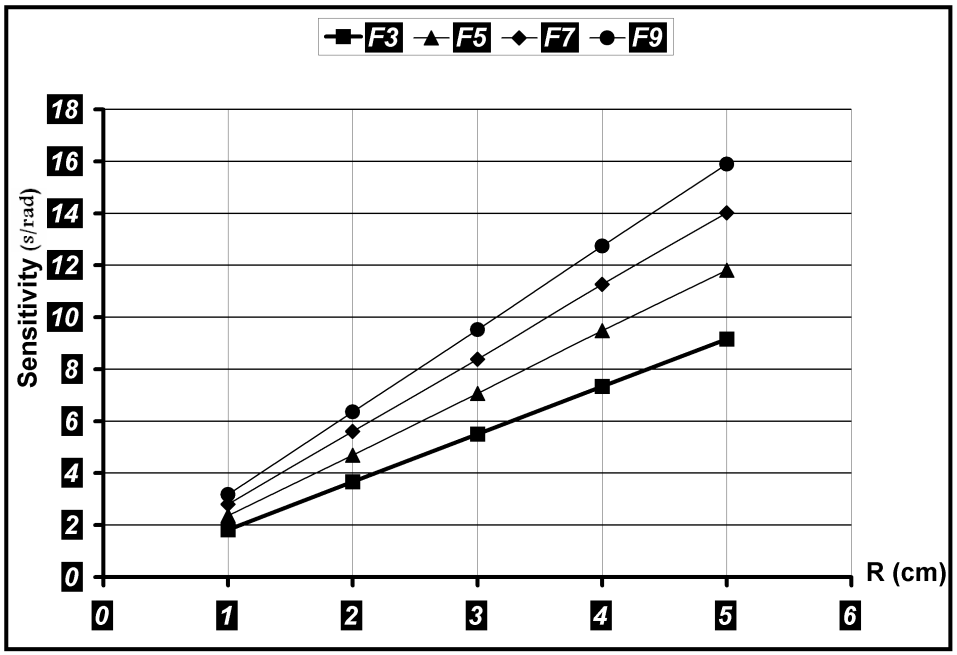

(a)

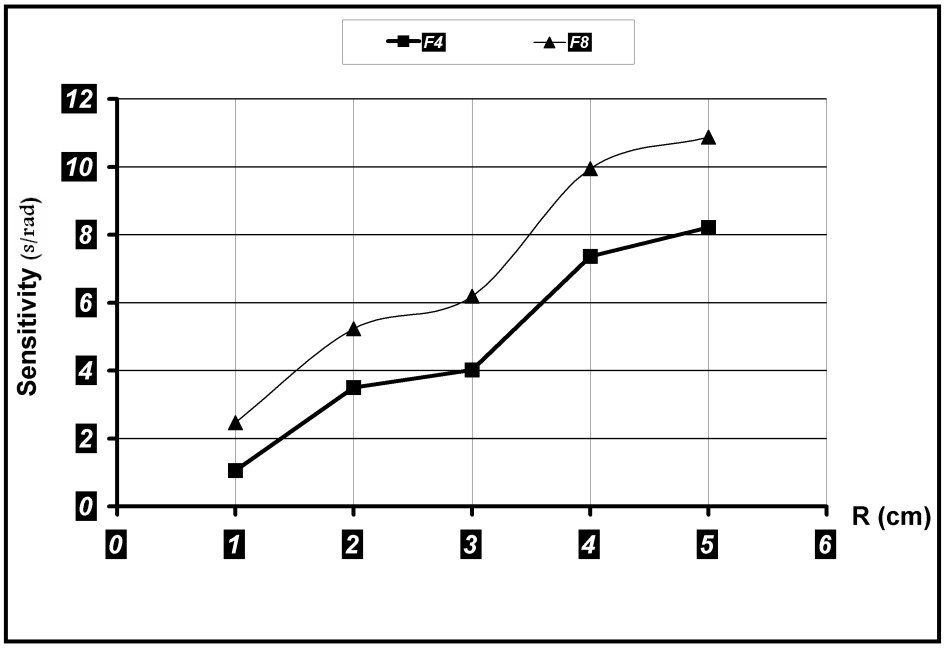

(b)

Figure 4.9: The sensitivity of the *equivalent* FOG for (a) CROW gyroscopes and (b) for CLR gyroscopes, with $\lambda_o = 1.55\ \mu m$ and $\alpha = 0.2\ dB/km$.

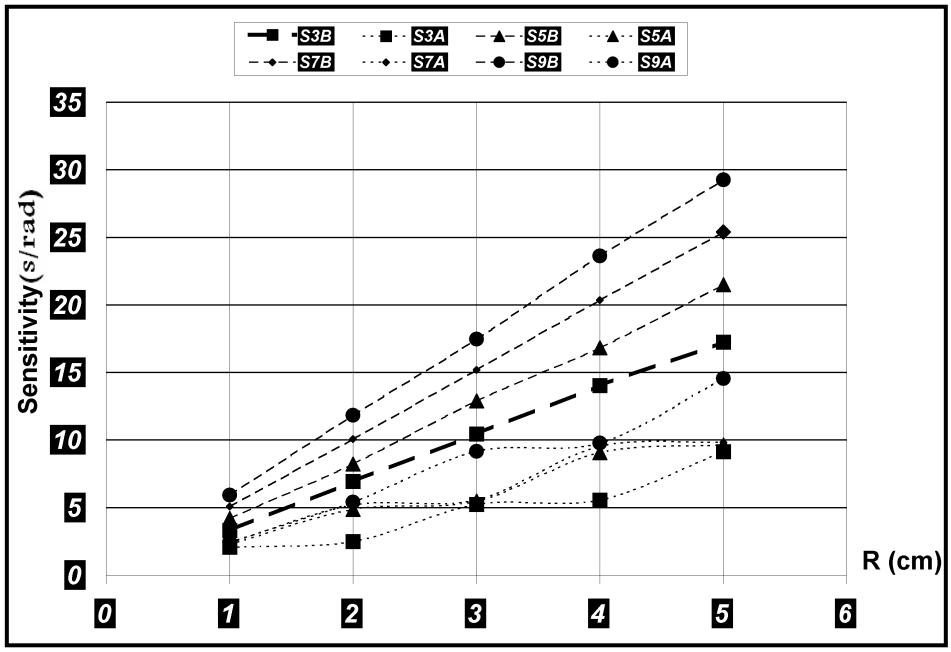

(a)

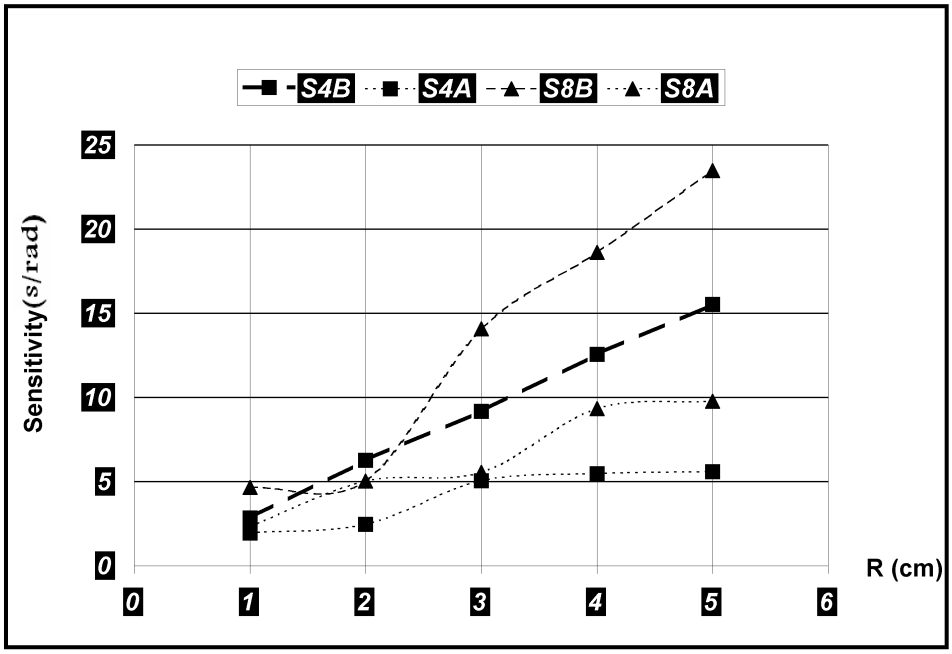

(b)

Figure 4.10: The sensitivity of the *equivalent* single ring gyroscope for (a) CROW gyroscopes and (b) for CLR gyroscopes, with $\lambda_o = 1.55\ \mu m$ and $\alpha = 0.2\ dB/km$.

4.5 Conclusion

In this chapter we studied a CLR gyro composed of a circle of mutually coupled ring resonators. As expected, we have found that a CLR structure is more sensitive to rotation than an equivalent FOG or CROW gyroscope. As well, the maximum sensitivity results when the coupling between the rings ≈ 1 and the coupling to the outer buses is $<<1$leading to the conclusion that the Sagnac shift is most efficiently amplified if the field propagates multiple times through the entire circuit. Consistent with this explanation, our calculations demonstrated that a gyroscope with a single ring that is weakly coupled to the buses is more sensitive for a fixed device dimension supporting the conclusions of [8].

Chapter 5

Conclusion and future work

In this work we have obtained several main results. The first of these is a new design of a tunable ring resonator (RR) circuit based on a hybrid structure incorporating an electro-optic polymer layer above a standard silicon over insulator (SOI) waveguide such that an externally applied electric field between two electrodes changes the refractive index (RI) of the polymer layer and hence the phase of the propagating mode. We discussed two approaches to tuning and showed sample design parameters based on standard waveguide dimensions and losses. The proposed device is expected to provide a switching speed of $20-100\ GHz$, which exceeds that obtained with current SOI technology, while still maintaining compatibility with CMOS components. A single polarity tuning voltage (V) can be employed unlike SOI devices for which dual polarity drive voltages are recommended. The quality factor (Q) is independent of V, unlike plasma tuned SOI devices, and is in the standard range of 10^4 similarly to the counterpart polymer and SOI devices. The extinction ratio (ζ) can as well approach $100\,dB$. We further studied the relation between the ring radius (R), and the depending parameters such as the tuning range (TR) and the free spectral range (FSR), and V. Our results show that this device can be optimized for standard Wavelength Division Multiplexing (WDM) applications with $FSR = 0.8\,nm$ unlike standard structures.

Next, we performed a comparison of numerical procedures in the context of a complex compound RR structure containing a compound ring formed from several individual ring resonators. Our studies, which comprised coupling of modes in space (CMS), the coupling of modes in time (CMT) and the finite difference time domain (FDTD) techniques demonstrated that while the CMT is the simplest to apply, the CMS is applicable to a larger range of coupling and losses. FDTD simulations were in good agreement with the two analytical techniques but required far greater computational resources. With these methods, we were able to customize the ring resonator configuration for WDM interleaver/deinterleaver circuit applications where we demonstrated that unlike the current state-of-the-art circuit which employs seven RRs, a structure employing five RRs could be employed, yielding simpler design rules, higher fabrication yield and smaller circuit area. We then fabricated this circuit using deep ultra-violet photolithography at a wavelength of $193\,nm$ in collaboration with UBC and IMEC. Our experimental results agreed well with theoretical expectations to within the expected fabrication tolerance.

Finally, we analyzed integrated RR based gyroscopes and compared them to a standard fiber optic gyroscope (FOG) with equivalent dimensions. While the FOG was found to exhibit superior performance, integrated gyroscopes could be competitive at presently unattainable lower waveguide losses.

Our results could find future application in numerous contexts. Improved versions of our tunable hybrid structure, especially in conjunction with future advances in polymer technology, could reduce the effect of fabrication error in many devices by providing a compensation mechanism through adjustments to the tuning voltage. As well, extensions of the compound RR structure that we examine in the second part of the thesis could be optimized for advanced processing functions such as digital and analog modulators and filters within a reduced footprint. For example, a similar structure

designed to control both signal amplitude and phase, could be employed to implement quadrature amplitude modulation (QAM) as well as amplitude shift keying (ASK) and phase shift keying (PSK). Finally, our results on integrated optical gyroscopes could eventually be employed together with active waveguides to achieve light weight and small volume devices.

In conclusion RR circuits could provide a high speed, large bandwidth alternatives to many standard devices for essential functions such as signal generation, modulation, amplification and routing. However, while this could provide additional levels of miniaturization and integration, the rather stringent fabrication tolerances constitute an obvious drawback. As a consequence, our experience indicates that optimal RR device parameters can generally only be established through repeated design and fabrication cycles.

References

1. E. A. J. Marcatilli, “Bends in optical dielectric waveguides,” Bell System Technical Journal vol. 48, pp. 2103–2132, 1969.

2. B. E. Little and S. T. Chu, “Theory of Polarization Rotation and Conversion in Vertically Coupled Microresonators,” IEEE Photonics Technology Letters, vol. 12, no. 4, pp. 401-403, 2000

3. B. E. Little, S. T. Chu, H. A. Haus, J. Foresi, and J.-P. Laine, “Microring Resonator Channel Dropping Filters,” Journal of Lightwave Technology, vo. 15, no. 6, pp. 998-1005, 1997

4. Q. Xu, J. Shakya, and M. Lipson, “Direct measurement of tunable optical delays on chip analogue to electromagnetically induced transparency," Optics Express, vol. 14, no. 14, pp. 6463-6468, 2006

5. S. Suzuki, Y. Hatakeyama, Y. Kokubun and S. T. Chu, “Precise Control of Wavelength Channel Spacing of Microring Resonator Add–Drop Filter Array,” Journal of Lightwave Technology, vol. 20, no. 4, pp. 745-750, 2002

6. I. Chremmos and N. Uzunoglu, “Reflective Properties of Double-Ring Resonator System Coupled to a waveguide,” IEEE Photonics Technology Letters, vol. 17, no. 10 , pp. 2110-2112, 2005

7. M. A. Terrel, M. J. F. Digonnet, and S. Fan, “Performance Limitation of a Coupled Resonant Optical Waveguide Gyroscope,” Journal of Lightwave Technology, vol. 27, no. 1, pp. 47-54, January 2009

8. M. Terrel, M. J. F. Digonnet, and S. Fan, “Performance comparison of slow-light coupled-resonator optical gyroscopes,” Laser Photonics Review, vol. 3, no. 5, pp. 452–465, 2009

9. Q. Xu and M. Lipson, “All-optical logic based on silicon micro-ring resonators,” Optics Express vol. 15, no. 3, pp. 924–929, 2007

10. M. Lipson, “Guiding, Modulating, and Emitting Light on Silicon—Challenges and Opportunities," Journal of Lightwave Technology, vol. 23, no. 12, pp. 4222-4238, 2005

11. Payam Rabiei and William H. Steier, “Tunable Polymer Double Micro-Ring Filters,” IEEE Photonics Technology Letters, vol. 15, no. 9, pp. 1255-1257, 2003

12. P. abiei, William H. Steier, Cheng Zhang, and Larry R. Dalton, “Polymer Micro-Ring Filters and Modulators,” Journal of Lightwave Technology, vol. 20, no. 11, pp.1968-1975, 2002

13. Mojca Jazbinšek, Payam Rabiei, Christian Bosshard and Peter Günter, “Nonlinear Organic Materials For VLSI Photonics,” AIP Conference Proceedings, vol. 709, pp. 187-213, 2004

14. V. Van, P.P: Absil, J.V. Hryniewicz, P.-T. Ho, “Propagation loss in single-mode GaAs-AlGaAs microring resonators: measurement aid model,” IEEE Journal of Lightwave Technology, vol.19, no. 11, pp. 1734-1739, 2001

15. D.G. Rabus, M. Hamacher, “MMI-coupled ring resonators in GaInAsP-InP,” IEEE Photonics Technology Letters, vol. 13, no. 8, pp. 812-814, 2001

16. K. Okamoto, *Fundamentals of Optical Waveguides*, Academic Press, U.S.A, 2000.

17. W. V. McLevige, T. Itoh And Rajmittra, “New Waveguide Structures for Millimeter-Wave and Optical Integrated Circuits, “ IEEE Transactions on microwave theory and techniques, vol. M-23, no. 10, pp. 788-794, 1975

18. G. B. Hocker and W. K. Burns, “Mode dispersion in diffused channel waveguides by the effective index method,” Applied Optics, vol. 16, no. 1, pp. 113-118, 1977

19. Isa Kiyat, Atilla Aydinl and Nadir Dagli, “High-Q silicon-on-insulator optical rib waveguide racetrack resonators,” Optics Express, vol.13, no. 6, pp. 1900-1905, 2005

20. Vijaya Subramaniam, Gregory N. De Brabander, David H. Naghski, and Joseph T. Boyd, “Measurement of Mode Field Profiles and Bending and Transition Losses in Curved Optical Channel Waveguides,” Journal of Lightwave Technology, vol. 15, no. 6, pp. 990-997, 1997

21. K. R. Hiremath, M. Hammer, S. Stoffer, L. Prkna, and J. Ctyroký, “Analytic approach to dielectric optical bent slab waveguides,” Opical and Quantum Electronics., vol. 37, no. 1–3, pp. 37–61, Jan. 2005.

22. B. Hermansson, D. Yevickt and J. Saijonmaat, “Propagating-beam-method analysis of two-dimensional microlenses and three-dimensional taper structures,” Journal of Optical Society of Amrica A, vol. 1, no. pp. 663-671, 1984

23. J. Saijonmaa and D. Yevick, “Beam-propagation analysis of loss in bent optical waveguides and fibers,” Journal of Optical Society of America, vol.73, no. 12, pp. 1785-1791, 1983

24. D. Yevick and B. Hermansson, “Efficient Beam Propagation Techniques,” IEEE Journal of Quantum Electronics, vol. 26, no. 1, pp. 109-112, 1990

25. D. Yevick and M. Glasner, “Analysis of forward wide-angle light propagation in semiconductor rib waveguides and integrated-optic structures,” Electronics Letters, vol. 25, no. 23, pp. 1611–1613, 1989.

26. Y. Chung and N. Dagli, “An assessment of finite difference beam propagation method,” Journal of Quantum Electronics, vol. 26, no. 8, pp. 1335-1339, 1990.

27. R. Scarmozzino and R.M. Osgood, Jr., “Comparison of finite-difference and Fourier-transform solutions of the parabolic wave equation with emphasis on integrated-optics applications,” Journal of Optical Society of America A, vol. 8, no. 5, pp. 724-731, 1991.

28. D. Yevick, C. Rolland and B. Hermansson, “Fresnel equation studies of longitudinally varying semi conductor rib waveguides : reference wavevector dependence,” Electronics Letters, vol. 25, no. 18, pp. 1254-1256, 1989

29. F. Grillot, L. Vivien, S. Laval, and E. Cassan, “Propagation Loss in Single-Mode Ultrasmall Square Silicon-on-Insulator Optical Waveguides," Journal of Lightwave Technology, vol. 24, no. 2, pp. 891-896, 2006

30. T. Tsuchizawa, T. Watanabe, E. Tamechika, T. Shoji, K. Yamada, J. Takahashi, S. Uchiyama, S. Itabashi, and H. Morita, “Fabrication and evaluation of submicron-square Si wire waveguides with spot-size converters,” in Proceedings of Lasers and Electro-Optics Society (LEOS) Annual Meeting, Glasgow, U.K., pp. 287, 2002

31. W. Bogaerts, R. Baets, P. Dumon, V. Wiaux, S. Beckx, D. Taillaert, B. Luyssaert, J. V. Campenhout, P. Bienstman and D. V. Thourhout “Nanophotonic Waveguides in Silicon-on-Insulator

Fabricated With CMOS Technology," Journal of Lightwave Technology, vol. 23, no 1, pp. 401-412, 2005

32. P. Dumon, "Ultra-Compact Integrated Optical Filters in Silicon-on-insulator by Means of Wafer-Scale Technology," Ph.D. dissertation, Department of Electrical Engineering, Ghent University, Belgium, 2007

33. M. Heiblum and J. H. Harris, "Analysis of Curved Optical Waveguides by Conformal Transformation," IEEE Journal of Quantum Electronics, vol. QE-11, no. 2, pp. 75-83, 1975

34. W. Berglund and A. Gopinath, "WKB Analysis of Bend Losses in Optical Waveguides," Journal of Lightwave Technology, vol. 18, no. 8, pp. 1161-1166, 2000

35. R. Clauberg and P. Von Allmen, "Vectorial beam propagation method for integrated optics", Electronics Letters, vol. 27, no. 8, pp. 654-655, 1991

36. W.P. Huang and C.L. Xu, "Simulation of three-dimensional optical waveguides by a full-vector beam propagation method," Journal of Quantum Electronics, vol. 29, no. 10, pp. 2639-2649, 1993

37. H.J.W.M. Hoekstra, G.J.M. Krijnen, and P.V. Lambeck, "New formulations of the beam propagation method based on the slowly varying envelope approximation," Optics Communications, vol. 97, pp. 301-303, 1993.

38. Y. Liu, T. Chang and A. E. Craig, "Coupled mode theory for modeling microring Resonators," Optical Engineering, vol. 44, no.8, 2005

39. H. A. Haus, W. P. Haung, S. Kawakami, and N. A. Whitaker, "Coupled mode theory of optical waveguides," Journal of Lightwave Technology, vol. LT-5, no. 1, pp. 16–23, 1987

40. C. Ma, X. Yan, Y. Xu, Z. Qin and X. Wang, "Characteristic analysis of bending coupling between two optical waveguides," Optical and Quantum Electronics, vol. 37, no. 11, pp. 1055–1067, 2005

41. Y. A. Vlasov and S. J. McNab, "Losses in single-mode silicon-on insulator strip waveguides and bends," Optics Express, vol. 12, no. 8, pp. 1622–1631, 2004

42. K. K. Lee, D. R. Lim, H.-C. Luan, A. Agarwal, J. Foresi, and L. C.Kimerling, "Effect of size and roughness on light transmission in a Si/SiO2 waveguide: Experiments and model," Applied Physics Letters, vol. 77, no. 11, pp. 1617–1619, Sep. 2000

43. C. J. Kaalund and G. D. Peng, "Pole-Zero Diagram Approach to the Design of Ring Resonator-Based Filters for Photonic Applications," Journal of Lightwave Technology, vol. 22, no. 6, pp. 1548-1559, 2004

44. V. Padgaonkar, M. Lipson, and S. Pradhan, "Thermal Effects in Silicon Based Resonant Cavity Devices," 2004 NNIN REU Research Accomplishments, pp. 98-99 , 2004

45. Q. Xu, B. Schmidt, S. Pradhan and M. Lipson, "Micrometre-scale silicon electro-optic modulator," Nature Letters, vol. 435, no. 19, pp. 325-327, 2005

46. Q. Xu and M. Lipson, "Carrier-induced optical bistability in silicon ring resonators," Optics Letters vol. 31, no. 3, pp. 341-343, 2006

47. S. Manipatruni, C. B. Poitras, Q. Xu, and M. Lipson, "High Speed Electro-Optic Tuning of the Optical Quality Factor of a Silicon Micro-cavity," Optics Letters, vol. 33, no. 15, pp. 1644-1646, 2008

48. K. K. McLauchlan, and S. T. Dunham, “Analysis of a Compact Modulator Incorporating a Hybrid Silicon/Electro-Optic Polymer Waveguide,” IEEE Journal of Selected Topics in Quantum Electronics, vol. 12, no. 6, pp. 1455-1460, 2006

49. C. Ozturk, A. Huntington, A. Aydinli, Y. Tae Byun, and N. Dagli, ”Filtering Characteristics of Hybrid Integrated Polymer and Compound Semiconductor Waveguides,” Journal of Lightwave Technology, vol. 20, no. 8, pp.1530-1536, 2002

50. P. B. Johnson and R. W. Christy, "Optical constants of the nobel metals," Physics Review B, vol. 6, issue 12, pp. 4370-4379, 1972

51. M. D. Watson, P. R. Ashley, A. J. Guenthner, and M. A. G. Abushagur, “Modeling of Electrooptic Polymer Electrical Characteristics in a Three-Layer Optical Waveguide Modulator," IEEE Journal of Quantum Electronics, vol. 41, no. 4, pp.589-595, 2005

52. M. N. Afsar and K. J. Button, “Dielectric Properties of Millimeter Wave Materials,” 1EEE Microwave Symposium DIGEST MTT-S International DIGEST, vol. 84, pp. 522-524, 1984

53. D. Chen, H. R. Fetterman, A. Chen, W. H. Steier, and L. R., Wenshen Wang and Yongqiang Shi, “Demonstration of 110 GHz electro-optic polymer modulators,” Applied Physics Letters, vol. 70, no. 25, pp. 3335-3337, 1997

54. D. G. Girton S. L. Kwiatkowski, G. F. Lipscomb, and R. S. Lytel, “20 GHz electro-optic polymer Mach-Zehnder modulator,” Applied Physicd Letters, vol. 58, no. 16, pp.1730-1772, 1991

55. M. Wik, D. Dumas, and D. Yevick, “Comparison of vector finite-difference techniques for modal analysis,” Journal of the Optical Society of America A - Optics Image Science and Vision, vol. 22, no. 7, pp. 1341-1347, 2005

56. J. Wang, J. E. Bowers, and A. Fang, “Loss, Reflection and Transmission Measurement and Analysis of Silicon-on-Insulator Ring Resonators," Electrical Engineering and Bioengineering, University of Pennsylvania, OPTICS • NNIN REU 2006 Research Accomplishments, pp. 112-113, 2006

57. G. Keiser, *Optical Fiber Communications*, McGraw Hill International Editions, 3rd edition, 2000.

58. A. Yariv, “Critical Coupling and Its Control in Optical Waveguide-Ring Resonator Systems,” IEEE Photonics Technology Letters, vol. 14, no. 4, pp. 483-485, 2002.

59. C. Madsen, G. Lenz, A. Bruce, M. Capuzzo, L. Gomez, T. Nielsen, L. Adams, and I. Brener, “An all-pass filter dispersion compensator using planar waveguide ring resonators,” presented at the Optical Fiber Communication Conf, and the International Conf, on Integrated Optics and Optical Fiber Communication, San Diego, CA, Feb. 23–26, 1999, paper FE6.

60. L. Dalton, B. Robinsona, A. Jena, P. Rieda, B.e Eichingera, P. S., A. Akelaitisa, D. Balea, M. Hallerb, J. Luob, S. Liub, Y. Liaoa, K. Firestonea, N. Bhatambrekara, S. Bhattacharjeea, J. Sinnessa, S. Hammonda, N. Bukera, R. Snoebergera, M. Lingwooda, H. Rommela, J. Amenda, S. Jangb, A. Chenc and W. Steierd , “Electro-optic coefficients of 500 pm/V and beyond for organic materials,” Proceedings of SPIE, vol. 5935, 2005 (SPIE, Bellingham, WA, 2005)

61. G. Cocorullo, F. G. Della Corte, R. De Rosa, I. Rendina, A. Rubino, and E. Terzini, “Amorphous Silicon-Based Guided-Wave Passive and Active Devices for Silicon Integrated Optoelectronics,” Selected topics in Quantum Electronics, vol. 4, no. 6, pp. 997-1002,1998

62. D. K. Sparacin, R. Sun, A.M. Agarwal, M.A. Beals, J. Michel, L.C. Kimerling, T. J. Conway, A.T. Pomerene, D.N. Carothers, M.J. Grove, D.M. Gill, M.S. Rasras, S.S. Patel and A.E. White,

"Low-Loss Amorphous Silicon Channel Waveguides for Integrated Photonics," Group IV Photonics, 3rd IEEE International Conference, Ontario, Canada, pp.255-257, 2006

63. P. Koonath and B. Jalali, "Multilayer 3-D photonics in silicon," Optics Express, vol. 15, no.20, pp. 12686-12691, 2007

64. C. Mazuré and A. Auberton-Hervé, "Engineering Wafers for the Nanotechnology Era," Proceedings of ESSCIRC, Grenoble, France, pp.29 - 38 , 2005

65. Y. Shi, C. Z., H.Zhang, J. H. Bechtel, L. R. Dalton, B. H. Robinson and W. H. Steier, "Low (Sub 1-Volt) Halfwave Voltage Polymeric Electro-optic Modulators Achieved by Controlling Chromophore Shape," Science, vol. 288, pp. 119–122, 2000.

66. L. Dalton, B. Robinsona, A. Jena, P. Ried, B. Eichinger, S. Jang, J. Luo, S. Liu, Y. Liao, K. Firestone, N. Bhatambrekar, D. Bale, M. Haller, S. Bhattacharjee, J. Schendel, P. Sullivan, S. Hammond, N. Buker, F. Cady, A. Chenc, and W. Steier, "Organic Electro-Optic Materials," Proceedings of SPIE, vol. 5621, pp. 93-100, 2004

67. A. Densmore, D.-X. Xu, P. Waldron, S. Janz, P. Cheben, J. Lapointe, A. Delâge, B. Lamontagne, J. H. Schmid and E. Post, "A Silicon-on-Insulator Photonic Wire Based Evanescent Field Sensor," IEEE Photonics Technology Letters, vol. 18, no. 23, pp. 2520-2522, 2006

68. S. Darmawan, Y. M. Landobasa, and M.-K. Chin, "Pole–Zero Dynamics of High-Order Ring Resonator Filters," Journal of Lightwave Technology, vol. 25, no. 6, pp.1568-1575, 2007

69. C. J. Kaalund, Z. Jin, W. Li, and G. D. Peng, "Novel optical wavelength interleaver based on symmetrically parallel-coupled and apodized ring resonator arrays," presented at the SPIE's 48th annual Meeting: Int. Symp. Optical Science and Technology, San Diego, CA, Aug. 2003.

70. A. V. Oppenheim and R. W. Schafer, *Discrete-Time Signal Processing*, Prentice-Hall, 1989

71. C. K. Madsen and J. H. Zhao, *Optical Filter Design and Analysis: A Signal Processing Approach*, Wiley, New York, 1999

72. H. A. Haus, *Waves and Fields in Optoelectronics*, Prentice Hall, 1984

73. http://www.rsoftdesign.com

74. Design Workshop Technologies, http://www.designw.com/PDA-Overview.php

75. R. Boeck, N. A. F. Jaeger, N. Rouger and L. Chrostowski, "Series-coupled silicon racetrack resonators and the Vernier effect: theory and measurement," Optics Express, vol. 18, issue 24, pp. 25151-25157, 2010

76. D. G. Rabus, "Realization of optical filters based on ring resonators with integrated semiconductor optical amplifiers in GaInAsP /InP," Ph.D. thesis, Heinrich-Hertz Institute for Telecommunications, Berlin 2002

77. S. Vargas and C. Vazquez, "Synthesis of optical filters using microring resonators with ultra-large FSR," Optics Express vol. 18, No. 25, pp. 25936-25949, 2010

78. A. Canciamilla, M. Torregiani, C. Ferrari, F. Morichetti, R. M. De La Rue, A. Samarelli, M. Sorel and A. Melloni, "Silicon coupled-ring resonator structures for slow light applications: potential, impairments and ultimate limits," Journal of Optics, doi: 12/ 10/4008, 2010

79. C. Ferrari, F. Morichetti, and A. Melloni, "Disorder in coupled-resonator optical waveguides," Journal of Optical Society of America B, vol. 26, No. 4, pp. 858-866, 2009

80. E. J. Post, “Sagnac Effect,” Reviews on Modern Physics, vol. 39, no. 19, pp. 475-493, 1967

81. J. Scheuer, and A. Yariv, ”Sagnac Effect in Coupled-Resonator Slow-Light Waveguide Structures,” Physics Review Letters, vol. 96, pp. 053901, 2006